UNIVERSITY OF LIVERPOOL

Surface Structure and Epitaxy on Ag-In-Rare Earth Quasicrystals and Related Approximants

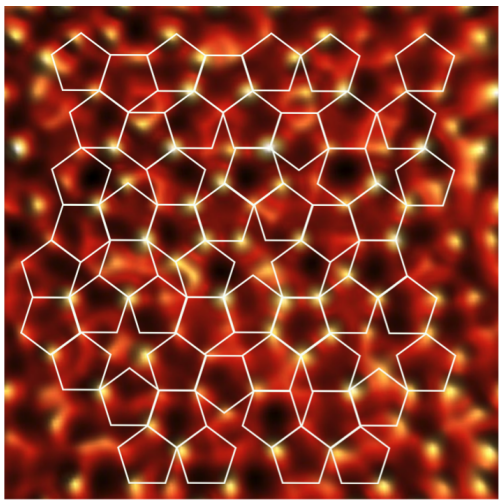

Thesis submitted in accordance with the requirements of the University of Liverpool for the degree of Doctor of Philosophy

By

SANGER SALEEM HARS

JULY 2015

Abstract

This thesis reports on work carried out in the Surface Science Research Centre of the University of Liverpool and in the Jean Lamour Institute, Université de Lorraine, Nancy, France. The research described in this thesis is the experimental investigation of epitaxy on quasicrystal surfaces and the determination of the surface structure of related approximants. Quasicrystals, which are new phases of solids conceptualised in 1982, show aperiodic long range order with lack of translational symmetry. Moreover, quasicrystals possess forbidden rotational symmetries such as five-fold and ten-fold. Quasicrystal surfaces have extensively been studied, however their studies were previously limited to Al-based quasicrystals. In this thesis surface studies are extended to the new ternary Ag-In-Yb quasicrystal and related approximants. Approximants are periodic metallic compounds whose chemical composition and atomic structure are close to their related quasicrystals, but which possess large unit cells.

The specific goals of this thesis are: to understand the surface structure of Ag-In-rare earth (rare earth (RE) = Tb, Gd and Yb) approximants whose structure is similar to their parent quasicrystals; secondly, to achieve artificial single element quasicrystals through the epitaxy on the five-fold surface of icosahedral Ag-In-Yb quasicrystal. Two main surface techniques have been used throughout the work of this thesis, Scanning Tunneling Microscopy (STM) and Low Energy Electron Diffraction (LEED).

The study of the surface structure of Ag-In-RE 1/1 approximants is presented. The bulk structure of these approximants is formed by the same rhombic triacontahedral (RTH) cluster as their parent icosahedral Ag-In-Yb quasicrystal. The RTH cluster consists of five successive atomic shells. The innermost shell is a tetrahedron of four Cd atoms. The second shell is a decagon of twenty Cd atoms. Twelve Yb atoms make an icosahedra in the third shell. The fourth shell is an icosadodecahedron of thirty Cd atoms. Finally, the outer-most shell is the rhombic triacontahedron (RTH) of ninety two Cd atoms. The RTH clusters are packed periodically in approximants. The aim of this work is to understand the surface of approximants and find out how they relate to the surface of the parent quasicrystal. It is found that the surface of Ag-In-Tb and Ag-In-Gd develops facets along different crystallographic directions. The comparison of observed step heights and high resolution STM images of facets with the bulk structure model showed that the surface of approximants similar to the surface of

parent quasicrystal, are bulk terminated. That means the surface corresponds to bulk truncation.

The five-fold surface of the icosahedral Ag-In-Yb quasicrystal was used as a template and two different elements, Bi and In were deposited on the surface. In this work single element quasicrystalline structure was successfully achieved through the deposition of both Bi and In on the surface. Both elements formed quasicrystalline layers on the surface. By comparing the STM images of quasicrystalline layers with the atomic structure of the RTH clusters above the surface, it was found that the adsorbate atoms occupy atomic sites of the RTH clusters. The Bi and In adsorbates were found to occupy different atomic sites. In addition to the symmetry, the structure and chemistry of the substrate seem to play a role in achieving a quasicrystalline thin film.

Contents

Glossary of Terms and Acronyms

Quasicrystals are mostly inter-metallic compounds which show long-range order with lack of periodicity and often possess classically forbidden rotational symmetries such as five-fold and ten-fold.

Approximants are periodic metallic compounds whose chemical composition and atomic structure are close to their related quasicrystals, and they generally possess a large unit cell.

RTH : The rhombic triacontahedral cluster is the basic building block of Ag-In-RE quasicrystals and approximants. It consists of five successive atomic shells. The inner-most shell is a tetrahedron of four Cd atoms. The second shell is a decagon of twenty Cd atoms. Twelve Yb atoms make an icosahedra in the third shell. The fourth shell is an icosadodecahedron of thirty Cd atoms. Finally the outer-most shell is a rhombic triacontahedron (RTH) of ninety two Cd atoms.

Golden ratio (τ) is an irrational number characteristic of quasicrystalline order (τ = 1.618...,).

DOS : Density of States

RE : Rare Earth Elements

UHV : Ultra High Vacuum

RGA : Residual Gas Analyser

STM : Scanning Tunneling Microscopy

TEM : Transition Electron Microscopy

LEED : Low Energy Electron Diffraction

RHEED : Reflection High-Energy Electron Diffraction

SAED : Selected Area Electron Diffraction

XPS : X-ray Photoelectron Spectroscopy

UPS : Ultraviolet Photoelectron Spectroscopy

AES : Auger Electron Spectroscopy

MEIS : Medium Energy Ion Scattering

HAS : Helium Atom Scattering

DFT : Density Functional Theory

DTA : Differential Thermal Analysis

FFT : Fast Fourier Transform

i : Icosahedral

d : Dodecahedral

AR : Acute Rhombohedron

OR : Obtuse Rhombohedron

Acknowledgements

I would like to express my sincere gratitude to the Kurdistan Regional Government (KRG) for providing financial support and the opportunity to do my PhD abroad. I am deeply grateful to both my supervisors Prof. Ronan McGrath and Dr. Hem Raj Sharma for suggesting experimental work and their continued support and guidance during my study and also for providing the opportunity to travel to many places to participate in workshops and conferences.

I would also like to thank Dr. Sam Haq and Dr. Joseph Smerdon whose expertise with UHV systems helped me during experiments. My special thanks go to Dr. Dave Joss from the physics department for his support and encouragement. My thanks also go to people who I met during my study including Dr. Thakur Prasad Yadav, Dr. Vincent Fournée, and Dr. Julian Ledieu for their collaboration and scientific discussions and I am also thankful to Dr. Ryuji Tamura and Dr. Masahiko Shimoda for providing samples and structure models. I am thankful to my coworkers Mike Lowe and Dr. Abdullah Al-Mahboob for collaboration and sharing software ideas.

Finally I would like to thank my family, I am very thankful to my parents, brothers and sisters for their inspiration and encouragement. I would also like to thank my lovely wife Khandah for her love, patience and her constant support and my lovely sons Sinar and Sanyar. My special thanks go to my nearest and dearest uncle Hassan Sulaiman. I thank him for all the help he has given and generosity he has shown.

Sanger Saleem Hars, 2015

Chapter 1

Introduction

1.1 Introduction

Surface phenomena such as friction, adhesion and surface tension are vitally important in processes such as heterogeneous catalysis, corrosion and wear. Therefore the study of the physics and chemistry of surfaces is crucial. Surface physics can be defined as a branch of science which deals with atomic arrangements at surfaces of solids and their mechanical, electronic and chemical properties.

The understanding of surface phenomena and surface properties require the answer to several questions. What kind of atoms are at a surface? What is the atomic structure and chemical composition of a surface? Where is the location of atoms or molecules on a surface? What are the electronic and vibrational properties of a surface? What happens to the surface by adsorbing atoms or molecules on a surface? How strongly do atoms or molecules stick to a surface?

To answer these questions surface experiments are conducted using different surface analysis techniques; a single technique is not adequate. For example, to get insight into the chemical composition of a surface both X-ray photoelectron spectroscopy (XPS) and Auger electron spectroscopy (AES) can be used. However, Scanning tunneling microscopy (STM) and low energy electron diffraction (LEED) are suitable to elucidate the surface structure. The later two will be explained in detail in this chapter as they have been used in the experiments of this thesis [1, 2].

Surfaces have been studied extensively since 1970s, and a large number of techniques have been developed to probe their structure, electronic and vibrational properties. The early focus of surface studies was on a single crystal metal surfaces. Following this, semiconductor surfaces were widely explored. Surface of alloys and intermetallic metals were not widely explored until the discovery of quasicrystals in 1982.

Quasicrystals are predominantly inter-metallic compounds which show long-range order with lack of periodicity and translational symmetry and often possess classically forbidden rotational symmetry such as five-fold and ten-fold symmetry. They were first discovered by Dan Shechtman [3] who was awarded the 2011 Noble Prize in chem-

istry for the discovery [4]. Quasicrystals have been studied intensively because of their unusual physical properties (brittle, hard, low electrical and thermal conductivity for Al-rich quasicrystals [5, 6, 7]) and surface properties (low coefficient of friction, low adhesion, high corrosion resistance, non-sticking behaviour) [6, 7, 8]. Due to their intriguing properties quasicrystals have potential applications as thermal barriers, hydrogen storage materials, coating materials and catalysts [6, 9]. Moreover, they have been used as a template to grow metallic and molecular thin films [10, 11, 12].

Since the discovery of quasicrystals [3], their surfaces have been an intense area of research. Before the discovery of the binary *i*-Cd-Yb quasicrystal [13, 14], whose basic building block is a rhombic triacontahedral (RTH) cluster [15], surface studies were limited to Al-based quasicrystals [16], whose basic building blocks are Mackay and Bergman clusters [17]. The new binary quasicrystal also showed novel physical properties such as large electronic specific heat coefficient and high magnetoresistance [18, 19].

The *i*-Cd-Yb quasicrystal has attracted great attention because of the lack of chemical disorder in the structure and large number of related approximants that have been found. The study of Cd-Yb surfaces has opened up a new area of investigation in the surface science of quasicrystals. Samples containing Cd cannot be prepared in ultra-high vacuum (UHV) because of high vapour pressure of Cd [20]. This obstacle has been circumvented by replacing Cd with equal amounts of Ag and In yielding new ternary *i*-Ag-In-Yb quasicrystals. In addition to the quasicrystal phase, different crystalline phases such as Ag-In-Yb 1/1 and Ag-In-Yb 2/1 approximants were also discovered in this system [21]. Refer to Chapter two Section 2.6 for explanation of 1/1 and 2/1 approximants. Moreover, replacing Yb with other rare earth elements generates further crystalline approximants such as Ag-In-Gd, Ag-In-Tb [22] and Ag-In-Eu [23].

Crystalline approximants are metallic compounds whose chemical composition and atomic structure are close to their parent quasicrystals [5, 6, 24, 25]. However, they possess a large (few hundreds of atoms) periodic unit cell [9]. Crystalline approximants play a crucial role in understanding the structure of quasicrystals because of their similarity with quasicrystals and their structure can be solved using conventional structure analysis techniques [23, 26].

An icosahedral Ag-In-Yb quasicrystal and Ag-In-RE 1/1 approximant samples have been used for surface studies in this thesis. The five-fold surface has been used as a template to grow metallic Bi and In films [27]. The goal of this work is to compare thin film formation of Bi and In on this surface, which is different structurally and chemically from Al-based quasicrystals. When these elements were deposited on an Al-based quasicrystal surface, Bi formed only a pseudomorphic quasicrystalline monolayer, but In did not show any order. It will be interesting to see how the structure and chemistry of the substrate influence the film formation. The structure of Ag-InTb,

Ag-In-Gd and Ag-In-Yb approximant surfaces are also studied here [28, 29]. This is to understand the structure of these surfaces and to compare their surface terminations to those of related quasicrystals. Once these surfaces are understood they can be used as templates to grow metallic or molecular thin films.

The work is done with our collaborators from Japan and France. For example, the Ag-In-Gd and Ag-In-Tb approximant samples were grown by our collaborator Dr. Ryuji Tamura from Tokyo University of Science, Noda, Japan and Ag-In-Yb approximant and quasicrystal sample were grown by Dr. Can Cui and Prof. An Pang Tsai from Tohoku University, Sendai, Japan. Regarding data collection, few STM images and LEED data of Ag-In-Tb approximant and STM and LEED data of In epitaxy on the five-fold surface of i-Ag-In-Yb quasicrystal were collected with our collaborators Dr. Vincent Fournée and Dr. Julian Ledieu from the Jean Lamour Institute, Université de Lorraine, Nancy, France.

1.2 Thesis Structure

Chapter Two contains a brief history of quasicrystals and approximants. The different types of quasicrystals are also mentioned. The discovery, formation and structure of the icosahedral Ag-In-Yb quasicrystal and related 1/1 approximants are discussed in detail. A brief introduction of Penrose and Girih tilings is also given.

Chapter Three details the experimental techniques that have been employed in this thesis. An introduction to Ultra High Vacuum (UHV) technology (components and advantages of UHV) is also presented. Sample preparation, surface techniques such as scanning tunneling microscopy (STM) and low energy electron diffraction (LEED) are described. The chapter ends with a brief description of thin film deposition.

Chapter Four presents a structural study of the surfaces of three different 1/1 approximants: Ag-In-Tb, Ag-In-Gd and Ag-In-Yb. Using the STM and LEED, the surface structure of these three 1/1 approximants is studied and compared. The structure of the five-fold surface of the i-Ag-In-Yb quasicrystal is reviewed here as well.

Chapter Five summarises thin film deposition on the surface of quasicrystals. It also details the study of the growth of a Bi film on the five-fold surface of the i-Ag-In-Yb quasicrystal using STM.

Chapter Six deals with STM and LEED data of In growth on the five-fold surface of the i-Ag-In-Yb quasicrystal.

Chapter Seven provides a brief summary and conclusions of the work of the thesis.

Chapter 2

Quasicrystals and Approximants

2.1 Introduction

This chapter provides a brief history of the discovery of quasicrystals and the different types of quasicrystal are also described. The icosahedral Ag-In-Yb quasicrystal is discussed in detail as its five-fold surface has been used as a template to grow quasicrystalline metallic films in this thesis. The structure Ag-In-RE (RE = Tb, Gd, and Yb) 1/1 approximants also described as their surfaces are investigated in this thesis.

2.2 A Brief History of Quasicrystals

Based on their structure solids are classified into two different classes: *crystals* which have a regular periodic three dimension pattern of atoms and *amorphous* solids in which atoms are arranged without any regularity and periodicity [30, 31]. However Dan Shechtman's discovery [3] introduced a new class of solids which differ from both amorphous and crystalline solids [6, 9] and they were dubbed *quasicrystals*, a shorthand form of 'quasiperiodic crystals' [32].

In 1982, Dan Shechtman was a visiting scientist at the National Bureau of Standards in Washington DC, USA. He was studying the structural effect of changing the amount of Mn in aluminium-manganese alloys using transmission electron microscopy (TEM). He observed that some grains showed sharp peaks characteristic of a three dimensional icosahedron which has twelve five-fold axes [5, 33].

The discovery was controversial and shook the crystallographic world. In conventional crystallography, a crystal has a rotational symmetry property in which, lattice maps onto itself after rotation through the angle $2\pi/n$; it is mathematically proven in solid state physics text books (for example *Solid State Physics* by S. O. Pillai [34]) that n =1, 2, 3, 4, and 6 are the only allowed values, whereas $n = 5$ or $n > 6$ are forbidden symmetries for crystals [33].

This can be demonstrated using a triangle or hexagon (also square, rectangle, diamond and oblique) tile as a unit cell. As shown in the Fig.2.1(a), one can tile a plane

without any overlapping and creating any gaps and build a lattice in which all unit cells are identical and have the same surroundings. However, such a lattice or complete tiling can not be obtained using unit cells or tiles with forbidden symmetries such as pentagons, heptagons, octagons and decagons (see Fig.2.1(b)) [35].

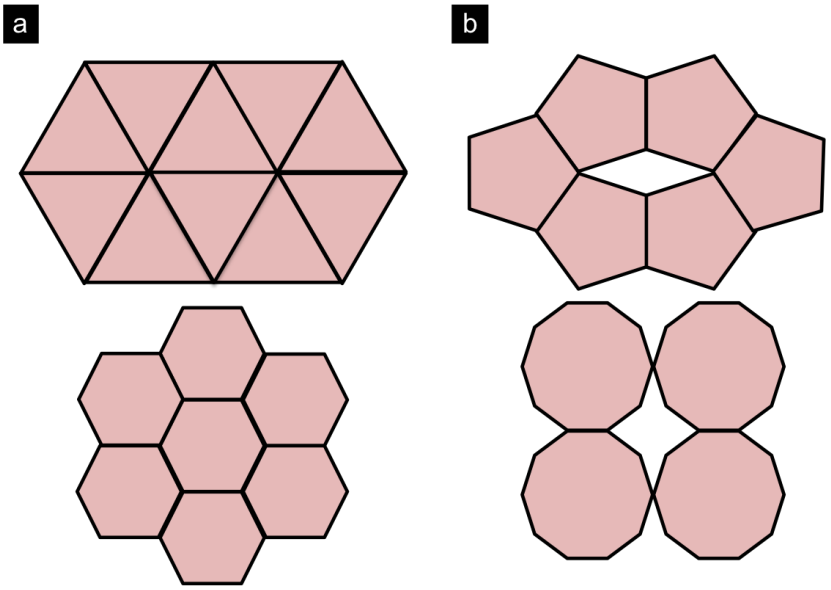

Figure 2.1: Depicts (a) allowed rotational symmetries, (b) disallowed rotational symmetries in conventional crystallography.

Therefore, the discovery was dismissed by many notable crystallographers including the double Nobel prize winner Linus Pauling because he thought that this diffraction pattern resulted from twinning, e.g. a combination of five crystals rotated by 72° relative to each other [36]. His discovery was even rejected by The Journal of Applied Physics [37]. However, Shechtman defended his work vigorously and it was published in Physical Review Letters in 1984 [3], and eventually Shechtman was awarded the 2011 Nobel prize in Chemistry [4]. In parallel with Shechtman's work, a metallic alloy of twelve-fold rotational symmetry was discovered in Switzerland [38]. Later on, eight-fold [39] and ten-fold [40] symmetry quasicrystals were reported. Eventually, the discovery of hundreds of quasicrystals removed all doubts of existence of quasicrystals. This caused the International Union of Crystallography to redefine the crystal as 'any solid with an essentially discrete diffraction pattern' [41].

At the beginning, rapid quenching was used to prepare quasicrystals and as a result a few micron-sized single-grain samples were made. These single-grains were small and metastable so it was difficult to study physical and structural properties [5]. It was thought that all quasicrystals might be metastable or non-equilibrium phases [35]. However, Dubost *et al.* and Tsai *et al.* changed this paradigm when they reported stable (Al_6CuLi_3) and (Al-Cu-Fe) quasicrystals of macroscopic size in 1986 and 1987

respectively [42, 43, 44].

Since then, hundreds of quasicrystals with different composition and symmetries have been discovered. Aluminium (Al) is the one of the most common components and is present in 70 % of known quasicrystals. Icosahedral and decagonal quasicrystals represent about 82 % and 16 % of known quasicrystals [5, 6]. In addition to solid phases, quasicrystals have also been found in liquid crystals [45], polymers [46, 47], perovskite thin films [48] and colloids [49, 50]. A natural quasicrystal ($Al_{63}Cu_{24}Fe_2$) has also been reported which was found in the Koryak Mountains, in Siberia [51, 52, 53, 54].

In summary, quasicrystals predominantly can be defined as intermetallic compounds (binary, ternary or quaternary) which possess long range order with a lack of translational symmetry and often show classically forbidden rotational symmetries such as five-fold, eight-fold, ten-fold and twelve-fold.

2.3 Basic Quasiperiodic Concepts

A non-periodic mathematical construction can be utilised to gain insight on the structure and atomic order in quasicrystals. The one-dimensional Fibonacci sequence and the two-dimensional Penrose tiling are the most common examples of non-periodic constructions [5].

2.3.1 Fibonacci Sequence

The Fibonacci sequence is the sequence of numbers that starts with 0 and 1 in which each new number is the sum of two previous numbers [33].

$$f_n = f_{n-1} + f_{n-2} \tag{2.1}$$

0, 1, 1, 2, 3, 5, 8, 13, 21,.....

The limiting value of the ratio of two successive numbers of the Fibonacci sequence gives the golden ratio (τ) as the sequence approaches infinity;

$$\lim_{n\to\infty} \frac{f_{n+1}}{f_n} = \tau \tag{2.2}$$

where τ is given by;

$$\tau = \frac{1+\sqrt{5}}{2} = 1.618..... \tag{2.3}$$

This sequence can be used as model structure for a one-dimensional quasicrystal which is aperiodic but perfectly ordered. A one-dimensional quasicrystal can be deduced from a two-dimensional periodic lattice by the cut and project method as follows; A two dimensional system of physical space X$\|$ and orthogonal space X$\perp$ is rotated

in the two dimensional hyperlattice (h_x and h_y) by an angle α. The rotation continues until the tangent of α equals the golden ratio τ ($\tan\alpha = \tau$). As a result of rotation the X$\parallel$ axis cuts the hyper lattice h_x and h_y axes which are decorated by an object (\) parallel to the X$\perp$ axis. The atomic positions are the points where (\) cuts the X$\parallel$ axis and these points are highlighted with circles ($\circ$) as shown in the Fig.2.2 [33].

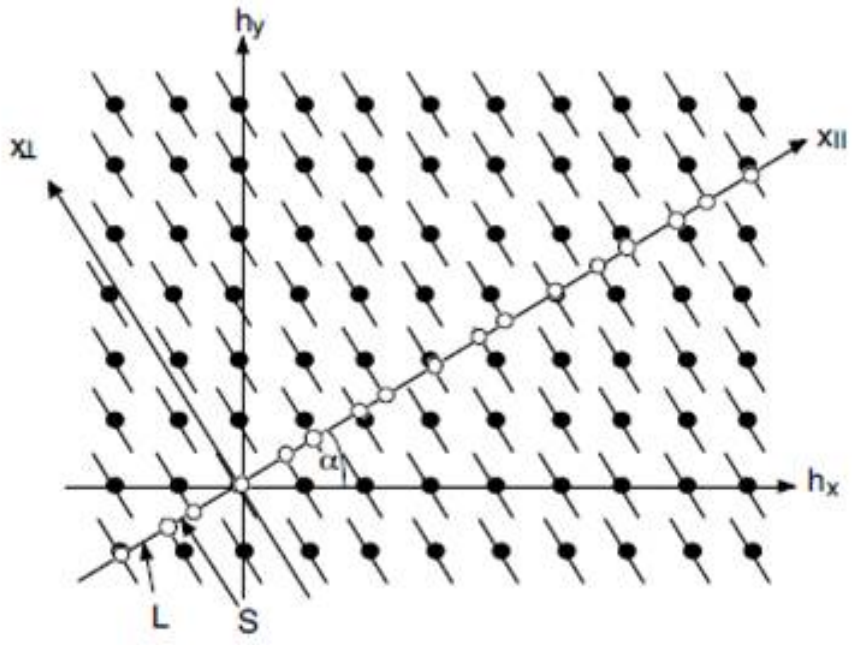

Figure 2.2: Generation of one dimensional quasicrystal from two dimensional hyperlattice, reprinted from [55].

These sites generate an aperiodic and well-ordered chain which is represented by long L and short S lattice parameters. This chain starts with L then it continues as L is replaced by LS and S by L. This chain is linked to the Fibonacci sequence as the ratio of L to S gives the golden ratio (τ).

L
LS
LSL
LSLLS
LSLLSLSL
LSLLSLSLLSLLS

2.3.2 Penrose Tiling

In 1960s, mathematicians explored the use of several tiles to produce an infinite, non-periodic tiling [56]. Such tilings were discovered using specific matching rules by Sir

Roger Penrose in 1974 [57] and are known as Penrose tilings. The importance of Penrose tilings in solid state physics was realised when quasicrystals were reported [58] because the diffraction pattern of a Penrose tiling shows five-fold and ten-fold symmetries which are very similar to the diffraction pattern of quasicrystals [59]. This makes the Penrose tilings a possible model for the structure of quasicrystals [33].

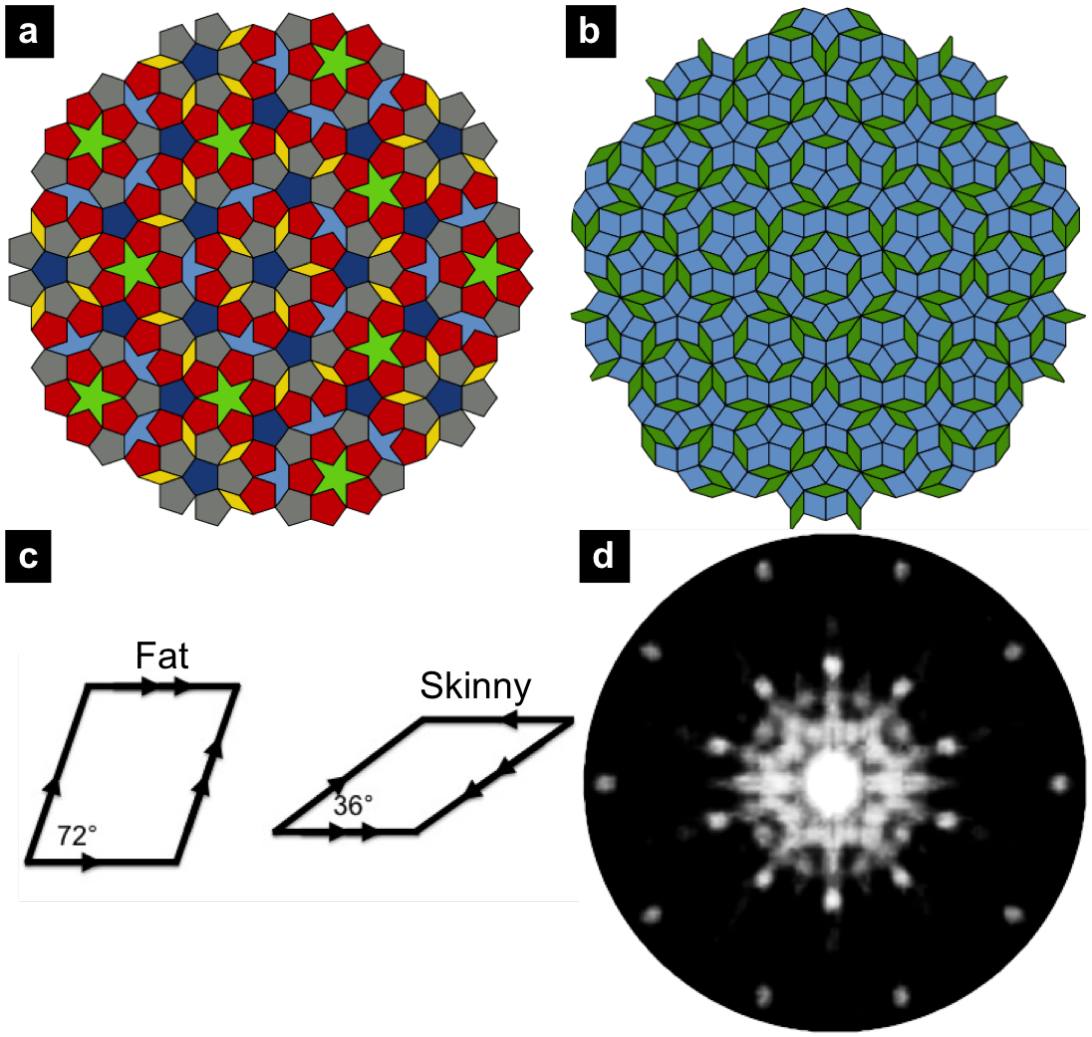

Figure 2.3: (a) P1 Penrose tiling. (b) P3 Penrose tiling. (c) Fat and skinny rombus. (d) FFT of P3 Penrose tiling (b).

Penrose used more than one shape to tile a plane aperiodically as it is impossible to make such a tiling with a single shape. There are three different types of Penrose tilings: P1, P2 and P3. The P1 Penrose tiling is the first tiling Penrose discovered in 1974 which comprises of four different shapes: pentagon, star, thin rhombus and a boat. Fig.2.3(a) shows the P1 tiling. The P2 tiling consists of two different shapes of tiles known as kites and darts.

The P3 tiling consists of two different rhombi (known as fat and skinny) with interior

angles $3\pi/5$ and $2\pi/5$ and $8\pi/10$ and $2\pi/10$ respectively as shown in the Fig.2.3(c). These shapes can be tiled together to produce either a periodic tiling or a non-periodic tiling. To produce a non-periodic tiling a specific matching rule must be applied. The rule states that the rhombi can join if the arrows of their edges match. The ratio of numbers in a non-periodic tiling of thick to thin rhombus is equal to the golden ratio (τ) [60, 61]. Fig.2.3(b) shows the P3 tiling.

The Fourier transform of Penrose tiling P3 shown in Fig.2.3(d) exhibits ten-fold symmetry which is similar to the diffraction patterns observed in icosahedral quasicrystals [62, 63]. The Penrose tilings have been overlaid on quasicrystal surfaces to classify surface features and to confirm the long-range order of surfaces [64]. The Penrose P1 tiling is used in the work of chapter five and six to describe the structure of Bi and In films.

Girih Tiles

Islamic architects used tiles to decorate mosques and buildings. These tiles are called girih tiles and are: a regular pentagon, a regular decagon, an elongated hexagon, a rhombus and a bow tie (Fig.2.4). These tiles have similar geometric features; for example they have the same edge length and their interior angles are multiples of $\pi/5$. All girih tiles except the pentagonal tile have reflection symmetry through two perpendicular lines and all tiles are decorated by lines which intersect the midpoint of edges at 72° and 108° [65].

Lu and Steinhardt [65] examined thousands of photos taken from mosques of different countries including Pakistan, Uzbekistan, Turkey, Iran and Iraq where girih tiles were used for decoration. They showed that the decagonal girih pattern is the most popular since 1200 and almost all the patterns were periodic. However, they found a girih pattern which was used to decorate the Darbi-i Imam shrine, in Isfahan, Iran, built in 1453, which shows quasicrystalline symmetry. A photograph of the half spandrel, which exhibits decagonal motifs with two different length scale, is shown in Fig.2.5(a). This is a telltale of a quasicrystalline pattern [65].

After examination of the photo Lu found that the girih pattern can be mapped onto the Penrose tiling including a few defects which could be made by workers during construction or repair. Lu suggested that the architects had understood quasicrystals since the 15^{th} century [65].

Lu's paper sparked a dispute over who first discovered quasicrystalline patterns in Medieval Islamic Architecture [66]. Emil Makovicky had studied girih patterns for two decades at the University of Copenhagen, Denmark and analysed a girih pattern on a tomb in Maragha in Iran which was built in 1197. He concluded that the pattern can map onto Penrose tiles and he published his work in a book about five-fold symmetry in 1992 [67]. Fig.2.5(b) shows a photograph of the tomb in Maragha. Levine of the Israel

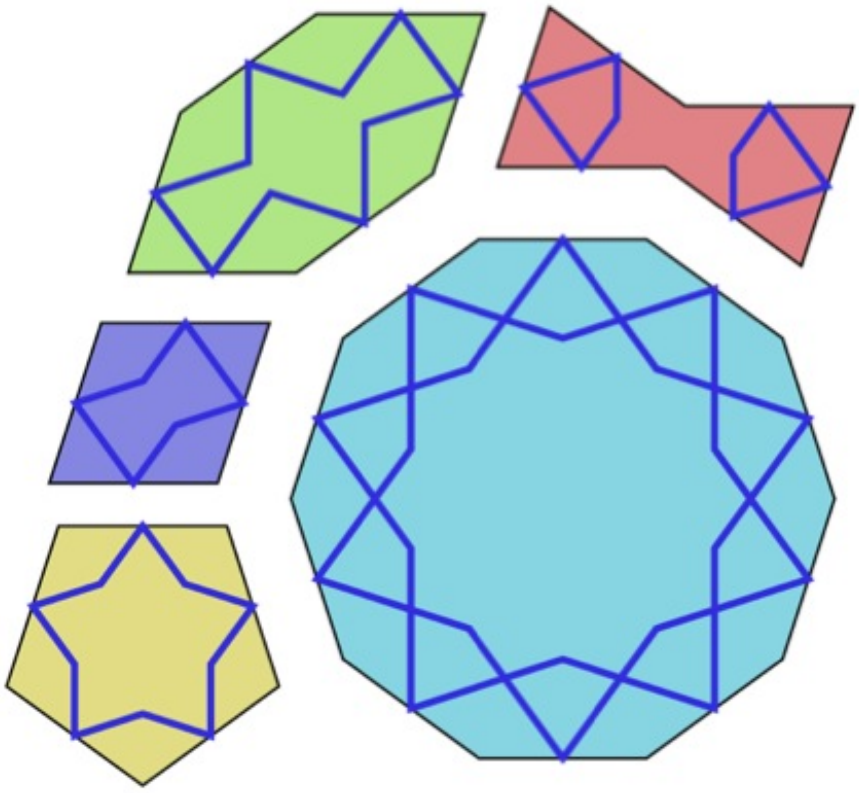

Figure 2.4: Girih tiles, reprinted from [65].

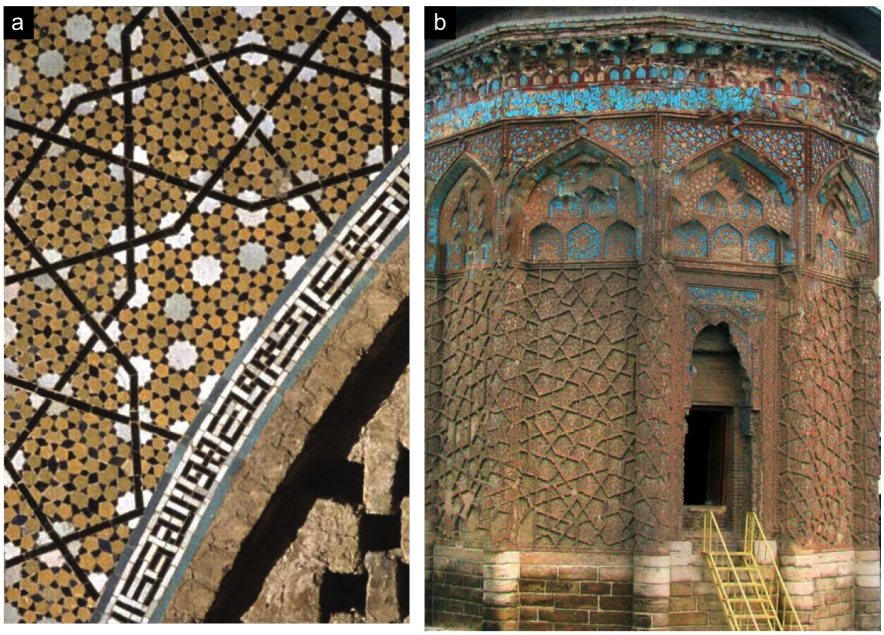

Figure 2.5: (a) Photograph of half of the spandrel of Darbi-i Imam shrine, in Isfahan, Iran 1453. (b) Photograph of the tomb in Maragha in Iran, built in 1197.

Institute of Technology in Haifa and Socolar of the Duke University in Durham, North Carolina agree that Makovicky deserves credit for the discovery and they disagree that architects in the 15^{th} century truly understood quasicrystals as Lu claims [66].

2.4 Types of Quasicrystals

There are several different classes of quasicrystals [68] and there are several ways to classify them [7]. They can be classified according to their structure or their thermodynamic stability or according to majority components [69].

- According to their structure quasicrystals can be classified into two different groups:
    1. Quasiperiodic in two dimensions, where one periodic direction is perpendicular to quasiperiodic layers. This includes octagonal, decagonal and dodecagonal quasicrystals.
    2. Quasicrystals in three dimensions, including icosahedral quasicrystals with five-fold symmetry.
- According to their thermal stability quasicrystals are classified into:
    1. Stable quasicrystals which are formed by slow cooling.
    2. Metastable quasicrystals which grown by melt-spinning or crystallisation of the amorphous phase.
- According to majority components they can be named as Al-, Mg-, Zn-, Cd-, Ti-, and Zr- based quasicrystals [69].

As the quasicrystal sample which has been used to collect the data for this thesis is the icosahedral (i-Ag-In-Yb) quasicrystal, the icosahedral quasicrystals will be described.

2.5 Icosahedral Quasicrystals

Icosahedral quasicrystals are quasicrystals which are quasiperiodic in three dimensions (3D) with no periodicity along any direction and they have three high symmetry axes: two-fold, three-fold and five-fold [7, 9]. The two-fold and three-fold axes make 31.7° and 37.4° angles with the five-fold axis respectively [9]. Fig.2.6 shows an example of the icosahedral $Ho_9Mg_{34}Zn_{57}$ quasicrystal, exhibiting facets along two-fold, three-fold and five-fold axes [70].

Three different types of icosahedral quasicrystals are theoretically possible which are primitive (P), face-centred (F) and body-centred (I). Only P- and F-types are observed

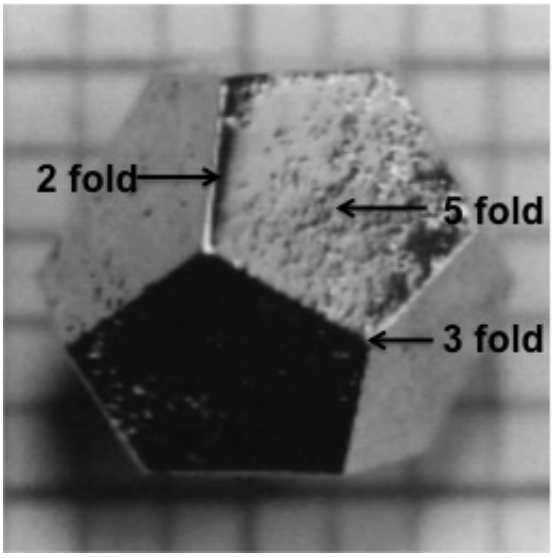

Figure 2.6: Macrograph of icosahedral $Ho_9Mg_{34}Zn_{57}$ quasicrystal. Reprinted from [70].

experimentally [71]. The icosahedral quasicrystals can be classified into three other classes according to the structure of icosahedral clusters (their building blocks) derived from their related approximants Al-Mn-Si, Mg-Al-Zn and Cd-Yb. Approximants are metallic compounds whose chemical composition and atomic structure are close to their parent quasicrystals and possess large periodic unit cells. The Mackay cluster is the building block of the first class. This cluster has three concentric atomic shells of fifty four atoms, with icosahedral symmetry. The first shell is an icosahedron consisting of twelve Al/Si atoms, the second shell is an icosidodecahedron composed of thirty Al/Si atoms and the third shell is a larger icosahedron of twelve Mn atom. The radii of these three shells are 0.245 nm, 0.470 nm and 0.483 nm respectively. The basic structural unit of the second class is the Bergman cluster of one hundred and four atoms which has four concentric atomic shells with icosahedral symmetry. The four shells are an icosahedron of twelve Al/Cu atoms, a dodecahedron of twenty Li atoms, a larger icosahedron of twelve Al/Cu atoms and a truncated icosahedron of fifty six atoms, with 0.248 nm, 0.450 nm, 0.493 nm and 0.678 nm radius respectively [71, 72].

The building block of the third class of icosahedral quasicrystals is the so-called rhombic triacontahedron (RTH) cluster. The RTH cluster consists of five successive atomic shells (Fig.2.7), starting with the innermost shell of four Cd atoms making a disordered tetrahedron. The twenty Cd atoms in the second shell making a dodecahedron of radius 0.46 nm. The third shell is an icosahedron of radius 0.56 nm made by twelve Yb atoms. The fourth shell is an icosidodecahedron of radius 0.65 nm formed by thirty Cd atoms. Finally the outermost shell is a rhombic triacontahedron (RTH) of radius 0.78 nm with 92 Cd atoms located on the vertices and mid-edges. The radii are measured along two-fold axis. In contrast to the Mackay and Bergman clusters which

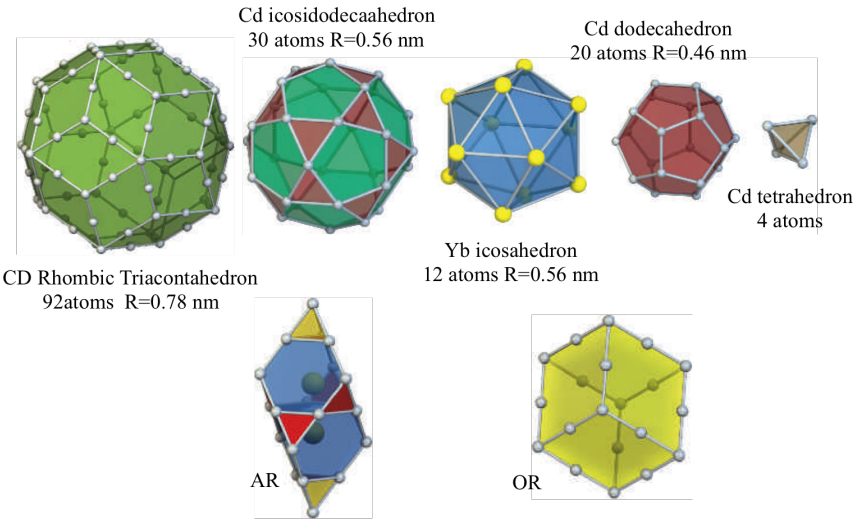

Figure 2.7: Rhombic triacontahedron (RTH) cluster which is defined by five successive atomic shells. Starting with a tetrahedron with 4 Cd atoms in the centre, twenty Cd atoms make a dodecahedron for the second shell, an icosahedron of twelve Yb atoms in the third shell whereas the fourth shell is formed by an icosadodecahedron of thirty Cd atoms. Finally the RTH shell which has 92 Cd atoms. The units shown underneath are an acute rhombohedron (AR) and obtuse rhombohedron (OR), which fill the space between RTH clusters. Reprinted from [15].

they have nothing in the centre, the RTH cluster has a tetrahedron of four Cd atoms which breaks the icosahedral symmetry [15, 73]. The quasicrystal and approximant samples used in this thesis belong to the third class.

2.5.1 The Binary *i*-Cd-Yb Quasicrystal

Discovery

Before discovery of the binary icosahedral (i-Cd-Yb) all quasicrystals were composed of more than two elements. Indeed it was thought that the icosahedral quasicrystals must have at least three elements to form and it was also thought that icosahedral quasicrystals are only formed by metals of the right-hand side of the Periodic Table [25]. The discovery of binary icosahedral (i-Cd-Yb) quasicrystal [13, 14] banished these notions.

Tsai *et al.* were preparing Cd-Mg-RE (RE refers to rare earth metals) quasicrystals and they were decreasing the amount of Mg and testing the phase diagram. By doing this, they found an unknown phase of $Cd_{5.7}Yb$ with a melting point of 636°C. Following this, the phase $Cd_{5.7}Yb$ was prepared from pure elements of Cd (99.99 %) and Yb (99.9 %). The raw materials were first put into an Al_2O_3 crucible and then the crucible was sealed into a quartz tube with an Ar atmosphere. Then sealed samples were put into an induction furnace. Then materials were annealed for 100 hours at 400°C.

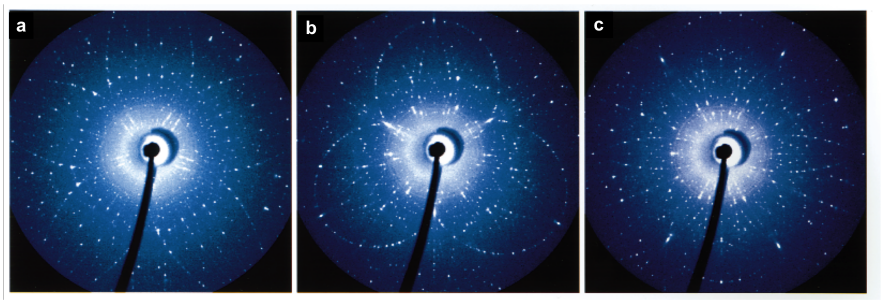

Figure 2.8: (a), (b) and (c) are Transmission Laue X-ray diffraction patterns of a single grain of the $Cd_{5.7}Yb$ quasicrystal along 5-fold, 3-fold and 2-fold axes respectively. Reprinted from [13].

The phase was identified as a quasicrystal by powder x-ray diffraction patterns and the selected area electron diffraction patterns showed the phase to be a primitive icosahedral one. The phase was a thermodynamically stable quasicrystal as it was evident in the solidified and fully annealed state [13, 14]. Fig.2.8 shows the transmission Laue X-ray diffraction patterns of a single grain of the $Cd_{5.7}Yb$ quasicrystal along 5-fold, 3-fold and 2-fold axes respectively.

Formation

Hume-Rothery *et al.* were able to establish some rules to summarise the formation of the structure of intermetallic compounds during their investigations on copper and silver. The rules concern atomic size factor, valence electron concentration and electronegativity [74].

- The characteristic ranges of the valence electron concentration (e/a) will give a definite structure of compounds. The number of valence electrons in the alloy per number of atoms (e/a) is given by;

$$e/a = Z_A(1 - c_B) + Z_B c_B \tag{2.4}$$

  where Z_A and Z_B are the atomic number of species A and B respectively.

- The atomic size factor is defined by;

$$\delta = (r_A - r_B)/r_A \tag{2.5}$$

  where r_A and r_B are the atomic radii of atoms A and B respectively. If the atomic size of atom B differs from that of atom A by more than 15% the structure will be unstable.

The formation of quasicrystals have been studied through valence electron concentration (e/a) [75], and it is found that stable icosahedral quasicrystal phases are subject to this rule as they have a common valence electron concentration (e/a) [14]. The (e/a) is found to be 1.75 for Al-transition metals and 2.1 for Al-Zn-Mg [76].

Similarly the formation of the stable binary icosahedral $Cd_{84}Yb_{16}$ quasicrystal is also subject to the (e/a) Hume-Rothery rule. Cd and Yb are both divalent so the (e/a) for binary stable icosahedral $Cd_{84}Yb_{16}$ is found to be 2.0. and the formation of the quasicrystal is also dominated by the atomic size factor. The atomic diameters of Cd and Yb are very close to each other (0.388 nm and 0.1396 nm respectively). Of the rare earth elements, Eu is also divalent but it does not make an icosahedral quasicrystal with Cd because its atomic diameter (0.408 nm) is slightly larger than Yb and Cd [14].

Structure

Determination of the structure of a crystal is essential to understand its physical properties. Since icosahedral quasicrystals are aperiodic in three dimensions and do not have any periodic axis, it is impossible to determine the structure using two dimensional mapping techniques such as high resolution electron microscopy (HREM) [77]. Yamamoto *et al.* tried to determine the structure of the icosahedral *i*-Al-Pd-Mn quasicrystal but because of the chemical disorder it was difficult to find the contrast between diffraction spots [78]. The discovery of binary icosahedral quasicrystals [13, 14] was an important milestone in quasicrystal research because of their structural simplicity and the existence of approximants [79]. The discovery of binary quasicrystals made it possible to obtain quasicrystals free of chemical disorder which makes the structure determination easier. For the first time, a complete model structure for a binary icosahedral quasicrystal *i*-Cd-Yb was obtained by Takakura *et al.* [15].

The detail of the structure determination is beyond the scope of this thesis and can be read in reference [15]. The structure is described by RTH clusters which are arranged aperiodically. 93.8% of the atoms of the structure belong to RTH clusters and the remaining space between RTH clusters is filled by two additional building blocks which are obtuse and acute rhombohedra (shown in Fig.2.7). The atoms of the rhombohedra are known as 'glue atoms' [15].

2.5.2 The Discovery of Ternary *i*-Ag-In-Yb Quasicrystal

The fascinating discovery of binary *i*-Cd-Yb systems drew the attention of scientists because of their lack of chemical disorder and the existence of related approximants. However, surface studies on a quasicrystal in the Cd-based system were not performed because both quasicrystals and approximants containing Cd are very reactive and unstable in air. Cd itself has a high vapour pressure so surfaces of Cd containing systems can not be prepared under ultra-high-vacuum for surface studies [20]. This obstacle was

circumvented by replacing Cd with equal amount of Ag and In which are neighbours to Cd in the Periodic Table. This replacement yielded a new stable ternary icosahedral Ag-In-Yb quasicrystal [21]. In contrast to the *i*-Cd-Yb quasicrystal, the ternary *i*-Ag-In-Yb quasicrystal is stable in air and has a low vapour pressure which helps sample preparation even under UHV [20].

Similar to the parent binary *i*-Cd-Yb quasicrystal, the ternary *i*-Ag-In-Yb quasicrystal is dominated by both the valence electron per atom (e/a) and atomic size Hume-Rothery rules. Yb, Ag and In are divalent, monovalent and trivalent respectively, so the (e/a) remains 2.0. The atomic diameters of Ag and In are 0.290 nm and 0.332 nm respectively which gives the average atomic diameter of 0.311 nm close to the Cd diameter 0.314 nm. Therefore the ternary quasicrystal has the atomic size ratio $d_{0.5Ag+0.5In}/d_{Yb} \approx 0.8$, the same as its parent binary quasicrystal d_{Cd}/d_{Yb} [20, 21].

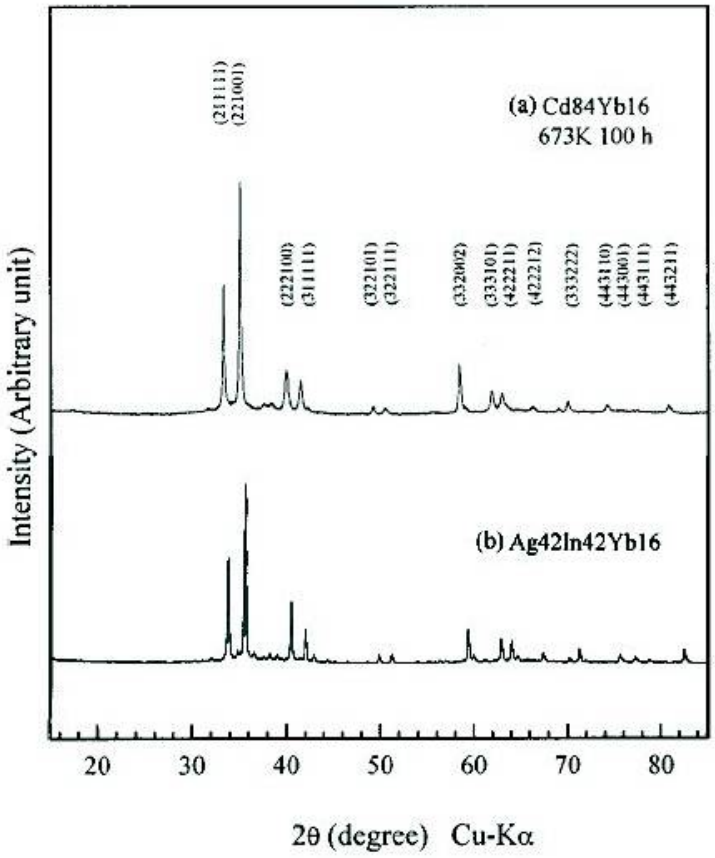

Figure 2.9: X - ray diffraction patterns of *i*-$Cd_{84}Yb_{16}$ and *i*-$Ag_{42}In_{42}Yb_{16}$ quasicrystals. Reprinted (a) from [14] and (b) from [21].

X-ray diffraction using a Cu Kα source and selected area electron diffraction (SAED) were used to identify the phase of the sample. The diffraction patterns of the *i*-Ag-In-Yb quasicrystal are found to be the same as the diffraction patterns of the *i*-Cd-Yb

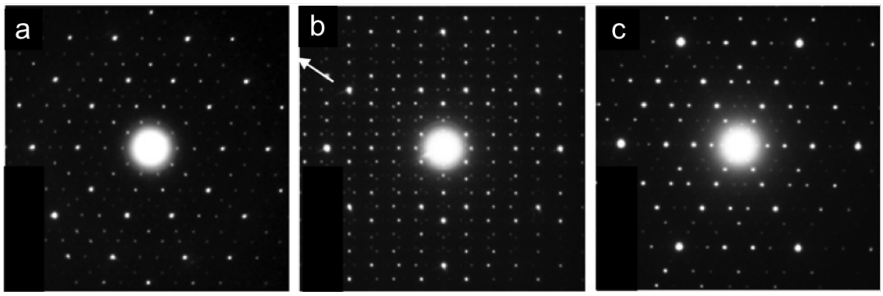

Figure 2.10: SAED patterns of *i*-Ag-In-Yb quasicrystals along (a) five-fold, (b) two-fold and (c) three-fold directions. Reprinted from[20].

quasicrystal. Fig.2.9 shows the diffraction pattern for both *i*-Cd-Yb and *i*-Ag-In-Yb quasicrystals. The indexing method proposed by Elser (1985) [80] was used to assign the diffraction peaks and it was found that the new alloy is only composed of an icosahedral quasicrystal [21]. The selected area electron diffraction (SAED) patterns of the Ag-In-Yb alloy taken along five-fold, two-fold and three-fold directions, shown in Fig.2.10, confirm the formation of an icosahedral quasicrystal [20].

Crystal Growth

Ohhashi *et al.* found a phase diagram for the Ag-In-Yb alloy as shown in Fig.2.11. Fig.2.11(a) shows the compositional range for the icosahedral quasicrystal and two other different phases known as 2/1 and 1/1 approximants. The formation of phases extends along the Ag and In axes whereas it is limited along the Yb axis. Fig.2.11(b) shows a temperature-composition phase diagram along the composition line $Ag_{26+x}In_{74-2x}Yb_x$. The melting points from differential thermal analysis (DTA) measurements were determined to be 890 K, 878 K and 887 K for the icosahedral quasicrystal, the 1/1 and the 2/1 approximants respectively [20]. It was found that the icosahedral phase forms congruently from the melt at 890 K while approximants form via peritectic reaction. Peritectic reaction is a reaction in which a solid phase and a liquid phase form another solid phase at certain composition and temperature.

Based on this phase diagram, the Bridgeman method was used to grow the quasicrystal. A single grain icosahedral quasicrystal in Ag-In-Yb system was successfully grown. This crystal provided an opportunity to study the bulk and surface properties of a P-type icosahedral quasicrystal, as other P-type icosahedral quasicrystals such as *i*-Cd-Yb and *i*-Al-Li-Cu were reactive and unstable in air [20]. Later a centimetre-sized single-grain Ag-In-Yb was synthesised using the Bridgeman method [81], as large single grain quasicrystals are desirable for the study of surface physical properties [26].

The Ag-In-Yb system is found to be a very good candidate for the study of a single grain crystal because the *i*-$Ag_{40}In_{40}Yb_{16}$ quasicrystal is isostructural to its parent *i*-

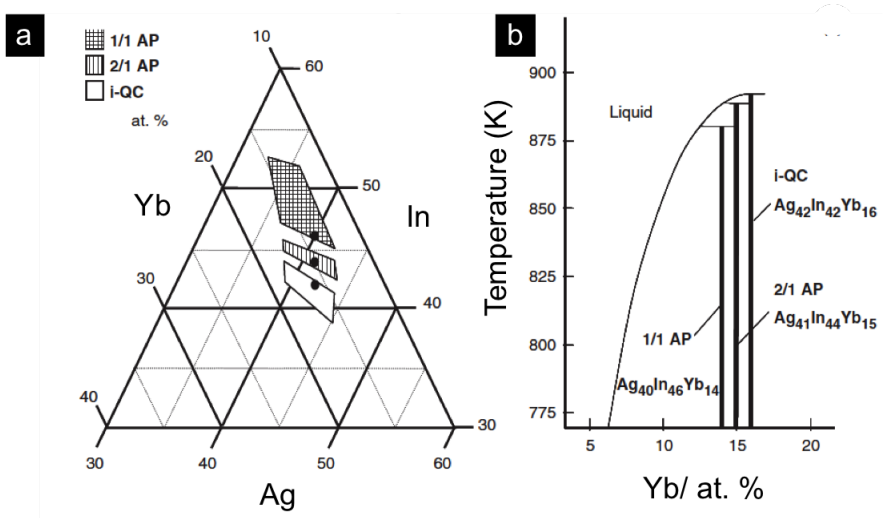

Figure 2.11: (a) Partial isothermal section of Ag-In-Yb system at 823K. (b) Temperature composition section along the composition line $Ag_{26+x}In_{74-2x}Yb_x$. The black dots given in (a) are the compositions which are single phase for each compound. Reprinted from [20].

Cd-Yb quasicrystal, and the most detailed quasicrystal structure model for *i*-Cd-Yb quasicrystal is available. Secondly, two different periodic 2/1 $Ag_{41}In_{44}Yb_{15}$ and 1/1 $Ag_{40}In_{46}Yb_{14}$ cubic approximants whose structure and chemical composition are very close to the *i*-$Ag_{40}In_{40}Yb_{16}$ quasicrystal exist. Finally, crystals of Ag-In-Yb system, which do not have toxic and high vapour pressure elements, are stable in air and in UHV system so they can be easily prepared for experiments [26].

2.6 Approximants

While exploring the structural similarity between known crystalline phases and related quasicrystalline phases, periodic crystals which are closely related to quasicrystalline phases were found. They were termed 'approximants' as the arrangement of their atoms in the unit cell closely approximates the local atomic structures of the quasicrystals. Approximants play a crucial role in understanding the formation, stability, physical properties and atomic scale structure of quasicrystals [24].

There are a number of reasons that make approximants so important in understanding the structure of quasicrystals especially icosahedral quasicrystals. Firstly, the formation of quasicrystals occurs at compositions very close to approximant phases. Secondly, approximants provide a model of the local atomic structure of quasicrystals. Finally, both quasicrystals and approximants possess similar physical properties [24].

The formation of approximant phases is due to phason strain in quasicrystals. To explain that we refer to Fig.2.2. Assume that phason strain rotates the physical space

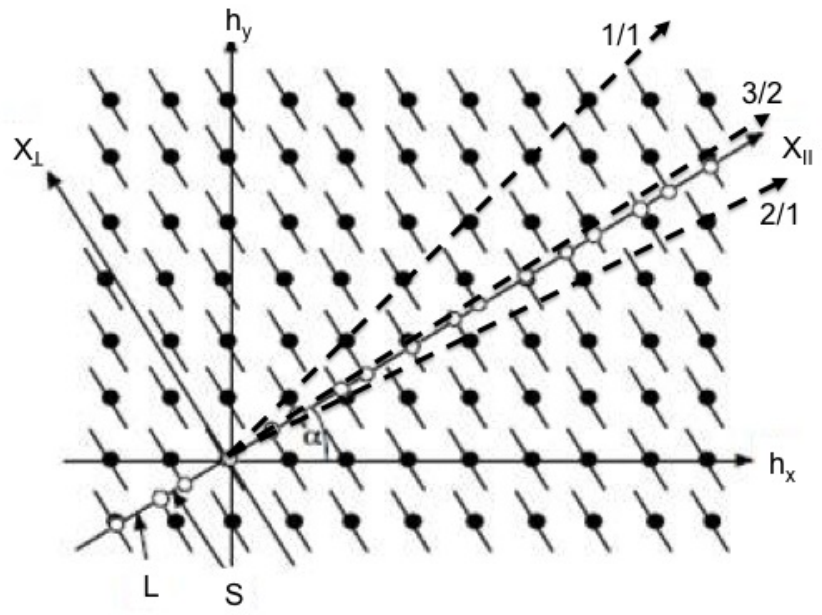

Figure 2.12: Transition of quasicrystalline phase to approximant phases due to phason strain. Reprinted form [55]

such that the slope produces a rational number which approximates the initial slope $1/\tau$ (the slope could be 1/1, 1/2, 2/3, 3/5 or 5/8 as shown in Fig.2.12). At these slopes physical space intersects the atomic surfaces and produces periodic sequences, LSLSLSLSLSLSLS...., LSLLSLLSLLSL..., LSLLSLSLLSLSLLS....., and LSLLSLSLL-SLLSLSL...respectively. These sequences with repeating unit cells LS, LSL, LSLLS and LSLLSLSL respectively yielding 1/1, 2/1, 3/2 and 5/3 approximants. Higher order approximants are even more similar to the correspondent quasicrystals [58, 82].

As mentioned earlier, the replacement of Cd in Cd-Yb system with equal amounts of Ag and In yields a new ternary quasicrystal and related cubic approximants such as the i-Ag-In-Yb quasicrystal and Ag-In-Yb 1/1 and 2/1 approximants. Replacing Yb with other rare earth elements yields new crystalline approximants such as Ag-In-Gd, Ag-In-Tb [22] and Ag-In-Eu [23] 1/1 approximants. The approximant samples used in this thesis are Ag-In-RE 1/1 approximants where RE = Yb, Gd and Tb. The surface structure of these approximants were characterised using STM and LEED. Details will be provided later on.

The structure of both 1/1 and 2/1 Ag-In-Yb approximants which are isostructural to Cd_6Yb 1/1 and $Cd_{5.8}Yb$ 2/1 approximants respectively can be described as a packing of triacontahedral (RTH) clusters. The RTH clusters in both approximants are linked along two-fold and three-fold directions (called b-linkage (length = b)) and c-linkage (length = b ($\sqrt{3}/2$)) respectively) [15]. Fig.2.13(a) shows both b- and c-linkage .

The RTH cluster packs differently in 1/1 and 2/1 approximants. The 1/1 approxi-

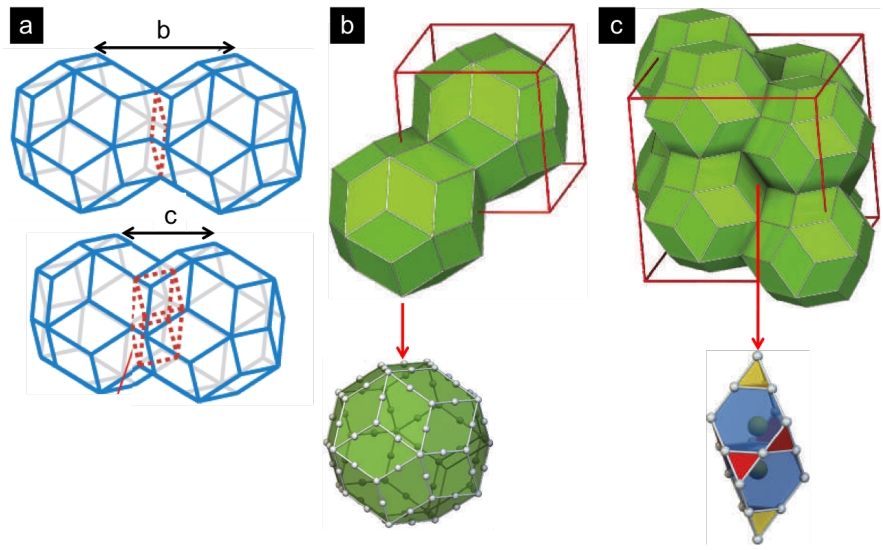

Figure 2.13: Approximant building units and linkages (a) b- and c- linkage along two and three-fold directions respectively. (b) The body-centred-cubic packing of RTH units in the 1/1 cubic approximant. (c) The packing of RTH units in the 2/1 cubic approximant with additional building block (AR). Reprinted from [15].

mant is described by a body-centred packing of RTH clusters as shown in Fig.2.13(b), all atoms belong to the RTH cluster, whereas the 2/1 approximant packing requires additional building blocks to fill gaps between RTH clusters (see Fig.2.13(c)). The additional building block is the acute rhombohedron (AR) which is decorated with two Yb atoms along its long diagonal and Cd atoms on the vertices and edges [82, 83, 84].

Using the self-flux method large single grains of approximant in Ag-In-Yb system were synthesed [26]. Single grains of Ag-In-Tb and Ag-In-Gd 1/1 approximants were also grown using the self-flux method. Fig.2.14 shows macrographs of Ag-In-RE 1/1 approximants (Re =Yb, Tb and Gd).

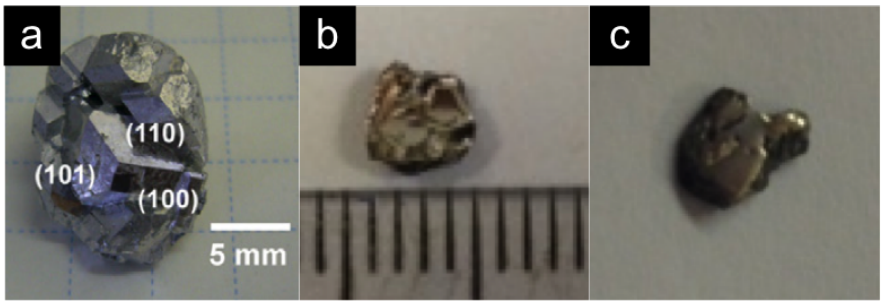

Figure 2.14: Macrographs of 1/1 approximant samples grown with the self-flux method. (a) Ag-In-Yb Reprinted from [26]. (b) Ag-In-Tb and (c) Ag-In-Gd.

Chapter 3

Experimental Techniques

3.1 Introduction

This chapter explains why surface experiments must be performed in an ultra high vacuum (UHV) system. The components of the UHV system are explained in detail. Finally, sample preparation methods and surface analysis techniques such as low energy electron diffraction (LEED) and scanning tunnelling microscopy (STM) are described.

3.2 Ultra High Vacuum (UHV)

To conduct a typical surface experiment and to keep the surface free from contamination during the experiment, an ultra high vacuum (UHV) chamber is required. Ultra high vacuum (UHV) can be defined as a vacuum with the pressure of residual gases below 10^{-9} mbar. Pressure is measured in different units. (Pascal (Pa), Newton/m^2, bar, mbar, Torr, atmosphere (atm), and millimetres of mercury (mmHg)); the relation between them is shown in Table 3.1. Torr and mbar are used to describe vacuum levels. The residual gas pressure affects some experiments and certain experiments need to be performed in a certain pressure regime. Therefore, the division of pressure into different regions become customary in vacuum technology [85] The different degrees of pressure are listed in the Table 3.2.

Table 3.1: Pressure units conversion

	Pa = N/m^2	bar	mbar	Torr = mmHg	atm
Pa	1	10^{-5}	10^{-2}	7.5×10^{-3}	9.87×10^{-6}
bar	10^5	1	10^3	750	0.987
mbar	100	10^{-3}	1	0.750	987×10^{-6}
Torr	133.32	1.33×10^{-3}	1.33	1	1.31×10^{-3}
atm	1.01×10^5	1.013	1013.25	760	1

Table 3.2: Vacuum Regimes

Low Vacuum (mbar)	Medium Vacuum (mbar)	High Vacuum (mbar)	Ultra High Vacuum (mbar)
1 - 10^{-3}	10^{-3} - 10^{-5}	10^{-6} - 10^{-8}	10^{-9}

3.2.1 Gas Flow

The nature of gas flow is one of the characteristics which changes between the regions of pressure. There are different flow regimes in different pressure regions. For example, in low (rough) vacuum region, the gas flow is called continuum (viscous) flow; the continuum flow can be either turbulent or laminar depending on the mutual interaction of the particles. Gas flow is turbulent flow if vortex motion appears or laminar if various layers of the streaming medium slide over each other. In continuum flow, the diameter (d) of the conducting tube is larger than the mean free path (λ) of the particles ($\lambda << d$). However, in the high and ultra high vacuum region, the flow is completely determined by gas-wall collisions and is called molecular flow; the mean free path is greater than the diameter of conducting tube ($\lambda >> d$). In this case gas molecules flow freely without collision. In between rough and high pressure vacuum there is a medium vacuum region. In this region there will be a transition from continuum flow to molecular flow. This kind of flow called transition flow in which the mean free path is similar to conducting tube diameter ($\lambda \approx d$). There will be collisions between gas molecules themselves and with the walls [85, 86, 87]. Laminar , turbulent and molecular flow are shown in Fig.3.1.

3.2.2 Why UHV is Required?

Surface properties of a crystal can only be studied when one can study a clean surface. In order to conduct a typical surface experiment, its essential to get a contamination-free surface and to keep the surface clean during the experiment. This is can be done under UHV [88, 89]. To illustrate how UHV keeps the surface free from contamination, it is worthwhile to put the different parameters which vary with pressure into context using the kinetic theory of gasses.

Mean Free Path (λ)

Mean Free Path (λ) is the distance of which a particle atom, molecule or ion can travel in a system before colliding with other particles. It can be written as;

$$\lambda = \frac{k_B T}{\sqrt{2}\pi\xi^2 P} \tag{3.1}$$

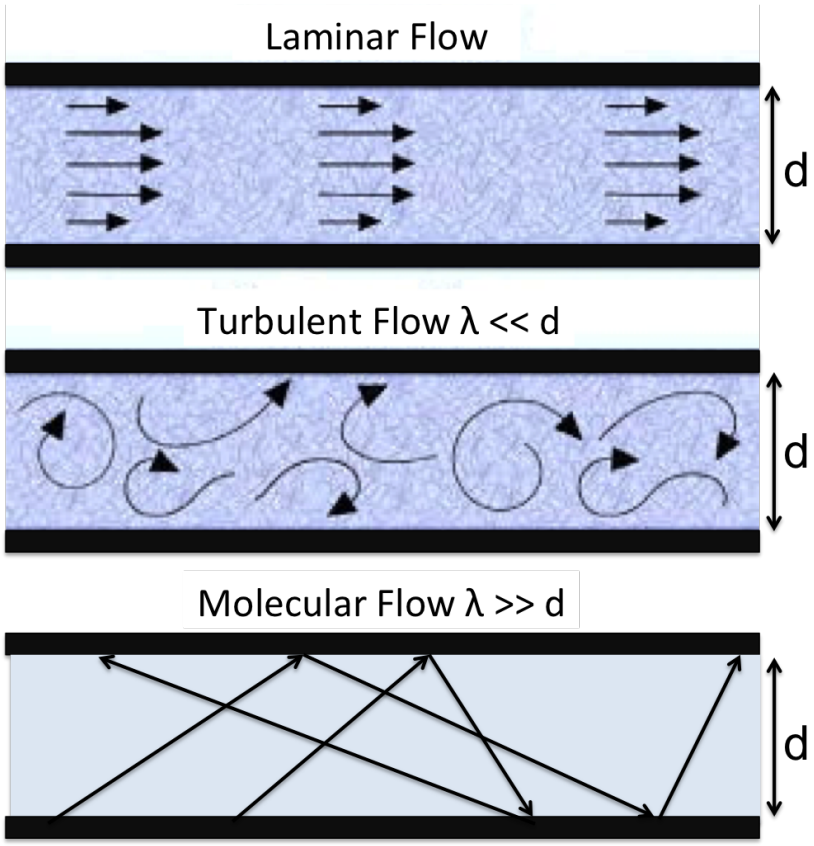

Figure 3.1: Schematic illustration of laminar, turbulent and molecular flow.

where: k_B is Boltzman Constant (1.38×10^{-23} J.K^{-1}) , T is the temperature (K), ξ is molecular diameter and P is pressure of gas molecules in N. m^{-2} [1].

From equation (3.1), the mean free path is inversely proportional to the pressure, which means high pressure generates a shorter mean free path. This leads to collision between gas molecules and has an affect on the surface cleanness.

Incident Flux (Z)

The incident flux (Z) is the number of incident particles per unit time per unit area of the surface. Therefore the incident flux (Z) is related to the density of gas molecules on the surface. Combining the ideal gas and the Maxwell-Boltzman velocity equation together yields the the incident flux (Z) (molecule.m^{-2} s^{-1}).

$$Z = \frac{1}{4} n \bar{c} \tag{3.2}$$

where n is the gas density, obtained from the ideal gas equation as follows

$$n = \frac{N}{V} = \frac{P}{kT} \tag{3.3}$$

where P is pressure (N.m^{-2}), k is Boltzman constant (1.38 $\times$ 10^{-23} J.K^{-1}), T is temperature (K), V is volume (m^3) and N number of gas molecules, and $\bar{c}$ is the average molecular speed which can be estimated from Maxwell-Boltzman distribution gas velocity by;

$$\bar{c} = \sqrt{\frac{8kT}{m\pi}} \tag{3.4}$$

where m is the mass of gas molecule. Putting equation(3.3) and (3.4) into equation (3.2), the incident flux will be;

$$Z = \frac{P}{\sqrt{2\pi m k_B T}} \tag{3.5}$$

or

$$Z = \frac{1}{\sqrt{2\pi k}} \times \frac{P}{\sqrt{mT}} = 1.074 \times 10^{11} \frac{P}{\sqrt{mT}} \tag{3.6}$$

Equation (3.6) shows that the incident flux of gas molecules is directly proportional to the pressure which means high pressure increases the density of particles (molecules, atoms or ions) impinging the surface. This makes the surface contaminated [90, 91].

Time to form a monolayer (τ)

The time (τ) required to form a monolayer of gas molecules on a surface can be expressed as;

$$\tau = \frac{N_\circ}{Z} \tag{3.7}$$

where $N_\circ$ is the number of atoms in a monolayer and Z is the incident flux. A surface has ($N_\circ$) about 10^{15} atom/cm^2. If the the sticking coefficient is assumed to be one, then the surface can only stay clean for a second which is too short to conduct an experiment [1, 92].

Table (3.3) depicts the calculated parameters (λ, Z and τ) for nitrogen (N_2) of molecular diameter (d = 3.7 $\times$ 10^{-10}) at same temperature (300 K) and different pressure regimes. The table shows that at high pressure or low vacuum (1 mbar) the mean free path of molecules is very short which makes the collision rate between molecules themselves and the incident flux too large and the time required to form a N_2 monolayer is extremely short. At this (low vacuum) no surface experiments can be carried out. However, at ultra high vacuum (UHV-10^{-10} mbar) level, the mean free path is large enough (around one hundred thousand meters) and it takes several hours to form a monolayer. This makes it possible to conduct a surface experiment. To summarise, the UHV is very crucial to prepare the clean surface and keep the surface clean during the experiment.

Table 3.3: Calculated parameters (λ, Z and τ) for nitrogen (N_2) of molecular diameter (d = 3.7×10^{-10}) at 300 K.

Pressure (mbar)	λ (m)	Z (molecule.m^{-2} s^{-1})	τ (s)
1	6.81×10^{-5}	2.87×10^{24}	3.48×10^{-6}
10^{-3}	6.81×10^{-2}	2.87×10^{21}	3.48×10^{-3}
10^{-6}	68.1	2.87×10^{18}	3.48
10^{-10}	6.81×10^{5}	2.87×10^{14}	3.48×10^{4}

3.2.3 Ultra High Vacuum (UHV) Chamber

This section provides the details of UHV system components. In general UHV systems consists of a main chamber in which heaters and evaporators are attached, as well as manipulators, load lock, power supplies, controls, pumps and valves. In addition to these, surface analysis equipment can be attached such as low energy electron diffraction (LEED), residual gas analysis (RGA) and scanning tunnelling microscopy (STM) [92].

UHV Materials

Materials for use in the UHV systems should be carefully chosen. The main criteria which determines the optimal materials for UHV systems are low vapour pressure and withstanding bakeout [1, 90, 92]. The most common materials suitable for UHV systems are stainless steel, glass, copper, ceramics, plastics, tantalum, tungsten and molybdenum. These materials are used for different purposes and will be explained individually [90, 93].

Materials of high vapour pressure can not be used in UHV systems (e.g. zinc and cadmium). Alloys which include these two elements are also not desirable for UHV because they will evaporate at low temperatures: for example zinc evaporate around 125 °C [1, 92].

Stainless Steel

The main chamber of most UHV systems is constructed of stainless steel and the most desirable type of stainless steel is type 304 because of its strength, low gas permeably, resistance to corrosion; also it is bakeable and can be cleaned easily after fabrication [92, 93].

Glass

Glasses are used in UHV systems as windows and tubes for evaporators. Silica is used as a window in the UHV technology as it has a low thermal expansion coefficient and fracture resistivity under thermal shock; however it has a large helium permeability

which may cause problems during helium leak testing. The window edge is metalled so it can be mounted into a metal flange [93].

Copper

Oxygen free and high electrical conductivity (OFHC) coopers an excellent choice for use in UHV systems. Copper has also good corrosion resistance. Copper is customarily used as a conductor or gasket in UHV [91, 93, 94].

Ceramics

Most ceramics in UHV systems are used as thermal and electrical insulators. The most common ceramic suitable for UHV systems is alumina (Al_2O_3) [91, 93, 94].

Plastics

In general plastics have a high permeability rate and desorb a large quantity of gases so they are not compatible with UHV. However, some of plastics can be used in UHV as they can withstand high temperatures; examples are teflon (PTFE), viton and silicone. Teflon is one of the plastics which has a low outgassing rate and it is a good electrical insulator so it can be used for insulating electrical wires whereas viton and silicone can be used for sealing gaskets in UHV [91, 92].

Tantalum, Tangsten and Molybdenum

These metals can be used in UHV systems as evaporators or sample holders [92].

Omicron VT-STM

The UHV system which was used for collecting the data of this thesis is shown in the Fig.3.2. It is an Omicron variable temperature (VT-STM) system. The system consists of pumps, the main chamber and the control rack unit.

Three chambers together constitute the main body of the machine. The first one, is the entry lock (loadlock). The loadlock is used for putting samples and STM tips into the system without breaking the vacuum. There is a valve between the loadlock and other chambers which must be closed during venting the loadlock to keep the vacuum of the other chambers intact. Once the sample or the tip is put into the loadlock, the loadlock can be pumped with rotary and turbo molecular pumps to create a vacuum. Following this, the valve between the loadlock and preparation chamber can be opened to transfer the sample using the transfer arm. There is also a window to view the sample during transferring.

The second chamber of the system is the preparation chamber (PC). This chamber includes all necessary equipment to prepare the sample. First of all, there is a manipulator which takes the sample form the loadlock and then can be moved in three

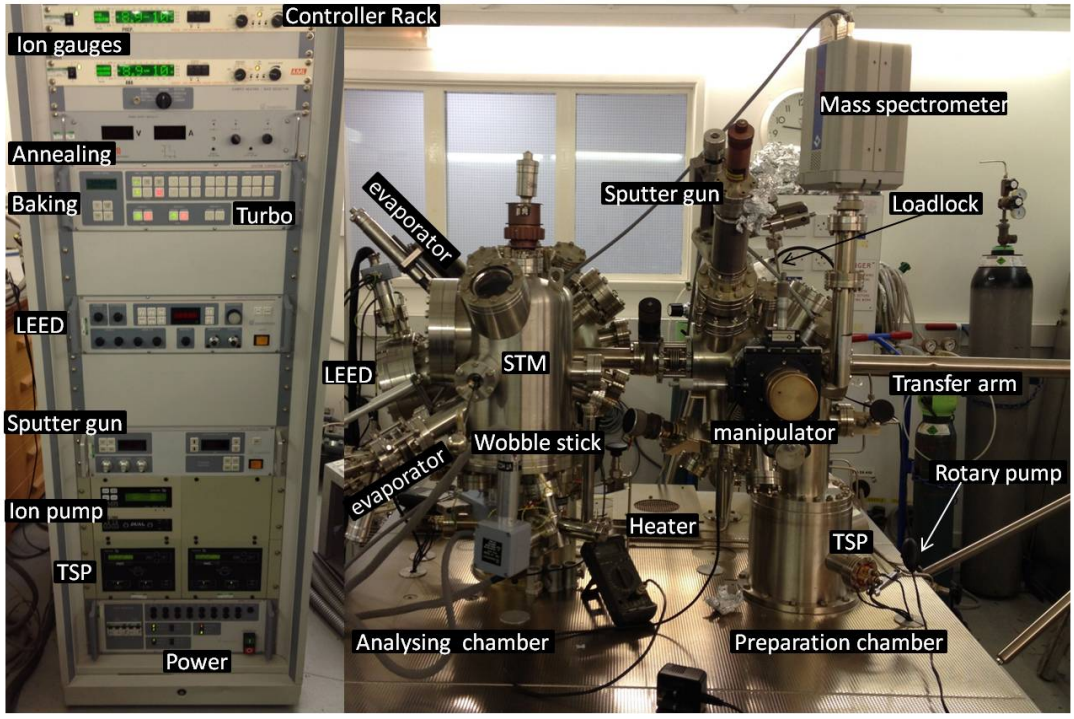

Figure 3.2: Omicron VT-STM UHV system.

dimensions. A heating facility is attached to the manipulator to anneal the sample. An ion gun is included for sputtering the sample. The purity of the vacuum can be monitored using a mass spectrometer. There is also an electron beam evaporator to deposit thin films. Finally, once the sample is well-prepared it can be transferred to the analysis chamber for characterisation. There is a transfer arm for this task.

The third chamber is the analysis chamber (AC). Equipments to characterise the surface of the sample are attached to this chamber such as low energy electron diffraction (LEED) and scanning tunnelling microscopy (STM). Similar to the PC a manipulator is attached to AC to move the sample as required. The sample can also be annealed here as an electron beam heating facility is attached to this manipulator. There are also evaporators attached for thin film deposition. To transfer the sample from the manipulator to the STM position a wobble stick is used. LEED is used to understand the symmetry of the surface and STM to characterise the structure of the surface.

UHV Pumping System

The aim of the pumping systems (pumps, valves and gauges) is to achieve and maintain UHV. Creating UHV of 10^{-10} Torr from atmospheric pressure can not be done with a single pump [91, 92]. There are several different types of pump to obtain UHV. The pumps used in our (Omicron-VT) UHV system are rotary vane pump, turbo molecular

pump, titanium sublimation pump (TSP) and ion pump. These pumps work at different pressure levels. The details of pumps, ion gauges and mass spectrometer are given in Appendix A.

Venting the system

Sometimes the UHV system needs to be opened for maintenance. Opening the UHV system means exposing it to atmosphere pressure; this is called venting. Since the pumps and gauges can not operate at the atmosphere pressure, they have to be turned off before starting venting. The system should be vented to dry liquid nitrogen rather than air.

Baking the system

Once the UHV system is vented everything is exposed to air; thus water is adsorbed to the walls of the UHV chamber. Since the water vapour pressure is so high it will be desorbed and pumped away very slowly. Therefore pumping the system at room temperature will not achieve the UHV pressure. The system must be baked out. Baking is the process of heating the whole UHV system to a temperature around 200 °C for a time between 24 - 48 hours. This is to accelerate desorption of adsorbed water. To start the baking process every electrical connection must be disconnected and every window must be covered with aluminium foil to prevent cracking due to a temperature gradient. Electrical feedthroughs also should be covered with foil. Finally the whole chamber is covered with insulated panels [1].

3.3 Sample Preparation

The samples used in the preparation of this thesis have been grown with two different methods which are Bridgeman method to grow *i*-Ag-In-Yb quasicrystals, and the self-flux method to grow both Ag-In-Gd and Ag-In-Tb 1/1 approximants [22].

3.3.1 Surface Cleaning

Ex-Situ

The grown samples can be cut to the desired size and along the desired crystallographic directions for surface studies. For example the quasicrystal was cut along the five-fold direction. Then samples were hand-polished using diamond pastes with 6μ, 1μ and 0.25μ grades respectively. After polishing samples with each grade for 20 minutes, they were put into an ultrasonic bath to remove the residual pastes. A mirror-like surface was produced using polishing. Once the polishing was done, the samples were mounted using tungsten or tantalum wires on the molybdenum sample holder. Once the sample was mounted it was put into ultrasonic bath once more.

In-Situ

Since polishing samples were kept at atmosphere pressure, it is possible that an oxide layer of thickness about 2 - 3 nm is formed on the surfaces [9]. Therefore polished surfaces are not adequate for surface science studies and surfaces have to under-go further treatment inside the UHV system to get rid of the oxide layer. There are different techniques to clean the surface inside the UHV system. The common techniques are listed below: [89, 95]

- Ion bombardment (Sputtering)
- High temperature treatment (Annealing)
- Cleavage
- Chemical treatment

The first two techniques were used to clean the surface inside the UHV system in this thesis.

Sputtering

Sputtering is the most common primary technique to clean metal surfaces. It is the process of striking energetic particles (usually Ar^+) onto the surface which dislodges the surface atoms. Thus some atomic layers of the surface will be removed. The schematic of physical sputtering is shown in the Fig.3.3. One of the drawbacks of sputtering is that it leaves a chemically and structurally damaged surface. For example a sputtered five-fold surface of *i*-Ag-In-Yb quasicrystal showed no order and different chemical composition as Ag and In atoms were depleted [96]. The samples used in this thesis were sputtered with Ar^+ (2.5 - 3 keV) for half an hour.

Annealing

Annealing is the process of heating the surface to appropriate temperature for a certain time. The chemical composition and the order of the sputtered surface can be regained by annealing the surface. The optimum annealing conditions such as annealing temperature and annealing time must be established for a specific sample because both factors affect the morphology of the surface [96]. The quasicrystal sample used was annealed at 440 °C for four hours and 1/1 approximant samples were annealed at 450 °C also for four hours.

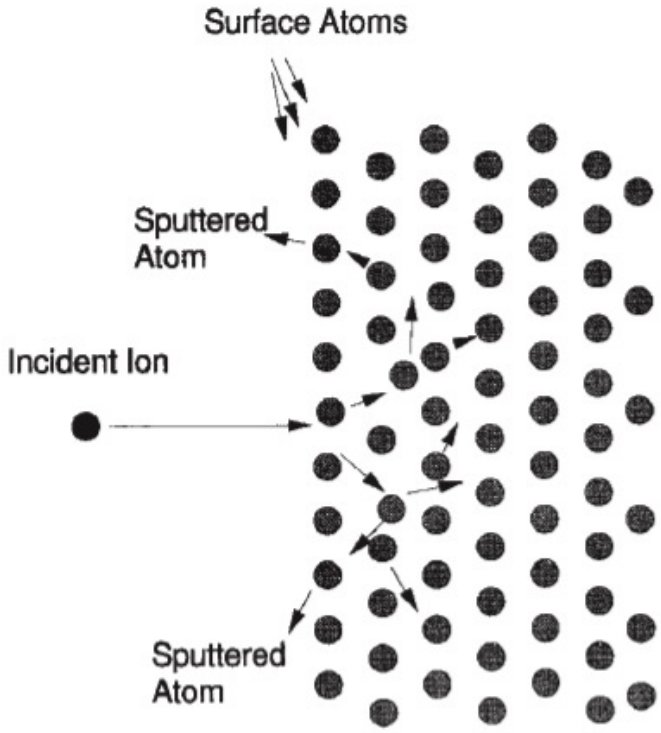

Figure 3.3: Schematic illustration of physical sputtering process. Reprinted from [97].

3.4 Surface Techniques

3.4.1 Low Energy Electron Diffraction (LEED)

Diffraction

The crystal structure can be studied using photon and electron diffraction [98]. When radiation (with wave length close to atomic spacing) strikes a crystal surface, a set of well defined diffracted beams result arranged in a characteristic geometry to form a diffraction pattern. This pattern carries information about the atomic arrangement in the crystal [99]. The incident beam is diffracted from atomic planes in the crystal. Fig.3.4 depicts Bragg's law geometry for diffraction of X-ray from crystal planes which separated by d_{hkl}.

A diffraction results from constructive or destructive wave interference. Constructive interference yields a diffraction pattern which occurs when the path difference between diffracted beams from neighbouring planes is equal to an integral multiple of the wave length (λ). This is known as Bragg's law which is given by; [100, 101]

$$2d_{hkl}\sin\theta = n\lambda \tag{3.8}$$

where d_{hkl} is the inter planar spacing, n is an integer, θ is the angle between the

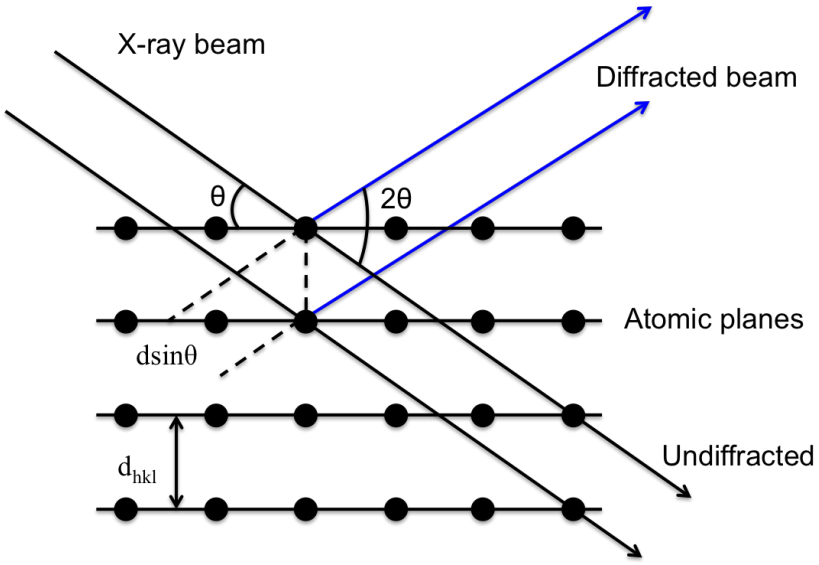

Figure 3.4: Schematic illustration of Bragg's law geometry

incident beam and crystal plane and λ is the wave length.

An attractive description for diffraction is the Laue formalism. Laue's condition of diffraction (momentum conservation law) is given by; [102]

$$\mathbf{K} - \mathbf{K}_o = \mathbf{G}_{hkl} \tag{3.9}$$

where $\mathbf{K}_o$ is the incident wave vector, $\mathbf{K}$ is the scattered wave vector and $\mathbf{G}_{hkl}$ is the reciprocal lattice vector and it is defined by; [102]

$$\mathbf{G}_{hkl} = h\mathbf{a}^* + k\mathbf{b}^* + l\mathbf{c}^* \tag{3.10}$$

where hkl are Miller indices and $\mathbf{a}^*$, $\mathbf{b}^*$ and $\mathbf{c}^*$ are primitive translation vectors in the reciprocal space. They are given by; [102]

$$\mathbf{a}^* = 2\pi\frac{\mathbf{b}\times\mathbf{c}}{\mathbf{a}\cdot(\mathbf{b}\times\mathbf{c})}, \mathbf{b}^* = 2\pi\frac{\mathbf{c}\times\mathbf{a}}{\mathbf{a}\cdot(\mathbf{b}\times\mathbf{c})}, \mathbf{c}^* = 2\pi\frac{\mathbf{a}\times\mathbf{b}}{\mathbf{a}\cdot(\mathbf{b}\times\mathbf{c})} \tag{3.11}$$

Since only elastic scattering is considered, the energy conservation law can be written as;

$$|K| = |K_o| \tag{3.12}$$

In the case of diffraction on a 2D lattice in which the periodicity in the normal direction is missing, the diffraction condition can be rearranged as follows; [92]

$$\mathbf{K}^{\|} - \mathbf{K}_o^{\|} = \mathbf{G}_{hk} \tag{3.13}$$

where $\parallel$ represents the components parallel to the surface and $\mathbf{G}_{hk}$ is defined by: [95]

$$\mathbf{G}_{hk} = h\mathbf{a}^* + k\mathbf{b}^* \tag{3.14}$$

and

$$\mathbf{a}^* = 2\pi\frac{\mathbf{b}\times\mathbf{n}}{\mathbf{A}}, \mathbf{b}^* = 2\pi\frac{\mathbf{n}\times\mathbf{a}}{\mathbf{A}}, \mathbf{A} = \mathbf{a}.\mathbf{b}\times\mathbf{n} \tag{3.15}$$

where $\mathbf{n}$ is the unit vector perpendicular to the surface [95].

Ewald Sphere

Using the Ewald sphere construction, Laue's law of diffraction can be represented graphically. One can construct the Ewald sphere as follows; first of all, build the reciprocal lattice of the crystal. Secondly draw $\mathbf{K}_o$ with origin chosen in the way that $\mathbf{K}_o$ terminates at a reciprocal lattice point. Then draw a sphere of radius ($K = 2\pi/\lambda$) such that its centre is at the origin of $\mathbf{K}_o$. Finally, find all reciprocal lattice points on the surface of the sphere, then draw the scattered wave vector $\mathbf{K}$ to these points. Fig.3.5(a) shows the construction of the Ewald sphere.

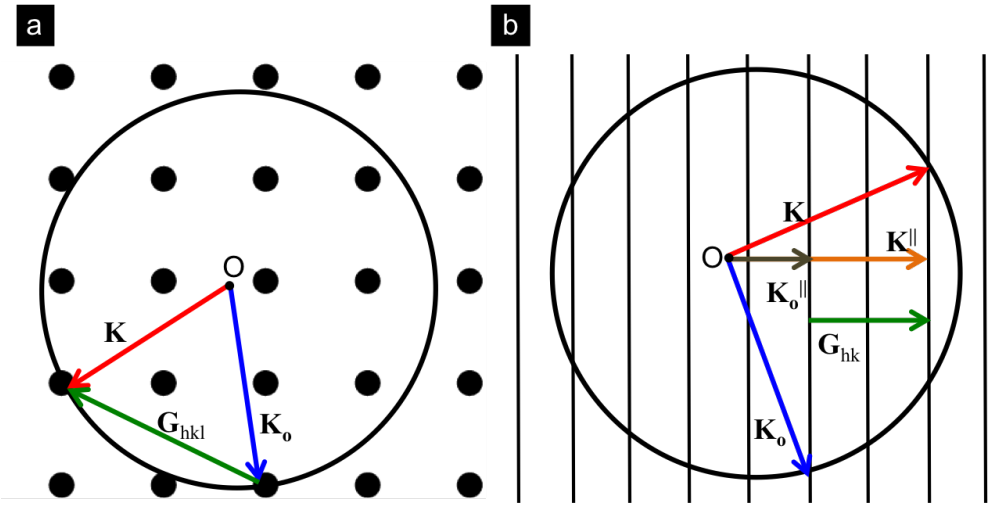

Figure 3.5: Schematic illustration Ewald sphere construction for diffraction from (a) a 3D lattice (b) a 2D lattice.

In the LEED case, the 2D reciprocal lattice points are represented by reciprocal lattice rods which are perpendicular to the surface. These rods are formed as the periodicity is infinite in the normal direction ($|c| \to \infty$ thus $|c^*| \to 0$) in a 3D lattice which makes the density of reciprocal lattice points infinite along the normal direction. In this case the scattered wave-vector of the diffracted beams can be defined as the points where reciprocal rods intersect the Ewald sphere [92]. The Ewald construction

for diffraction on a 2D surface is shown in Fig.3.5(b). Both Fig.3.5(a) and (b) satisfy equation (3.10) and (3.14), respectively.

LEED Experiment

Electron diffraction was first discovered by Davisson and Germer in 1927 [103]. Since the discovery, LEED has became a principal technique in surface science to determine the surface structure of solids. LEED can be used either *qualitatively*, in which the analysis of spot positions yields information about the symmetry and size of the unit cell, or *quantitatively*, in this case accurate information about position of atoms within the unit cell can be provided by recording the intensity of diffracted beams as a function of incident electron beam energy (I-V). LEED has been used qualitatively for data collection in this thesis.

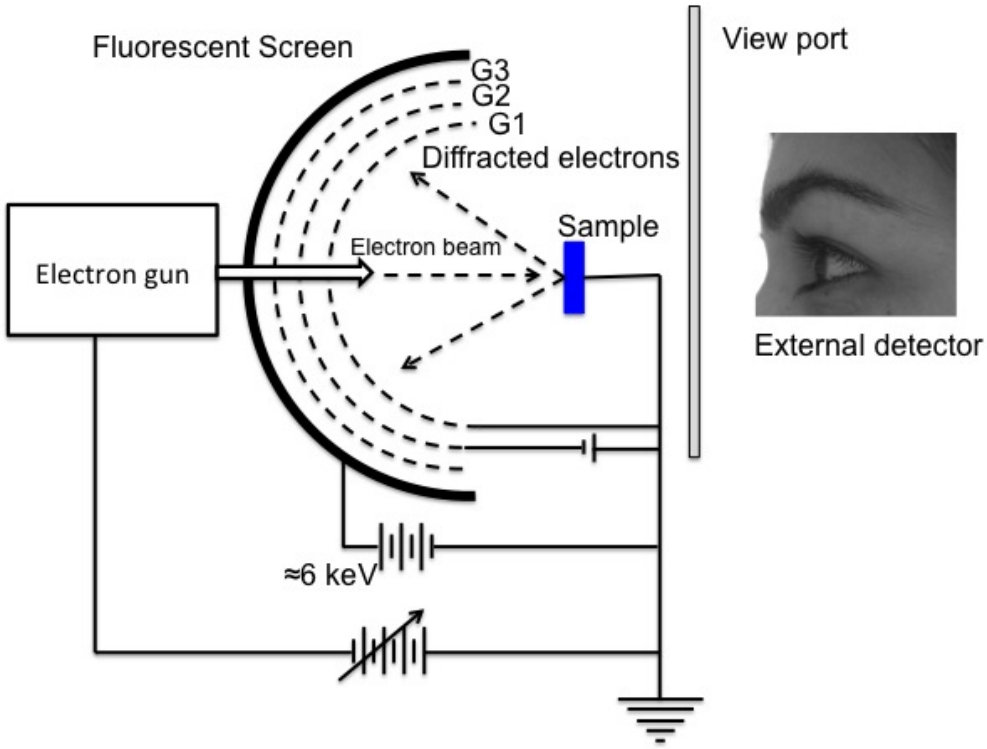

Figure 3.6: Schematic illustration of low energy electron diffraction (LEED)

A schematic illustration of a typical LEED apparatus is shown in the Fig.3.6. It consists of an electron gun to produce the incident electron beam, a sample (single crystal), a series of grids to filter the diffracted electron beams, a fluorescent screen to observe the diffraction pattern and finally an external detector to record the pattern.

The electron gun fires an electron beam with a specific energy (typically 20 - 200 eV) and wave-length. These electrons are accelerated towards the surface of the sample. Once they strike the surface they are elastically and inelastically back-scattered towards

the grids and the screen. Elastically scattered means they do not lose energy whereas inelastically scattered means they lose energy. The scattered electrons then are filtered by grids. The first grid G1 is grounded to provide the necessary field-free region. A retarding voltage is applied to G2 to suppress the inelasticity scattered electrons. Finally, the elastically scattered electrons are accelerated by G3 towards the screen. These electrons fluoresce the phosphor on the screen to produce the diffraction pattern [60].

3.4.2 Scanning Tunnelling Microscopy (STM)

STM is one of the most ubiquitous tools in the surface science laboratories. It was invented by Gert Binnig and Heinrich Röhrer at IBM, Switzerland, in 1982. The 1986 Nobel Prize for physics was awarded to them for their invention [2, 92].

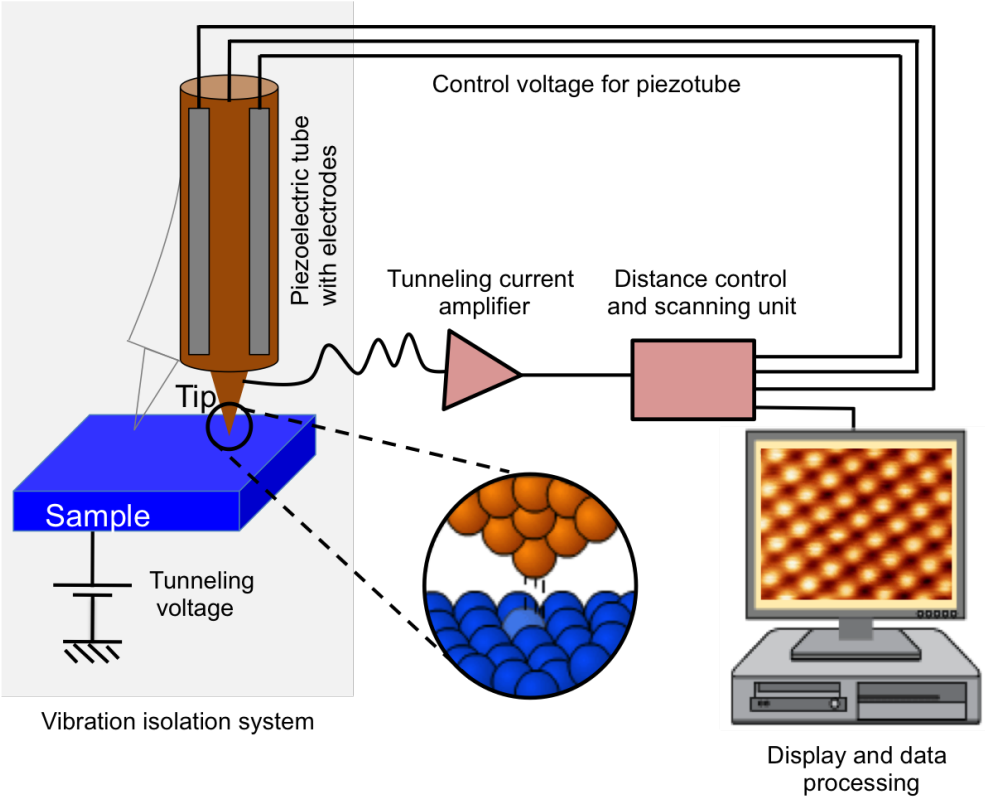

Figure 3.7: Schematic illustration of scanning tunneling microscopy (STM)

STM is used for imaging conductive surfaces at the atomic scale as well as determination of the electronic properties of the surface [104]. It has five main components which are: a very sharp conductive probe (tip) usually made out of tungsten (W) or platinum-iridium (Pt-Ir), a piezoelectric controlled scanner to raster the tip over the surface, feedback electronics to control the sample-tip separation, a vibration isolation system to reduce the noise during operation of the STM, a distance control and

scanning unit, and finally a computer system to acquire and display the data [92]. A schematic illustration of an STM is shown in Fig.3.7.

The working principle of STM is as follows. The tip is connected to the piezoelectric scanner so it can move in XYZ directions over the sample. When the tip is close enough ($\leq$ 10 Å) to the surface of the sample, the electrons will flow across the gap as a result of applying a voltage between the tip and the sample based on quantum tunneling. This yields a measurable current which can be amplified using a tunneling current amplifier and finally it can be measured. As the tip scans over the surface using the piezo controller the surface topography can be observed on the computer screen.

It is important to understand physical phenomena such as tunneling and the piezoelectric effect as they play a crucial role in the operation of STM. These phenomena are explained below.

Tunneling Effect

Tunneling effect refers to the existence of a finite probability of a particle such as an electron, which can be described by a wave function, penetrates through a potential barrier into a classically forbidden region. In consequence, the electron may tunnel through the potential barrier [105]. Fig.3.8. shows the difference between classical and quantum theory.

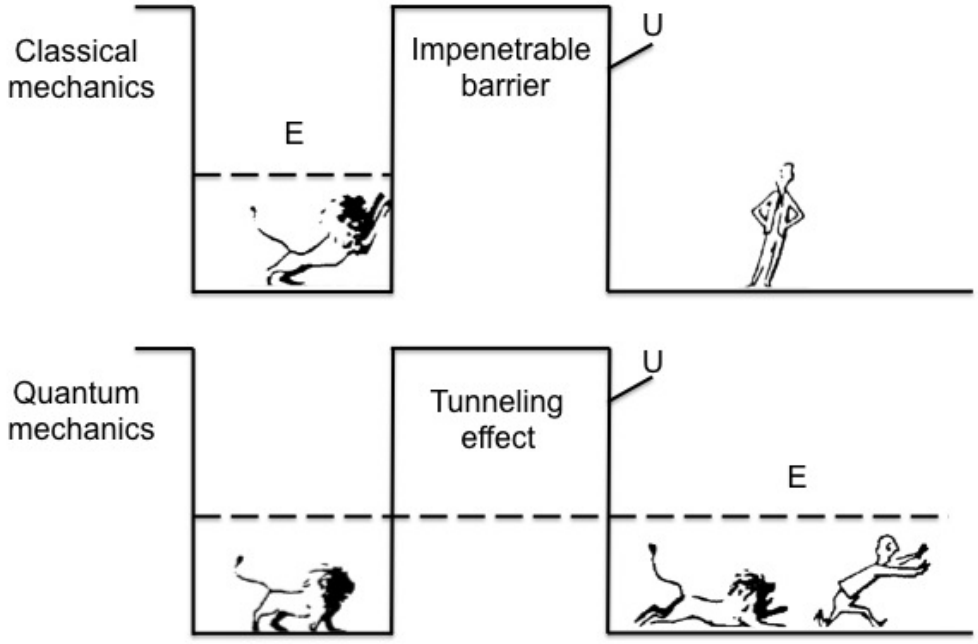

Figure 3.8: In classical mechanics the particle with kinetic energy less than the potential barrier is repelled by the barrier. In quantum mechanic electrons are described by a wave function which has a finite probability of penetrating through the potential barrier [106, 107, 108].

In classical mechanics, the total energy of an electron E is given by;

$$\frac{p_z^2}{2m} = E - U(z) \tag{3.16}$$

where $E >$ U(z) the electron has a momentum p_z whereas the electron can not penetrate to any region with $E \leq$ U(z). In quantum mechanics the electron is described by the wave function ψ(z) which satisfies the Schrödinger equation;

$$\frac{-\hbar^2}{2m}\frac{d^2}{dz^2}\psi(z) = E\psi(z) - U(z)\psi(z) \tag{3.17}$$

For a region with $E >$ U(z) the solution for equation (3.17) will be;

$$\psi(z) = \psi(0)\exp(\pm ikz) \tag{3.18}$$

where k is the wave vector and is defined by;

$$k = \frac{\sqrt{2m(E-U)}}{\hbar} \tag{3.19}$$

In these regions electrons can move freely with a constant velocity $v_z = \mathrm{p}_z/\mathrm{m}$ where $p_z = \hbar k$. However, for a classically forbidden region ($E < U(\mathrm{z})$) the solution of the Schrödinger equation will be;

$$\psi(z) = \psi(0)\exp(-kz) \tag{3.20}$$

In this case k is the decay constant which describes the electron decay state and it is defined by;

$$k = \frac{\sqrt{2m(U-E)}}{\hbar} \tag{3.21}$$

The probability density of observing electron close to the barrier is proportional to $|\psi(0)|^{\ 2}\ \exp(-2kz)$. Thus, there is a finite probability of the electron penetrating through the barrier [106, 107].

This model can help explain the tunneling phenomenon between tip (metal) - vacuum - sample (metal). The metal-vacuum-metal tunneling was first observed in 1970 by Young *et al.* Based on this tunnelling they developed a tool, so-called "topografiner" to measure the topography of the metal surfaces [105].

In the scanning tunneling microscopy (STM) case when the atomically sharp tip (tungsten W) approaches ($\leq$ 10 Å) through the vacuum to a metal surface, the sample and tip electrons wavefunctions overlap as shown in Fig.3.9. A bias voltage is applied between the tip and the sample, the electrons tunnel through the vacuum and produce a current so called tunneling current (I) which exponentially depends on the tip-sample separation (d) and the average work function of sample and tip (ϕ) [104].

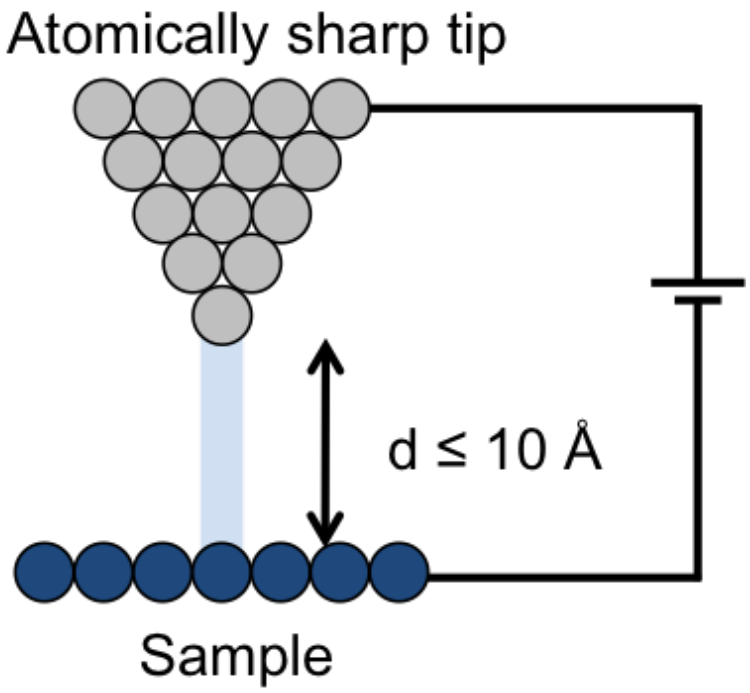

Figure 3.9: Electron tunneling between sample and tip.

$$I \propto \exp(-kd) \tag{3.22}$$

where d is tip-sample separation and k is the decay constant and is given by;

$$k = \frac{\sqrt{2m\phi}}{\hbar} \tag{3.23}$$

where ϕ is the average work function. Putting equation (3.23) into equation (3.22) yields;

$$I = C \exp(-\sqrt{\phi}d) \tag{3.24}$$

where C is constant.

Electrons can flow from the tip to the sample or from the sample to the tip depending on the applied bias voltage. If the tip is biased positively relative to the sample, electrons flow from the sample (occupied energy level) to the tip (unoccupied energy level) and the process is reversed when the tip is negatively biased. Fig.3.10 shows electron flow from sample to tip or vice versa depending on the bias voltage.

Piezoelectric Effect

Piezoelectricity was first discovered by Jacques Curie and Pierre Curie in 1880 [109]. The term itself is derived from Greek word piezein (squeeze or press). The piezoelectric

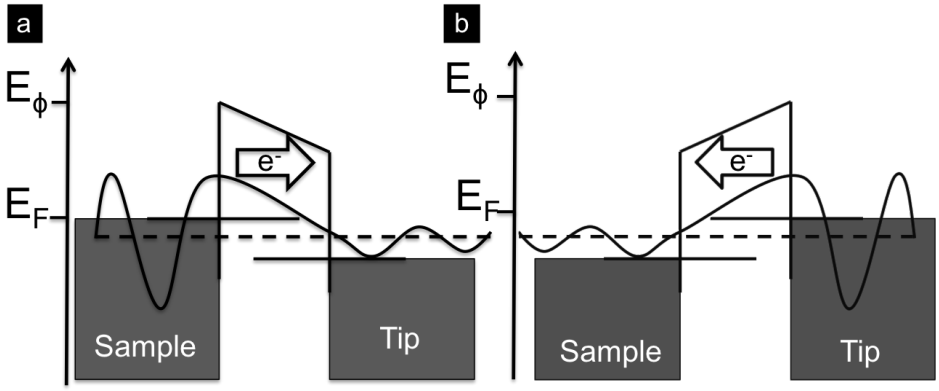

Figure 3.10: (a) electrons flow from sample to tip as the tip is positively biased. (b) electrons flow from tip to sample as the tip is negatively biased.

effect is the phenomenon in which certain materials (e.g. quartz) have the ability to generate electric charge in response to applied mechanical stress; the converse of the phenomenon is also true. This means that mechanical stress is produced when an electric field is applied. Fig.3.11 shows both direct and reverse piezoelectric effects [109, 110].

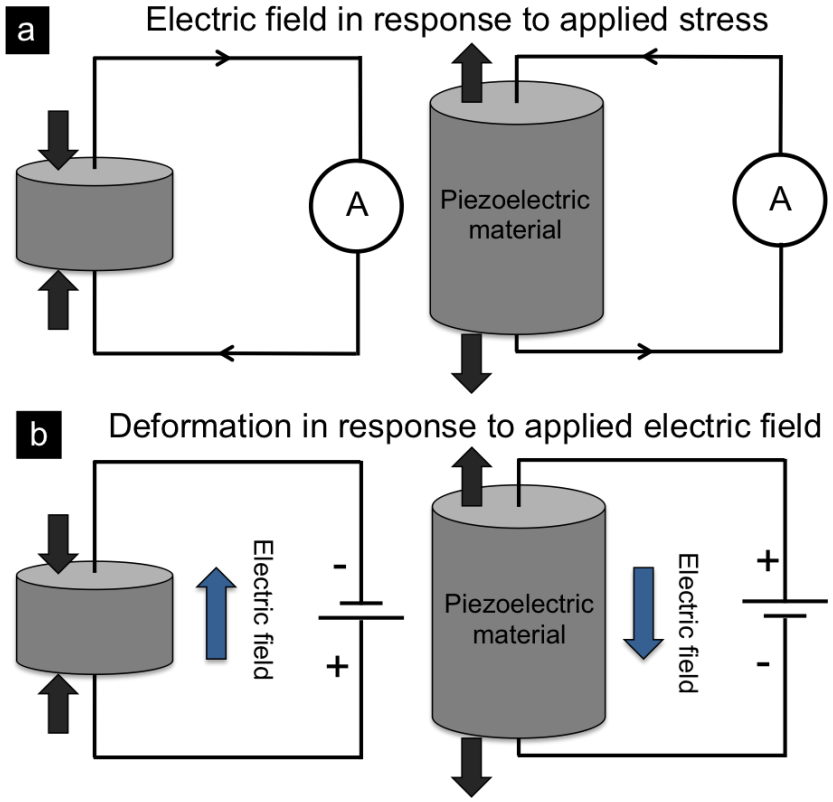

Figure 3.11: (a) Piezoelectric effect (b) Converse piezoelectric effect.

STM Operation Modes

There are two different modes of STM operation which are constant-current mode and constant-height mode. Fig.3.12 shows a schematic of STM operation modes.

Constant-Current Mode

This is the most common used mode to acquire STM images. The tip is rastered over the surface with constant current and voltage. In this mode the tip-sample separation is continuously adjusted by variation of feedback voltage using the Z-piezo driver. Thus a constant tunneling current is maintained. The merit of this mode is that it can be used for scanning rough surfaces. However, the scan speed is limited [92].

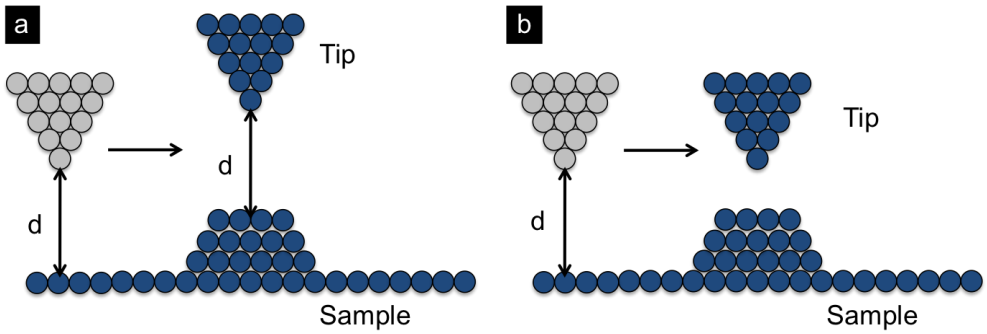

Figure 3.12: STM operation modes (a) Constant-current mode (b) Constant-height mode.

Constant-Height Mode

The tip-sample separation remains constant as the tip is scanned across the surface with constant Z-piezo voltage. In this case the surface image is represented by current as a function of lateral position. The scanning speed is much higher compared to constant-current mode, so it can be used to record STM videos. However, it can be only used to scan atomically flat surfaces otherwise there will be a high probability of crashing the tip into the sample [92].

STM Tip

As the tip plays an essential role in acquiring high resolution STM images, the tip has to be in optimum condition [111, 112]. The tip must be carefully prepared. Tips which are not sharp enough may have some atoms at the apex; in this case tunneling occurs through multiple atoms which cause multiple imaging of features at the surface. Non-cleaned tips may have an oxide layer which make the tip unstable and produce irregularities in STM imaging [113].

There are different techniques to prepare STM tips depending on the metal from which tip is made and the environment where the tip is used [114]. The typical metals to fabricate STM tips are tungsten (W), platinum - iridium (Pt-Ir) and gold (Au) [115], and the most common preparation techniques are electrochemical etching and cutting [114]. Electrochemically etched tungsten (W) tips were used to collect the data of this thesis. Méndez *et al* reported that the best electrolytic condition to prepare electrochemical etched W tips is a DC etching at (2 - 3) V with saturated NaOH solution [116].

Tip Fabrication

The equipment used to prepare tungsten (W) tips using electrochemical etching comprises; a dc power supply, sodium hydroxide (NaOH), clean tungsten wire of 0.38 nm diameter and 99.95 % purity (Goodfellow Ltd, England), a mini pliers to hold the wire and a stainless steel bar with a hole in the centre and a beaker. The steel bar is put over the beaker and the tungsten wire lowered through the hole and a few drops of the solution poured over the hole. Then the wire is connected to the positive pole of the power supply and the steel is connected to the negative pole. Fig.3.13 shows the tip fabrication process; the right image is a photograph of the setup and the left image is a schematic illustration. When a voltage (2 V) is applied, etching occurs. During etching, it has been noticed that the current decreases as the etching decreases the diameter of the wire, which increases the resistance.

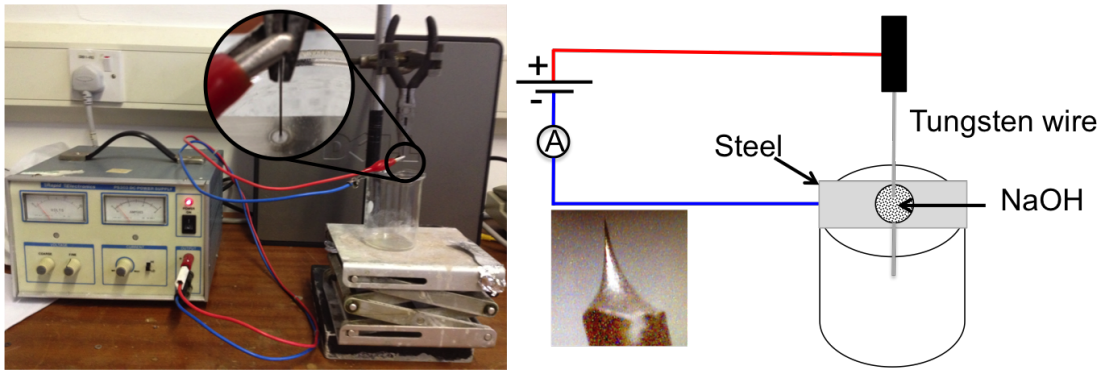

Figure 3.13: A photograph (left) and schematic diagram (right) of tip-making procedure.

During the etching process W will dissolve into soluble tungsten anions (WO_4^{2-}) on the anode while hydrogen gas bubbles and OH^- will be formed from the reduction of water on the cathode [115]. This is the etching reaction [115, 112]. The etching process takes about (20 - 30) minutes. Etching causes the wire to thin in the electrolyte; once it is thin enough the weight of the wire in the lower part fractures the neck and produces a tip [106]. A photograph of tip prepared with this procedure and used to collect the

STM data of this thesis is shown in the inset of the left image in Fig.3.13

Since the etching occurs at the air/electrolyte interface [115], the tip will be exposed to air and electrolyte, and this makes an oxide (WO_3) layer on the tip [106, 115]. This is the main drawback of W tips [113]. However, this oxide layer can be removed. The contaminated W tip cannot be used straight after preparation as the contamination affects tunneling in the STM. There are various methods to clean (remove the oxide layer) the tip. These methods are explained in detail in Ref. [106].

In our case, once the tip was made it was subjected to the following treatments. Straight after etching finished, the tip was viewed with a microscope to check its condition and then it was rinsed off with distilled water, after that it was secured in a tip holder. The tip has also sputtered inside the UHV chamber to remove the oxide layer using Ar^+ with 2.5 keV for 30 minutes.

3.5 Thin Film Deposition

Thin film formation research field is one of the most active research fields due to the existence of many applications of thin films. It is also very important technology in modern fabrication processes, e.g. for fabrication of optical data storage devices in compact disks and memory, optical coating for antireflection purposes such as interference filters on solar panels, hard surface coatings to improve mechanical properties of surfaces, and magnetic films for data storage in computers and control systems [97].

Thin film formation will also help to understand complex substrates through their interaction with the adsorbates. Quasicrystals as an example, are very complex systems in terms of structure (aperiodicity) and chemistry (more than one element). So the complexity can be reduced though achieving a single element quasicrystal. This can be done by using a quasicrystal surface as a substrate for thin film deposition.

3.5.1 The Growth Modes

Three types of epitaxial growth modes were introduced in 1958 by E. Bauer [117]. These modes are: *Frank-Van der Merwe* (Layer by layer), *Volmer-Weber* (Island grow) and *Stranski Krastanov* (Layer plus Island). In the first mode there is a high affinity between adsorbate and substrate. Thus adsorbate atoms are more strongly bonded to the substrate atoms than to each other. Therefore the film grows in a two-dimensional fashion until a monolayer is completed, thereafter further layers will form in layer by layer fashion. The second mode is opposite to the first mode, the adsorbates are strongly bonded to each other. Thus the film grows in a three-dimensional fashion producing islands. The last type is the combination of the previous modes. In this mode the film will grow smoothly to form a monolayer or more than a monolayer after which it changes to three-dimensional islands [118]. Fig.3.14 illustrates these modes.

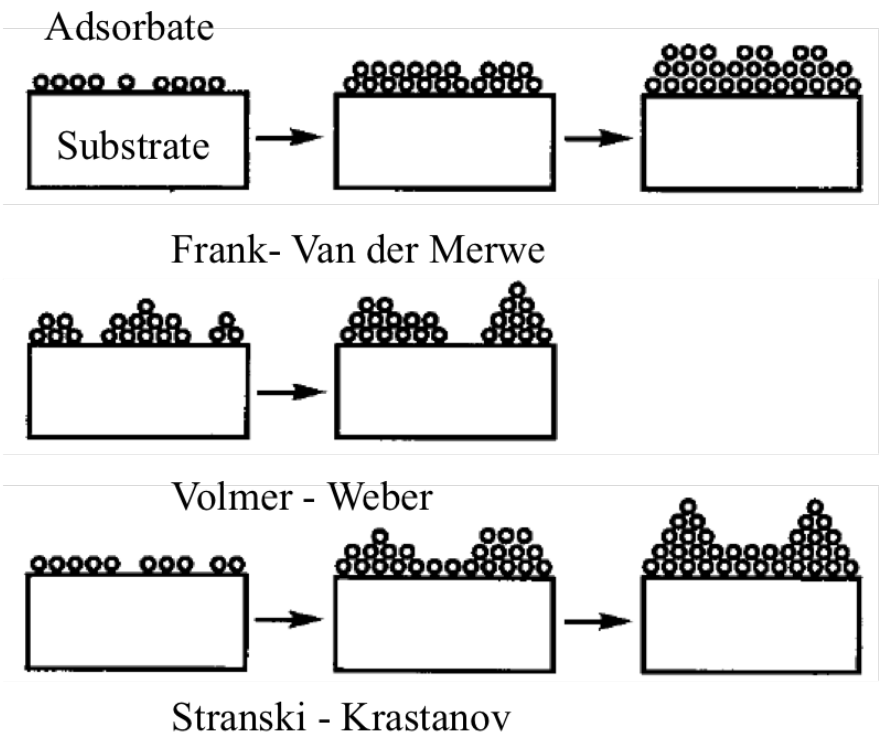

Figure 3.14: Thin film growth modes [118].

The growth modes can be distinguished in terms of surface γ_s, adsorbate γ_a, and interfacial γ^* energy. The γ^* energy is defined by equation;

$$\gamma^* = \gamma_s + \gamma_a - W_{sa} \tag{3.25}$$

where W_{sa} is the adhesion work required to isolate unit area of adsorbate and substrate surface.

When $\gamma_s \geq \gamma_a + \gamma^*$, the film will grow in *Frank-Van der Merwe* mode (layer by layer) to maximise the surface area covered by adsorbate. When $\gamma_s < \gamma_a + \gamma^*$ the surface area covered by adsorbate will be minimised so the film will grow in *Volmer-Weber* mode. In *Stranski Krastanov* mode the growth of film will change from two-dimensional fashion to three-dimensional fashion at certain film thickness. This is because the strain on the film changes the surface free energy balance from $\gamma_s \geq \gamma_a + \gamma^*$ to $\gamma_s < \gamma_a + \gamma^*$ [61].

Chapter 4

The Surface Structure of Ag-In-RE 1/1 Approximants (RE = Tb, Gd and Yb)

4.1 Introduction

Before presenting the results obtained from the surface structure of approximants, the surface structure of the parent icosahedral quasicrystal will be presented. This is because they have the same building block; the RTH cluster. The RTH clusters in approximants are packed in a periodic fashion.

4.1.1 Structure of the Five-fold Surface of the *i*-Ag-In-Yb Quasicrystal

The lack of other quasicrystal samples suitable to prepare under UHV conditions for surface experiments limited the surface studies to Al-based quasicrystals. The surface structure of Al-based quasicrystals was found to be bulk-terminated without any reconstruction. However surface relaxation was observed on the surface of ten-fold decagonal quasicrystals [10]. After discovery of the *i*-Ag-In-Yb quasicrystal, all surfaces including five-fold [16], three-fold [119] and two-fold [120] surfaces of the *i*-Ag-In-Yb quasicrystal were studied. All surfaces were found to be formed at the bulk planes which intersect the centre of the RTH clusters [121]. The RTH clusters make up the bulk structure of these quasicrystals. This section provides the details of previous studies on the structure of the five-fold surface, as it has been used for the work in Chapters five and six.

The fivefold surface of the *i*-Ag-In-Yb quasicrystal was first studied under UHV using X-ray photoelectron spectroscopy (XPS), reflection high-energy electron diffraction (RHEED) and STM [96]. It was found that after sputtering with Ar^+ (2.5 – 3 keV) the surface showed no order and a change in chemical composition, see Fig.4.1(a) and (b). In contrast to Al-based quasicrystals which show a depletion of the lighter element Al

upon sputtering [68, 7], the *i*-Ag-In-Yb quasicrystal showed the depletion of heavier elements Yb and In. Annealing the surface around 400°C restored the bulk stoichiometry and the quasicrystalline structure was regained. STM images of the sputtered-annealed surface showed the step/terrace morphology [96].

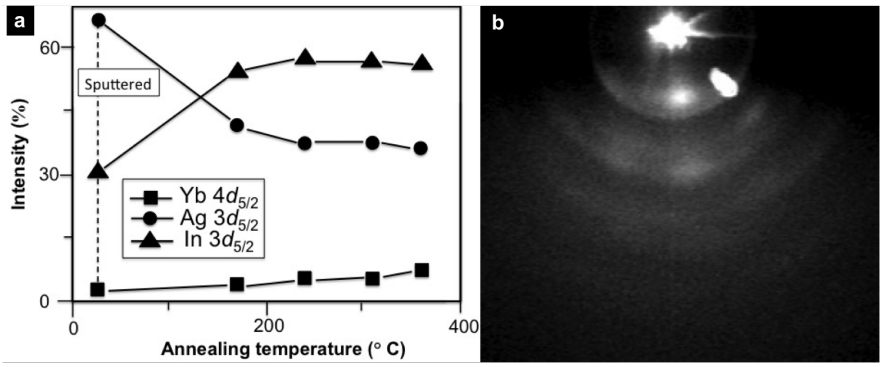

Figure 4.1: (a) The intensity of Ag $3d_5/2$, In $3d_5/2$ and Yb $4_d5/2$ core level photoemission from the fivefold *i*-Ag-In-Yb surface after sputtering (marked by dotted line) and annealing at different temperatures. (b) RHEED pattern from the fivefold *i*-Ag-In-Yb surface after sputtering. (a) and (b) reprinted from [96].

Following this, the study of the structure of the fivefold surface of the *i*-Ag-In-Yb quasicrystal was reported by Sharma *et al.* using STM and LEED [16]. The STM images revealed terraces which were separated with steps of different heights. The observed step heights in STM were found to be short (S = 0.28 ± 0.04 nm) and large (L = 0.85 ± 0.05 nm). These steps often produce a sequence LSLSS as shown in Fig.4.2(a). Fig.4.2(a) is a 250 nm × 250 nm STM image, showing the step/terrace morphology of the five-fold surface of the *i*-Ag-In-Yb quasicrystal. Fig.4.2(b) shows the LEED pattern of the surface taken at (23 eV) electron energy after annealing the surface which shows quasicrystalline order [16].

High resolution STM images of terraces were found to be applied bias-voltage dependant. Fig.4.2(c) and (d) are STM images taken at negative and positive bias respectively of the same terrace and taken with the same tip. STM images taken at negative bias reveal protrusions arranged in pentagons of 2.40 ± 0.15 nm edge length. These pentagons are rotated by $\pi/5$ with respect to each other and are marked with yellow circles in Fig.4.2(c). The diameter of the protrusions were found to be 1.30 ± 0.04 nm which is obtained from the full width at half maxima of the height profiles [16].

The STM images taken at positive bias revealed rings in the positions of protrusions i.e., at the vertices of the pentagons. The yellow circle in Fig.4.2(c) highlights a pentagon with rings at the vertices. The diameter of these rings were found to be 1.80 ± 0.05 nm [16].

After observation of the step/terrace structure and high resolution STM images of

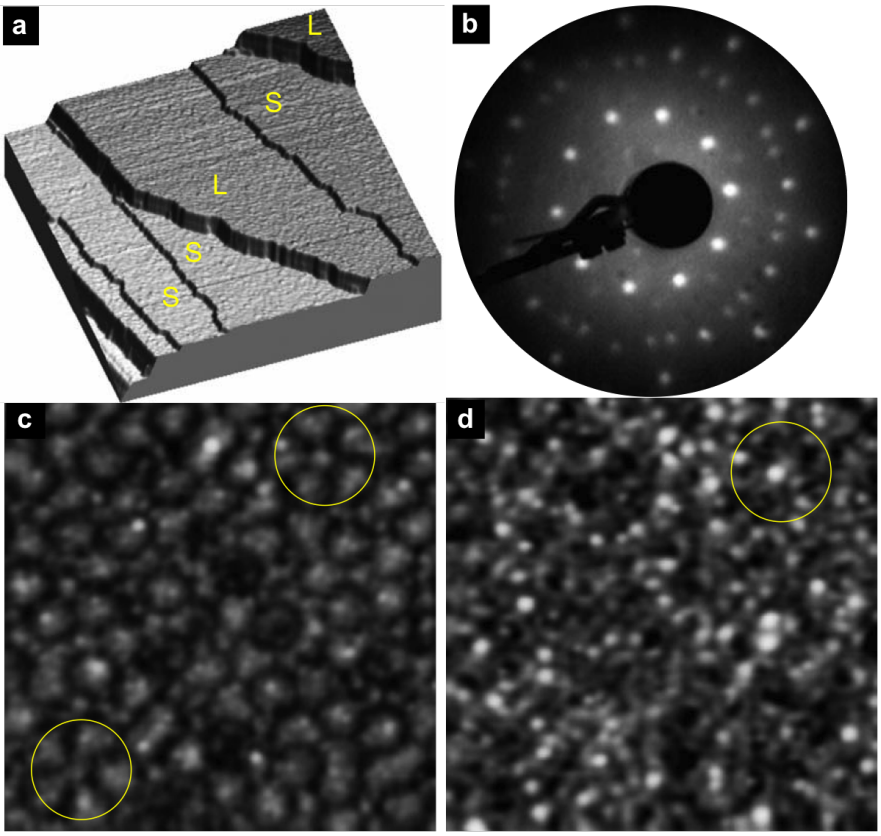

Figure 4.2: (a) A 250 nm × 250 nm STM image of the fivefold *i*-Ag-In-Yb surface, showing the step/terrace morphology. (b) LEED pattern from the same surface at (23 eV), showing quasicrystalline order. (c) 23 nm × 23 nm STM image taken at (-0.5) negative bias, showing protrusions arranged in pentagons of 2.40 ± 0.04 nm edge length. (d) 23 nm × 23 nm STM image taken at (+1) positive bias, showing rings arranged in pentagons of 2.40 ± 0.04 nm edge length. (a), (b), (c) and (d) are reprinted from [16].

terraces, the STM data were compared with the bulk structure model of the *i*-Cd-Yb quasicrystal. Fig.4.3(e) is the atomic density distribution of the *i*-Cd-Yb, and shows the bulk planes of different atomic density. It was found that the observed step heights in STM are consistent with the bulk separation of planes which intersect the centre of the RTH cluster. These planes are marked with blue rectangles and they can also produce the same sequence LSLSS observed in the STM.

Moreover, the bias dependent STM images were compared with the atomic structure of those planes which intersect the RTH cluster centre. Fig.4.3(a) is the in-plane structure (20 nm × 20 nm) of the plane which cuts the centre of RTH cluster (marked with the black arrow) and the thickness of the slab (ΔZ) is 0.02 nm. The structure shows pentagons of two different orientations of 2.53 nm edge length. These pentagons are formed by light pink and green rings which belong to Cd and Yb atoms of the fourth (icosadodecahedron) and third (icosahedron) shell of the RTH cluster respec-

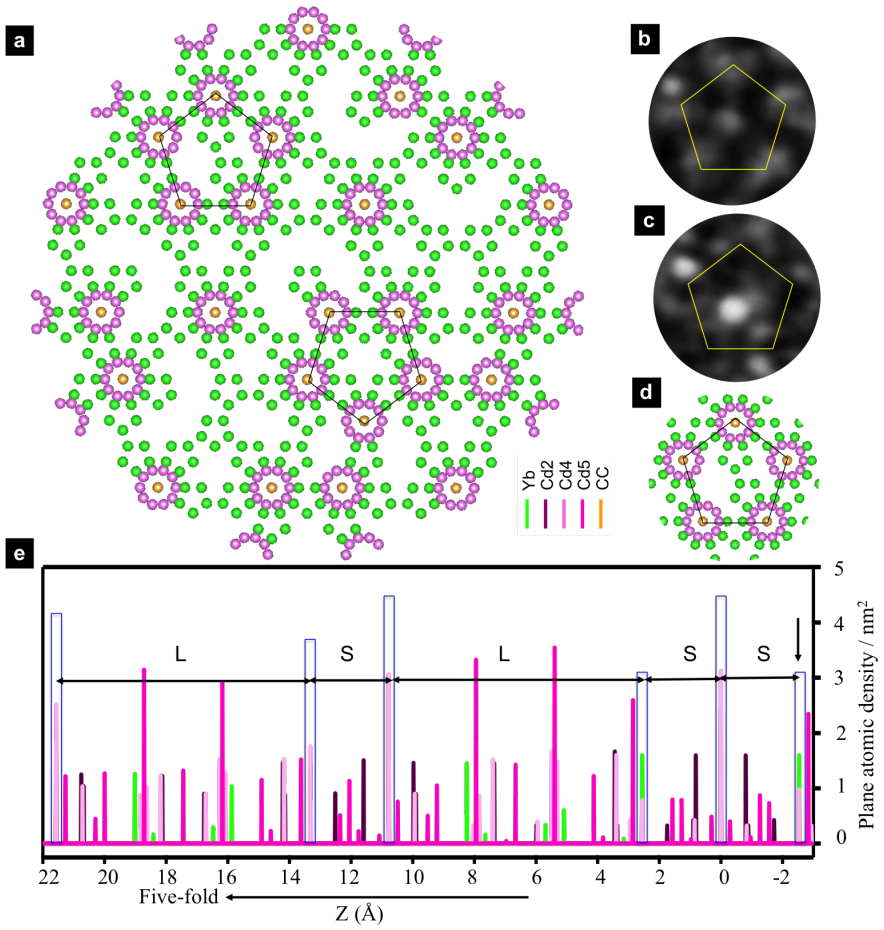

Figure 4.3: (a) The in-plane structure of a bulk plane (marked by the black arrow) which intersects the centre of the RTH cluster. (b), (c) and (d) Pentagon motifs of STM images at negative and positive bias, and in-plane structure respectively. (b) and (c) are reprinted from [16]. (e) The atomic density distribution of the *i*-Cd-Yb quasicrystal along five-fold, showing atomic bulk planes of different density. Different colours refer to atoms of different shells of the RTH cluster.

tively. Here the Cd atoms are replaced by Ag/In. The diameter of Ag/In rings in the model is 1.30 nm which is consistent with the diameter of protrusions (1.30 ± 0.04 nm) observed in the STM at negative bias. The diameter of the Yb ring is 1.94 nm in the model which is also close to the diameter of rings 1.80 ± 0.05 nm observed in STM at positive bias. That means at negative bias the tunneling current is enhanced at the Ag/In sites while at positive bias it is enhanced at the Yb sites [16]. This agrees with the results of an *ab initio* study of the *i*-Cd-Yb quasicrystal which reported that the Yb-5d dominates the unoccupied states just above the Fermi level [122]. Fig.4.3(b), (c) and (d) are pentagonal motifs of STM image at negative and positive bias, and in-plane structure respectively. To summarise, the five-fold surface of *i*-Ag-In-Yb quasicrystal is preferentially formed at bulk planes which are dense and cut the centre of the RTH

clusters [16].

4.2 The Surface Structure of Ag-In-RE 1/1 Approximants

As these approximants have the same building blocks (RTH clusters), the study of their surface structure will be interesting to compare with their parent quasicrystal surfaces in terms of the bulk termination. In this work, a structural study of the Ag-In-RE 1/1 approximant surfaces (RE = Tb, Gd and Yb) is presented. Scanning tunneling microscopy (STM) and low energy electron diffraction (LEED) were employed to characterise the surfaces. Understanding the clean surface of approximants to prepare them for use as templates to grow new metallic and molecular thin films is another motivation of the work. This will help in understanding the factors affecting epitaxy on these approximants and provide a useful comparison to growth on the *i*-Ag-In-Yb quasicrystal surface.

4.2.1 Experimental Procedures

The $Ag_{46.5}In_{39.2}Tb_{14.3}$, $Ag_{47}In_{38.3}Gd_{14.7}$ [22] and $Ag_{40}In_{46}Yb_{14}$ [81, 26] 1/1 approximant samples were used for this study. All samples were grown with the self-flux method, starting with 99.999 % pure Ag, 99.9999 % pure In, 99.9 % of pure Tb, Gd and Yb. The raw metals were put into an Al_2O_3 crucible and it was sealed into a quartz tube with an Ar atmosphere. Then the sealed samples were placed in an electronic furnace. First the materials were melted and well mixed at 900 °C for 3 hours, then cooled down to 760 °C for 4 hours (- 10K/min). At this temperature, the system was slow cooled (-1 K/hour) to 610 °C in order to grow single crystals. At 610 °C, the system has two thermal equilibrium phases: the approximant phase (solid phase) and the liquid phase. Therefore, at this temperature (610 °C, decanting temperature), an ampoule was taken from the furnace and then set into a centrifuge to decant the liquid phase. After cooling the ampule to room temperature, it was opened and the single grains were harvested [22, 26].

To prepare samples for surface study, usually samples are cut along desired crystallographic direction but this was not done for Ag-In-Tb and Ag-In-Gd 1/1 approximants because of the tiny size of the samples. Samples were hand-polished along the (100) facet with diamond paste of 6 μm, 1 μm, and 0.25 μm grades successively. After polishing with each grade for 20 minutes, samples were put into ultrasonic bath to remove the residual paste. Following this, samples were cleaned in-situ using normal sputter/annealing cycles. The surface was sputtered by clean Ar^+ with (2.5 - 3 keV) for 30 minutes, followed by annealing at 450 °C for four hours. An infra-red pyrometer with the same emissivity of their related quasicrystals [96] (0.35) was used to monitor the temperature.

Scanning tunneling microscopy (STM) images and low energy electron diffraction (LEED) patterns were recorded at room temperature using an Omicron variable temperature (VT-STM) instrument. STM images were analysed using WSxM software [123]. VESTA software was used to analyse the model structure [124] and producing the surface structure model for different facets.

4.2.2 STM and LEED Results

Bulk Structure of Ag-In-RE 1/1 Approximants

Before we present the experimental results, we describe the bulk structure of the Ag-In-RE 1/1 approximant. The Ag-In-RE 1/1 approximant is isostructural to the Cd-RE 1/1 approximant, where Cd atoms are replaced by Ag and In. The structure can be described as a body centred cubic packing of rhombic triacontahedral (RTH) clusters. The RTH cluster consists of five successive atomic shells. The inner shell is a tetrahedron with 4 Cd atoms. The second shell is a dodecahedron which has 20 Cd atoms, the third shell is an icosahedron with 12 Yb atoms, and the fourth shell is an icosidodecahedron with 30 Cd atoms. Finally, the outer-most shell is a rhombic triacontahedron with 92 Cd atoms. Fig.4.4(a) shows RTH atomic shells (innermost shell is not shown). The RTH cluster have five-fold, three-fold and two-fold axes, these axes are highlighted ($5f$, $3f$ and $2f$) in each shell.

As mentioned above; Cd atoms are replaced by Ag and In in the Ag-In-Yb approximant. However, chemical ordering of Ag and In has not yet been determined. It is known that the first shell of the RTH cluster is formed by In atoms. Similarly, the second shell contains 60 % Ag and 40 % In and the fourth shell 20 % Ag and 80 % In. The mid-edge of the fifth shell is 100 % Ag and vertices contain 37 % Ag and 63 % In. We will use this information to determine the composition of the surface layer in Section 4.2.4.

The diameter of the outermost shell (measured along two-fold [100] axis) is the same as the lattice constant so that the outermost shell shares atoms with the same shell of the neighbouring cluster. A bcc unit cell is shown in Fig.4.4, for clarity only icosahedra are shown. Different colours are chosen for atoms of different shells.

The lattice constant a of the three approximants (Cd-RE) is slightly different (Ag-In-Gd: 1.529 nm , Ag-In-Tb: 1.519 nm [22] and Ag-In-Yb 1.537 nm [15]). The size of the shells of the RTH cluster in the three approximants will be also different in the same proportion. We have used the model structure of the Cd-Tb 1/1 approximant with lattice constant 1.557 nm throughout the chapter. The difference in the lattice constant in the three systems is within the uncertainty of the STM measurements.

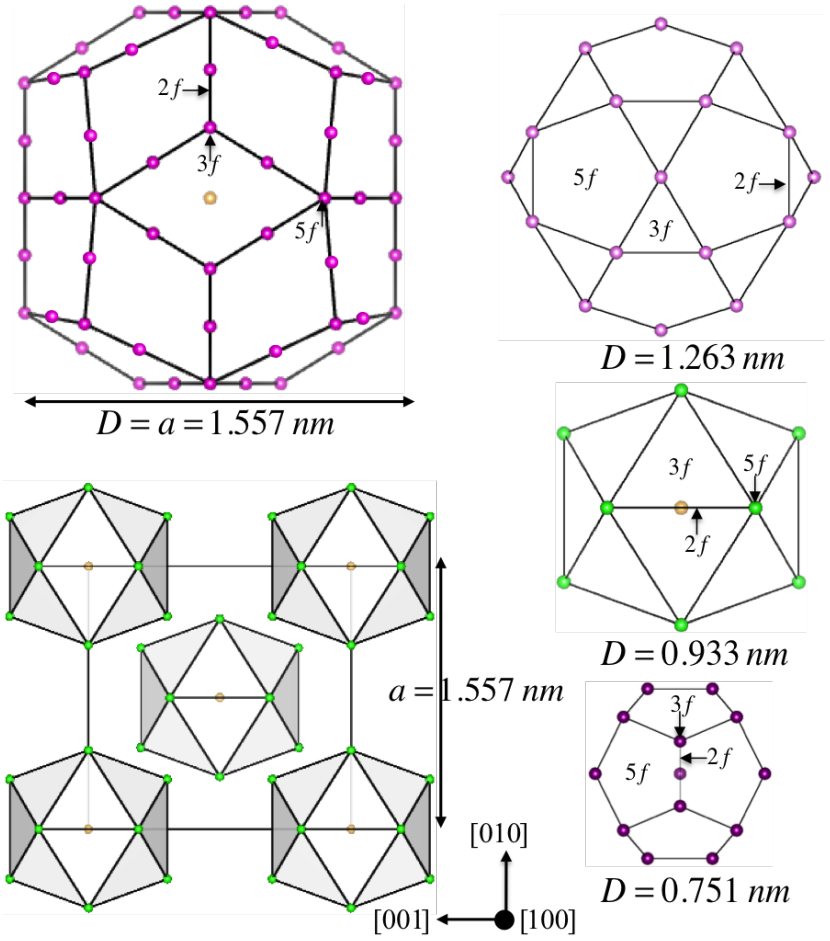

Figure 4.4: Structure of the Cd-RE 1/1 approximant. Successive atomic shells of rhombic triacontahedron (RTH) cluster are depicted with their diameter measured along the two-fold axis and a bcc unit cell is shown (with only icosahedra for clarity).

Observation of Facets

The surface of both Ag-In-Gd and Ag-In-Tb samples after sputtering and annealing produces facets along different crystallographic directions. Fig.4.5 (a) and (b) are 400 nm × 400 nm and 200 nm × 200 nm STM images of the Ag-In-Tb surface and Fig.4.5(c) is a 200 nm × 200 nm STM image of the Ag-In-Gd surface, showing facets along different crystallographic directions.

To find the Miller indices (*hkl*) of the facet planes, we first identified the (100) facet from its symmetry. Then, the angle between the (100) facet and the other facet was determined using STM images. The calculated angles are compared with the expected values in Table 4.1. The angle alone is not sufficient to specify the Miller indices of the facets. For example, the (310), ($3\bar{1}0$), (301) and ($30\bar{1}$) plane make the same angle 18.43° with the (100) plane. The Miller indices were thus determined by the cross product of two vectors in the facet plane. Three points were chosen on a plane which

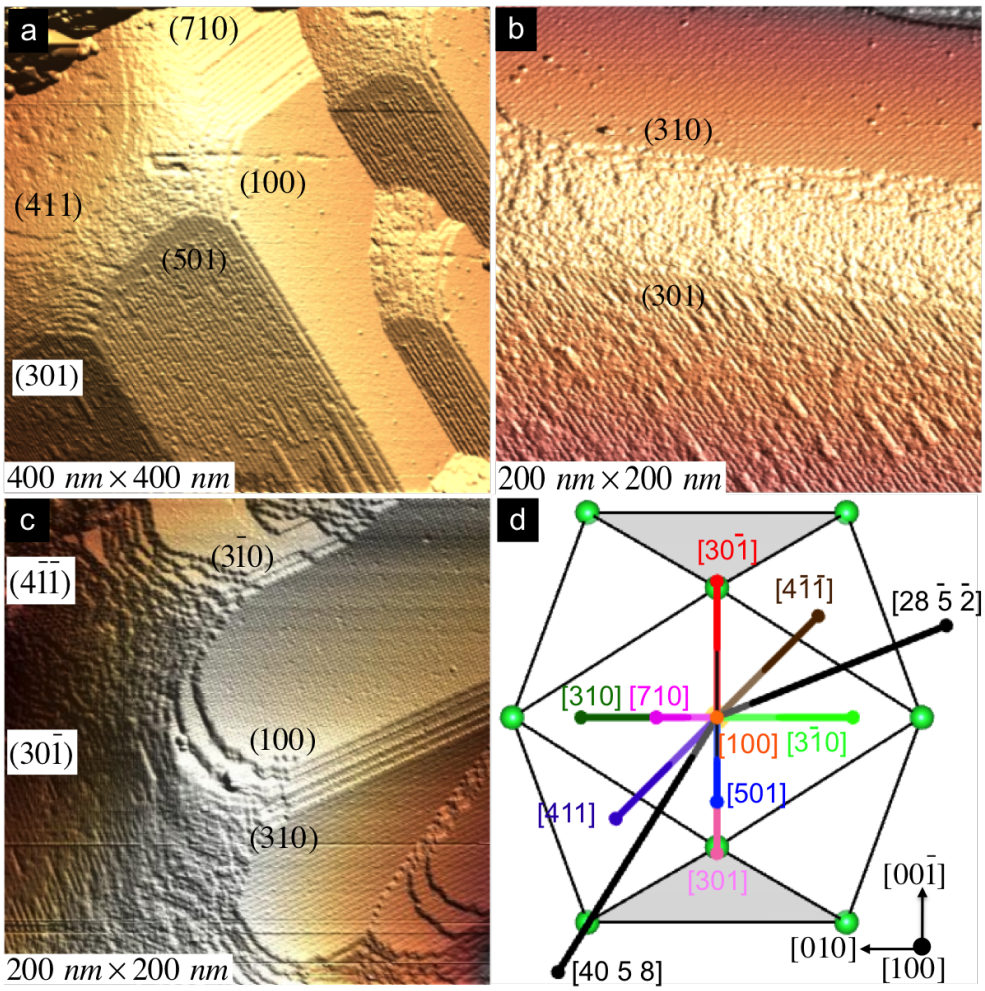

Figure 4.5: STM images of facets: (a) 400 nm × 400 nm STM image of the Ag-In-Tb surface. (b) 200 nm × 200 nm STM image of the Ag-In-Tb surface. (c) 200 nm × 200 nm STM image of the Ag-In-Gd surface. (d) Icosahedron shell of the RTH cluster indicating different crystallographic directions.

Table 4.1: The observed facets and their angle of inclination with the (100) surface.

	(411)	(4$\bar{1}\bar{1}$)	(501)	(301)	(30$\bar{1}$)	(310)	(3$\bar{1}$0)	(710)
actual angle	19.47°	19.47	11.31°	18.43°	18.43	18.43°	18.43°	8.13°
measured angle	20.35°	20.11	12.05°	18.25°	18.60	19.05°	18.01°	9.2°
Ag-In-Tb	Yes	No	Yes	Yes	No	Yes	No	Yes
Ag-In-Gd	No	Yes	No	No	Yes	Yes	Yes	No

give two vectors. The cross product of these vectors give the normal unit vector of the plane which is the equivalent to the Miller indices of the plane for cubic system.

The Miller indices of the planes in the STM images are found to be (411), (501), (710) and (301) in Fig.4.5(a), (310) and (301) in Fig.4.5(b) and (30$\bar{1}$), (310), (3$\bar{1}$0) and

$(4\bar{1}\bar{1})$ in Fig.4.5(c). The (100) and (310) facets are observed in both samples, while other facets are seen only in one or another sample (refer to Table 4.1). The most frequently observed facets are (100) and (310). Other facets are occasionally observed. The distribution of the facets over the sample is not homogenous. Some facets are observed more dominantly in one area than another.

We now analyse whether the facets are aligned along particular high symmetry directions of the RTH cluster. The RTH cluster has five-fold, three-fold and two-fold axes as mentioned earlier. For clarity, we have shown only the icosahedral shell of the RTH cluster in the Fig.4.5(d). The surface normal direction of each of facets observed in STM is also shown in the figure. The two-fold axis of the cluster is aligned along the [100] direction of the crystal lattice, whereas [310] is along the three-fold axis of the cluster. However, the other facet planes are not aligned any particular high symmetry direction of the cluster.

The formation of the facets is further confirmed by comparing STM images with the bulk structure. Fig.4.6 shows the lattice planes of the bcc crystal along (100), (310) $(3\bar{1}0)$, (301), $(30\bar{1})$, (501), (710), (411) and $(4\bar{1}\bar{1})$. Here, only the space lattice is considered not the RTH cluster. Fast Fourier transform (FFT) of STM images from each facet, shown in the same figure, confirms that the symmetry and dimension of the unit cell observed by STM is in agreement with that of the facet planes expected from the bcc structure with lattice constant a.

The observation of the facets is in contrast with the result from the (100) surface of the isostructural Ag-In-Yb 1/1 approximant [29]. The latter system showed only the flat surface with no facets. The structure of (100) surface of Ag-In-Yb 1/1 approximant will be discussed in detail later on. In order to understand the formation of the facets in the current systems, we checked the macroscopic orientation of the surface by Laue back-scattering after the UHV measurements were performed. It was found that the Ag-In-Gd surface was tilted by 10° from [001] and 4° from [010]. The respective angles for the Ag-In-Tb were found to be 11° from [001] and 7° from [010]. This corresponds to the overall tilt of the surface from the (100) plane to be 10.8° and 13.1 ° for Ag-In-Gd and Ag-In-Tb respectively. So the surface orientation found from the tilt are close to {20 5 2}- and {40 5 8}-equivalent direction for the Ag-In-Gd and Ag-In-Tb sample, respectively. Among many equivalent directions, $[20\ \bar{5}\ \bar{2}]$ and [40 5 8] would explain why the facets are observed predominantly in a particular direction of the crystal. As can be seen in Fig.4.5 or Table 4.1 the facets in Ag-In-Gd are observed more towards $[0\bar{1}\bar{1}]$ direction than [011] and vise-versa in Ag-In-Tb. We assume that the tilt was introduced during polishing the surface; a mis-alignment of the surface may have promoted the formation of the facets. We also examined whether a different surface preparation method would influence the surface morphology. For this preparation samples were removed form the UHV chamber and repolished as described in Section 4.2.1 and

sputtered at high temperature (450 °C) for several hours. The surface was then cooled down to room temperature and sputtered briefly (15 minutes with the same parameters) and annealed at (450 °C) for 60 minutes. The overall facet morphology remained unchanged after this preparation.

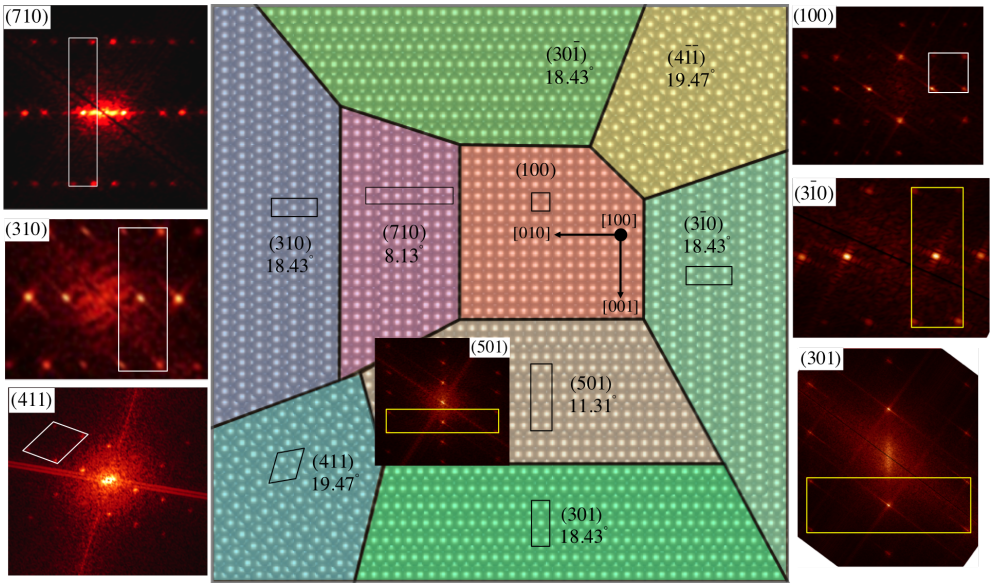

Figure 4.6: Symmetry of the facets: A bcc lattice showing truncated planes along the direction of the facets observed by STM in bird eye view along [100] (middle) and FFT of STM images from each facet. The surface unit cells of the facets are marked. The size of the FFT is not to scale.

The orientation of the facets is further confirmed by comparing STM images with the bulk structure. High resolution STM images of each facet were taken separately. Atomic resolution was only achieved on the (301) and (501) facets. Features observed on the other facets can also be compared with the structure expected from the crystal structure of the Ag-In-RE 1/1 approximant, which is based on the body-centred-cubic (bcc) lattice. The detailed structure of each facet is described in the next section. The LEED patterns which confirm the existence of facets on the surface will be discussed later on.

Detailed Structure of the Facets

(100)

STM images from the (100) facet of both Ag-In-Tb and Ag-In-Gd 1/1 approximants are very similar. Fig. 4.7(a) shows a 60 nm × 60 nm STM image of AgIn-Gd surface exhibiting a step/terrace morphology. The line profile in Fig. 4.7(b) shows that the flat terraces in Fig.4.7(a) are separated by steps of 0.770 ± 0.004 nm height. A 120 nm × 120 nm STM image is shown in Fig.4.7(c), showing the step/terrace morphology

of the Ag-In-Tb surface. Observed steps of Ag-In-Tb system have very similar heights (0.780 ± 0.020 nm) to Ag-In-Gd systems.

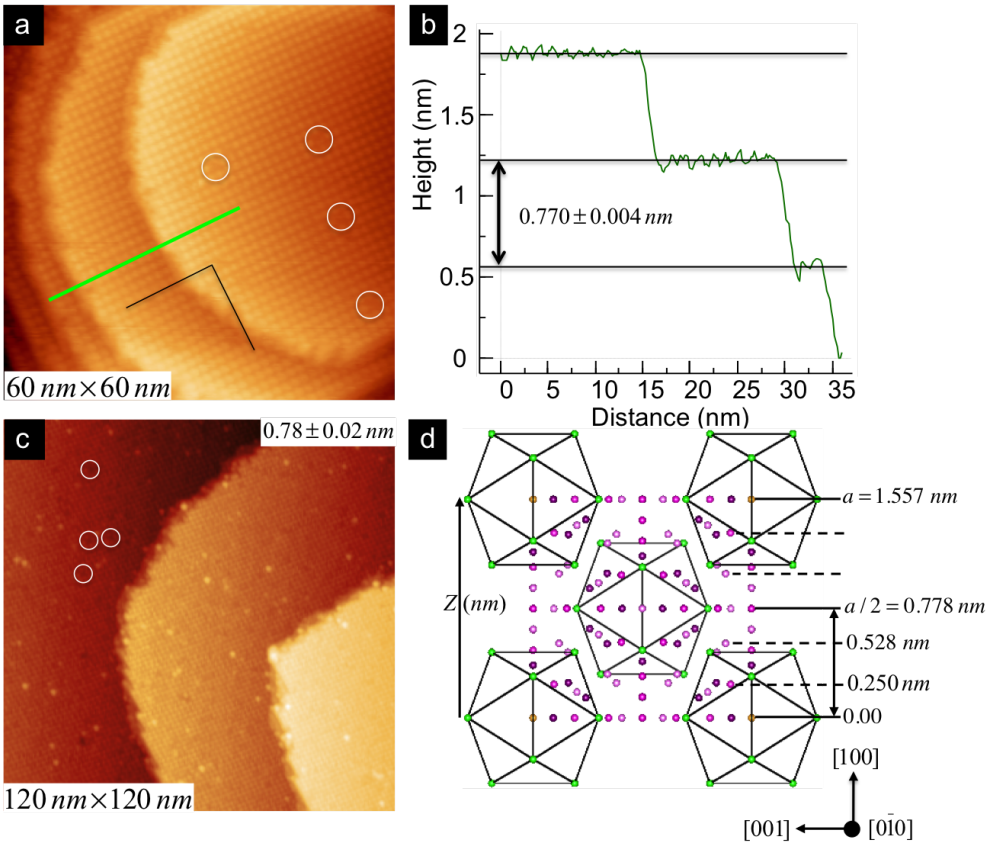

Figure 4.7: (a) 60 nm × 60 nm STM image of the Ag-In-Gd (100) surface showing a step/terrace morphology ; (b) A line profile across the terraces of image(a); (c) 120 nm × 120 nm STM image of Ag-In-Tb (100) facet showing flat terraces separated by steps of 0.780 ± 0.020 nm height. (d) A unit cell of the Cd-Tb 1/1 approximant with 1.557 nm lattice constant projected normal to [100], showing flat (black solid line) and puckered (dashed lines) layers. For clarity only the icosahedron shell is shown. White circles in (a) and (c) highlight point defects.

In order to explain the step height, the bulk unit cell of the Cd-Tb 1/1 approximant is presented in Fig.4.7(d). Two different type of layers, flat (black solid line) and puckered (dashed lines) can be identified perpendicular to the [100] direction. The flat layers are located at Z = *0*, Z = a/2 and Z = a, where they intersect the centre of the RTH clusters. The puckered layers are at 0.250 nm and 0.528 nm. Other layers at z > a/2 are mirror planes of the layers at z < a/2. The height separation of flat layers is 0.778 nm, which is close to the observed step heights in STM. A study by Cui *et al* on the (100) surface of Ag-In-Yb 1/1 approximant reported that puckered layers are less stable than flat layers [29]. Moreover, the atomic density of flat layers is much higher compared to puckered layers. For example in a single unit cell there are 24 atoms in

a flat layer whereas only 12 and 8 atoms in puckered layers located at Z = 0.528 nm and 0.250 nm respectively. Therefore, it can be assumed that the terraces are formed at flat layers which cut the cluster centre and have the highest atomic density.

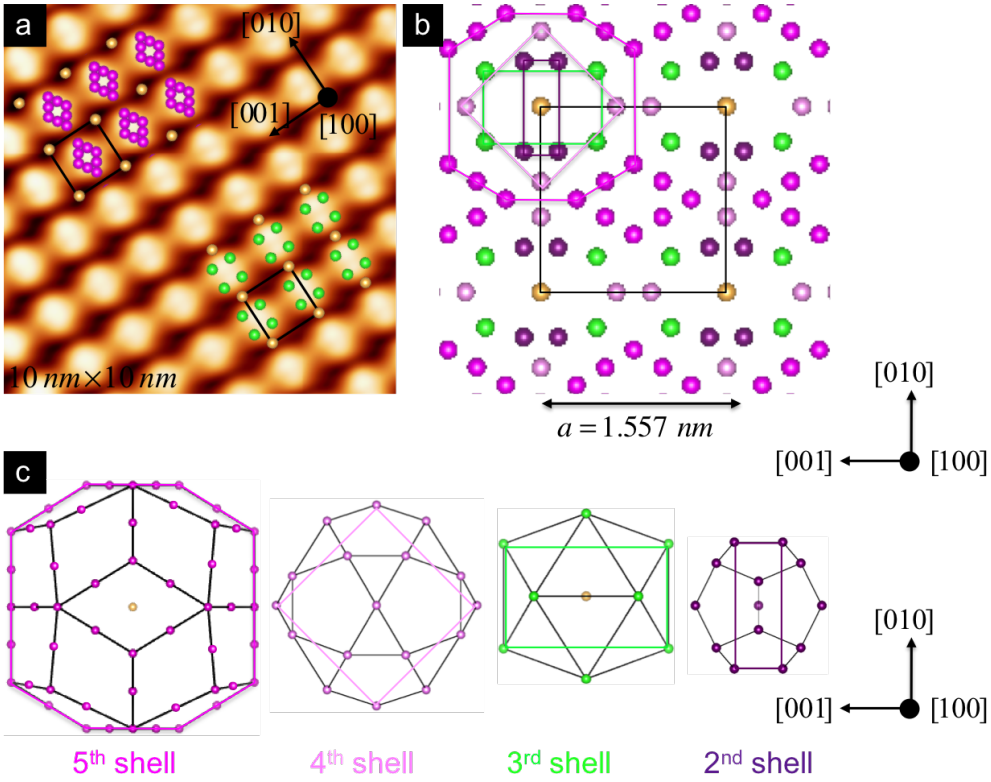

Figure 4.8: (a) 10 nm × 10 nm STM image showing protrusions on the Ag-In-Tb (100) surface arranged with a square unit cell of dimension 1.50 ± 0.02 nm. The (100) structure model is superimposed in two different possible ways. (b) A (100) structure model from a plane which cuts the centre of the RTH clusters, showing a square unit cell linking protrusions. Atoms of different shells of the RTH cluster are highlighted. (c) Four successive shells of RTH cluster projected along the [100] direction. Atoms which lie on the cluster centre plane are highlighted.

The black lines in Fig.4.7(a) indicates that rows of protrusions in the adjacent terraces are shifted by a half of lattice constant (a/2) in the direction normal to the rows. This is expected in a bcc structure if the terraces are formed at the lattice planes which intersect the body centre and faces of the cube. The observation of the shift thus supports our interpretation that the terraces are formed at the planes intersecting the centre of the RTH clusters. Point defects (vacancies) were observed on the (100) surface of both systems. These defects are highlighted in both Fig.4.7(a) and (b) with white circles.

Since the structure of the (100) facet of both Ag-In-Tb and Ag-In-Gd systems is very similar, high resolution STM images of the Ag-In-Tb system only are shown. The high resolution STM images of the fine structure of the (100) facet reveal protrusions on the

terraces, arranged with a square unit cell, as shown in Fig. 4.8(a). The distance between protrusions is 1.50 ± 0.02 nm, which is obtained from the fast-Fourier transform (FFT) of the image using the relation ($a = 2\pi/a^*$). The separation of protrusions of the (100) facet of Ag-In-Gd (1.52 ± 0.05 nm) [28] is very similar to Ag-In-Tb. These values are in a good agreement with the bcc lattice constant for the Ag-In-RE 1/1 approximants [22]. The FFT of the STM image, shown in the inset in Fig.4.6, is compatible with the square lattice, and also indicates that the surface is well-ordered. The size of the protrusions is about 1 nm, which is much larger than the usual size of features resulting from a single atom. This means atomic resolution was not obtained.

Because of the lack of atomic resolution, it is not possible to relate the protrusions in STM to the atomic structure model unambiguously. However, there seems to be two possible ways that the protrusions can be explained. In order to illustrate this, we present the structure of the (100) plane intersecting the centre of RTH clusters in Fig.4.8(b). Atoms belonging to different shells of the RTH cluster are marked. Since the [100] direction is along two-fold axes of the RTH cluster as explained before, the surface truncated shells show two-fold symmetry around the vertices of the unit cell.

The (100) atomic structure is superimposed to the STM image in Fig.4.8(a), in two possible ways. the first possibility is that the protrusions would be observed if each two Tb atoms of the third shell of the two neighbouring clusters along [010] are electronically coupled and thereby produce an enhanced density of states. The second possibility is that the Ag/In atoms of the outermost shell of the four neighbouring RTH clusters, which appear as a diamond in the centre of the unit cell, would contribute to the tunneling current producing the protrusions. However, in this case, we would expect to observe protrusions elongated along the [010] direction, i.e along the the diagonal of the diamond. In fact, the (100) surface of Ag-In-Yb approximant often shows elongated protrusions. STM data alone without theoretical calculations are insufficient to confirm that protrusions are related to one of these two possible structures, or to a new unknown structure.

(310) and ($3\bar{1}0$)

The step/terraced morphology of the (310) surface of both Ag-In-Gd and Ag-In-Tb systems are shown in the Fig.4.9(a) and (c) respectively. The step height for both systems are close to each other. A line profile is used to measure the step heights. The line profile, drawn over the terraces of Fig.4.9(a) is shown in Fig.4.9(b), showing that the terraces are separated by periodic steps of height 5.0 ± 0.20 nm. To understand the observed step heights in STM in terms of bulk separation planes, a bbc bulk unit cell of the Cd-Tb 1/1 approximant projected normal to the [310] direction is shown in Fig.4.9(c). This figure shows bulk planes which cut the centre of RTH cluster and are highlighted by dashed lines. These planes are separated by $a/\sqrt{10}$ nm which is the

expected periodicity ($a/\sqrt{h^2+k^2+l^2}$) along [310] direction. This is consistent with the observed step heights in the STM data. For the bcc lattice, the rows in the adjacent terraces are expected to be shifted along [$\bar{3}$10] by $2a/\sqrt{10}$. This shift is also observed in STM images.

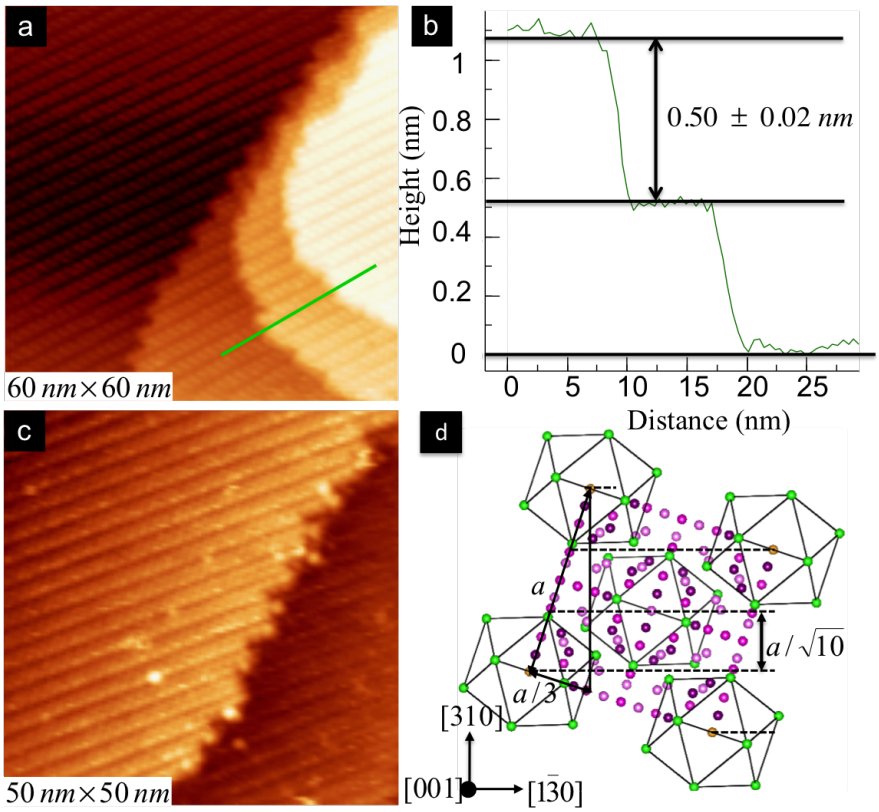

Figure 4.9: (a) 60 nm × 60 nm STM image showing the step/terrace morphology of the (310) surface of the Ag-In-Gd system; (b) A line profile across the terraces of image (a) showing that flat terraces are separated by steps of 0.50 ± 0.02 nm heights. (c) 50 nm × 50 nm STM image showing the step/terrace morphology of the (310) surface of the Ag-In-Tb system. (d) A bcc bulk unit cell of Cd-Tb 1/1 approximant projected normal to [310].

The observed structure on the (310) facet is the same for both Ag-In-Tb and Ag-In-Gd systems. Here only a high resolution STM image of the (310) facet of the Ag-In-Tb system is presented. A 10 nm × 10 nm STM image of the structure is shown in Fig.4.10(a). This reveals two different types of parallel rows. One row exhibits fine features forming a zigzag pattern and the other row consists of protrusions. Both rows show an atomic scale resolution. The fine features in the zigzag row are at 0.63 ± 0.02 nm. Two brighter spots are observed within the protrusion, which are at a separation of 0.58 ± 0.03 nm.

The high resolution STM image of the terrace is consistent with the atomic structure of the plane intersecting the centre of the RTH cluster. The structure of the plane

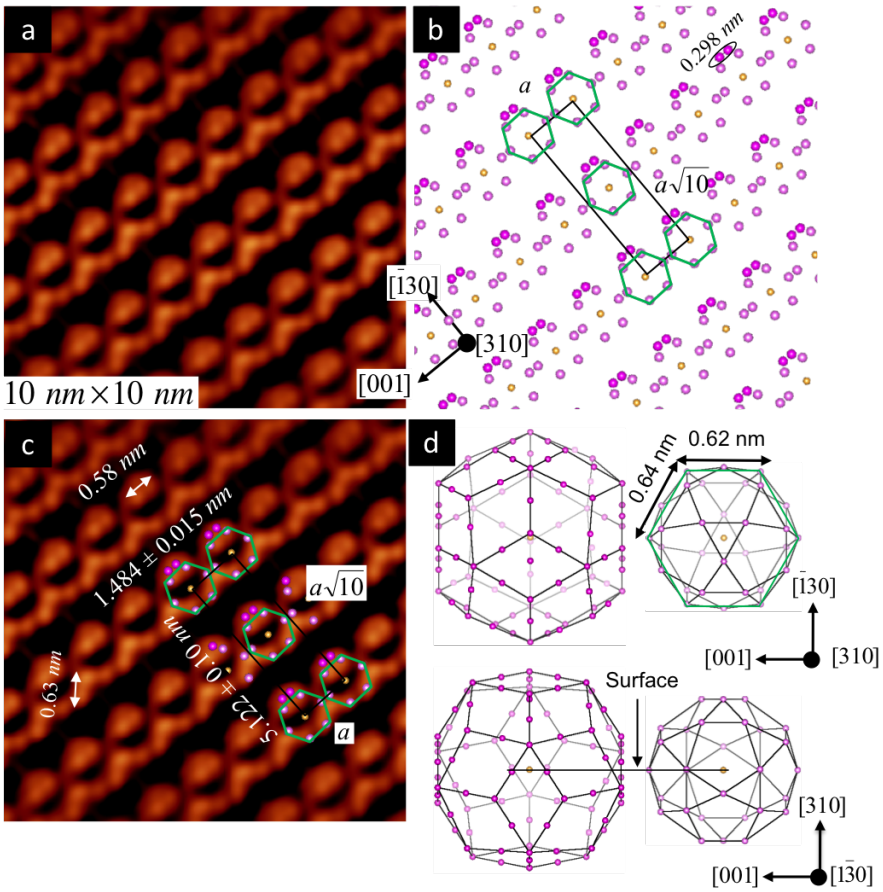

Figure 4.10: (a) 10 nm × 10 nm STM image showing a high resolution STM image of the (310) facet of the Ag-In-Tb; (b) Atomic structure of the (310) plane intersecting the centre of the RTH clusters. The Ag/In atoms marked by a hexagon belong to the fourth shell of the RTH cluster. A centre-rectangle unit cell of dimensions a and $a\sqrt{10}$ is highlighted. (c) For clarity, the STM image in (a) is duplicated with a unit cell from the model structure (b) overlaid. (d) Fifth and fourth shells of the RTH cluster in side and top view. Atoms appearing in the surface layer are marked by a hexagon.

extracted from the model is shown in Fig.4.10(b). The surface unit cell is a centred rectangle, with lattice points considered at the centre of the RTH cluster. The lattice points are decorated by Ag/In atoms forming a hexagon. The hexagons belong to the fourth shell of the RTH cluster (Fig.4.10(d)). In order to describe the STM images, we also need to consider atoms from the layer underneath, which is 0.02 nm from the top layer. These atoms belong to the fifth shell and line up along one side of the hexagons, i.e., along the [001] direction. The atomic structure is superimposed on the STM image in Fig.4.10(c), for clarity only one unit cell is shown. As seen, almost all the features of the two rows can be explained by the atomic structure. The zigzag pattern is formed by the Ag/In atoms of the fourth shell, whereas the protrusions are contributed by the fourth and fifth shell atoms.

The $(3\bar{1}0)$ facet is observed only once in the STM image in Fig.4.5(c). This facet is only observed in the Ag-In-Gd system. The $(3\bar{1}0)$ and (310) facets are equivalent in atomic structure. As the area of the observed $(3\bar{1}0)$ facet is very small, atomic resolution in STM from this facet was not achieved. However, the FFT of the $(3\bar{1}0)$ facet confirms the same symmetry and the same unit cell as the (310) facet. The FFT is shown in Fig.4.6.

(501)

STM images from the (501) facets also reveal a step-terrace structure. The terraces of the (501) facet are found to be separated by steps of 0.30 ± 0.01 nm height. The measured step heights correspond to the expected periodicity along [501] which is $a/\sqrt{26}$. Fig.4.11(a) is a 15 nm × 15 nm STM image of the (501) facet showing the step/terrace structure.

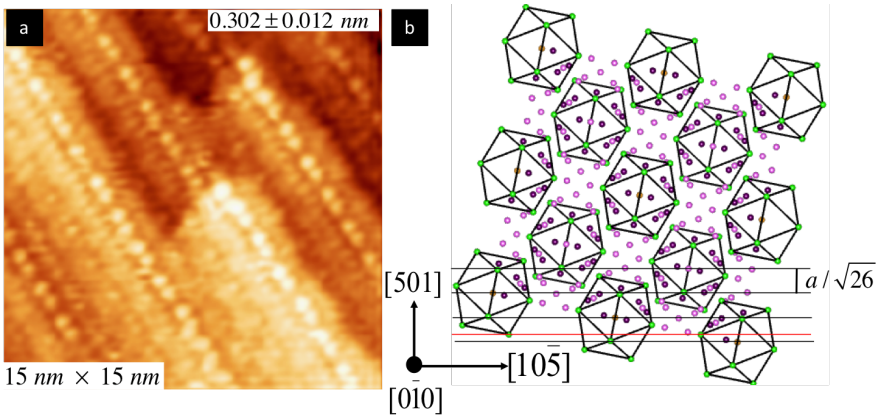

Figure 4.11: (a) 15 nm × 15 nm STM image showing the step/terrace morphology of the (501) facet of the Ag-In-Tb system. Terraces are separated by steps of 0.302 ± 0.012 nm heights. (b) bcc bulk unit cells of the Cd-Tb 1/1 approximant projected normal to [501]. Black lines indicates planes which cut the centre of RTH clusters. These lines are separated by $a/\sqrt{26}$ nm and the red lines indicates the surface plane.

A high resolution STM image of a terrace is shown in Fig.4.12(a). It exhibits rows of bright dots (indicated by the black arrow). The rows are separated by 4.07 ± 0.07 nm. Faint dots are also observed in a row in-between the bright rows (indicated by the white arrow). The dots in both bright and faint rows are paired. The separation of the bright dots in the pair is 0.58 ± 0.02 nm. The bright dots are higher than the faint dots by 0.05 ± 0.01 nm. In addition to the rows, a band of fine structure is apparent between the bright and faint rows. The dots can be assigned to atoms. However, the structure in the band is the not clear because of poor resolution.

Most of the STM features on terraces can be explained by the atomic structure of a plane which intersects at 0.08 nm above the cluster centre. This plane is marked by

a red line in Fig.4.11(b) and Fig.4.12(d). The atomic structure of the plane is shown in Fig.4.12(b). The surface unit cell, which is a central rectangle with dimensions of a and $a\sqrt{26}$, is highlighted. The atomic structure of the plane is superimposed on the STM image in Fig.4.12(c). Here, we consider atoms from layers underneath as well. The undermost layer is at 0.03 nm from the top layer (see side view inset in Fig.4.12(c)). The position of Tb atoms matches exactly with that of the bright dots in STM. The faint dots coincide with Ag/In atoms from the second shell. The dots in the pairs are slightly displaced from the centre of the pair along [010], compared to the model. Similarly, the Ag/In atoms from fourth and second shells lay along the edge of the band of the fine features. The remaining atoms from the second shell, which lie in the bottom layer, are either not detected by STM or displaced along [010].

The observed difference in height between the bright and faint dots is consistent with the fact that the bright dots are from the top layer atoms, while the faint dots are from the atoms in the bottom layer. A few other features of the STM image, such as those in-between bright and faint dots, cannot be explained by the atomic structure of the selected plane. However, the atomic structure of other planes is very far from agreement with the STM images.

(301)

As expected from the bcc lattice structure, STM from the (301) facets reveals the same symmetry and periodicity as the (310) facets. For example the (301) facet shows similar step heights to the (310) facet. However, the detailed atomic structure is different for the (301) and (310) facets. Fig.4.13(a) is 9 nm $\times$ 9 nm STM image, showing the structure of the (301) facet. The structure shows parallel rows. The row consists of protrusions (indicted by a black arrow) and dots (indicted by a red arrow). Both protrusions and dots can be assigned to the atomic structure of the plane which intersects just 0.028 nm above the cluster centre. This plane is indicated by a red line in Fig.4.13(d) (bottom inset).

The atomic structure of this plane is shown in Fig.4.13(b), where the centred rectangle surface unit cell of dimensions a and $a\sqrt{10}$ is highlighted. The atomic structure is superimposed on the STM image in Fig.4.13(c). For clarity only a single unit cell is shown. The position of the dots matches with that of the second shell atoms, while atoms from the fourth shell may also contribute to the protrusions.

(411)

Fig.4.14(a) shows an STM image of the step/terrace structure of the (411) facet. The measured step height is found to be 0.346 $\pm$ 0.016 nm which is consistent with the expected periodicity ($a/\sqrt{18}$) along the [411]. The structure on the terraces of the (411) facets is shown in Fig.4.14(b). As the regular features in the STM images are

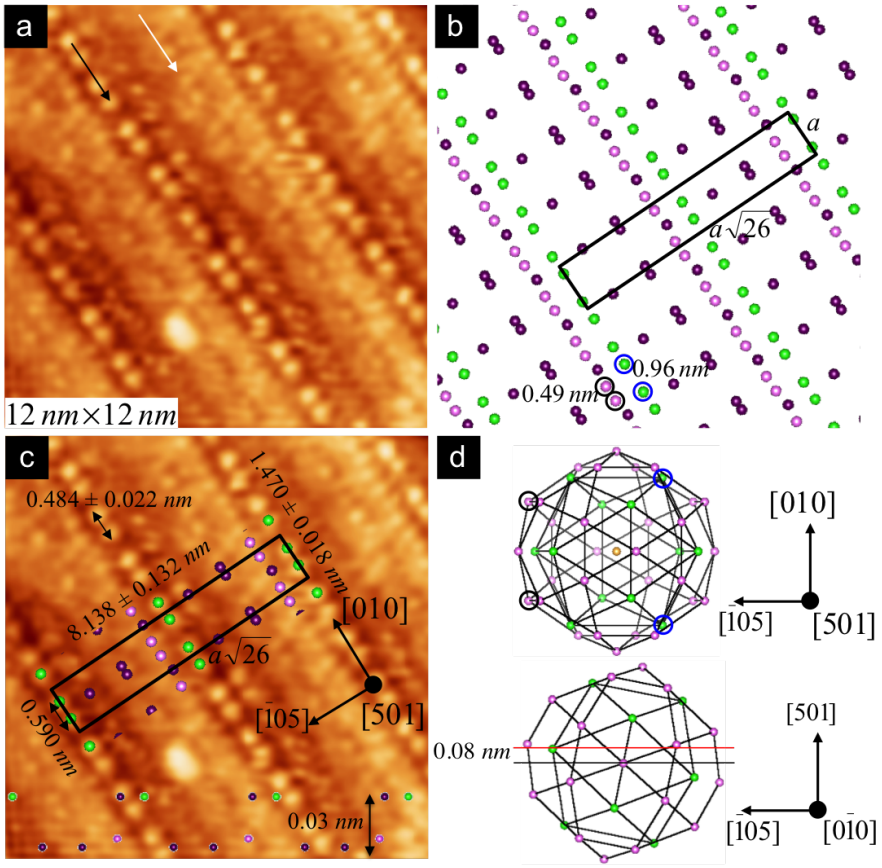

Figure 4.12: (a) 12 nm × 12 nm STM image showing atomic structure of the (501) facet of the Ag-In-Tb system. (b) Atomic structure of a bulk plane which intersect at 0.08 nm above the cluster centre. A centred rectangle unit cell with a and $a\sqrt{26}$ dimensions, is highlighted. (c) STM image (a) with atomic structure (b) superimposed. For clarity only one unit cell is shown. The bottom inset is the side view of (b) which show the separation between the top surface plane and the subsurface plane. (d) Fourth and third shells of the RTH cluster in top and side view with both planes which cuts the RTH cluster centre (black line) and surface-terminated plane (red line) marked. Atoms appearing in the surface layer are marked.

of about 1 nm in diameter, i.e., no atomic resolution is obtained, it is not possible to assign the terrace in STM with the atomic plane of the model. However, the symmetry and size of the unit cell of the STM image can be compared with that of the (411) plane of the bcc lattice. In order to determine the unit cell, we analyse the autocorrelation function of the image (Fig.4.14(c)), in addition to the FFT analysis discussed above. The unit cell is found to be oblique, of size (2.554 ± 0.032 nm, 2.148 ± 0.058 nm, α = 65°) which is consistent with that of the (411) plane of the bcc model structure (2.582 nm, 2.202 nm, α = 64.76°).

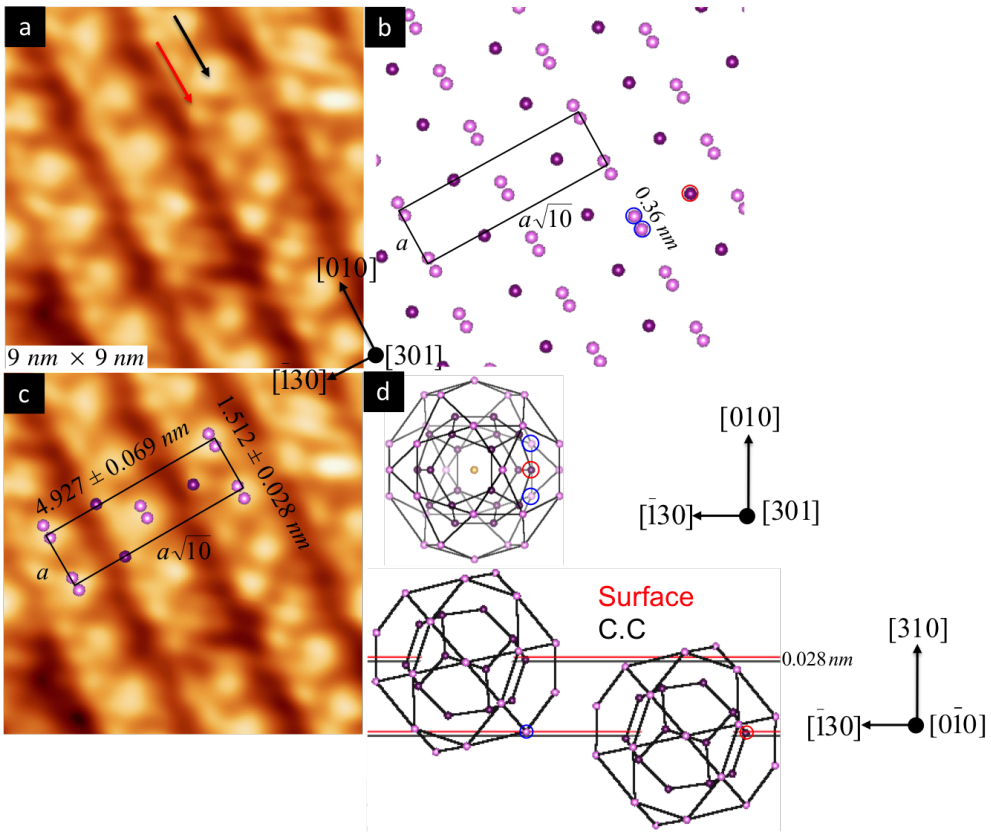

Figure 4.13: (a) 9 nm × 9 nm STM image showing the structure of the (301) facet of the Ag-In-Tb system. (b) Atomic structure of a bulk plane which intersects at 0.028 nm above the cluster centre. A centred rectangle unit cell with a and $a\sqrt{10}$ dimensions is highlighted. (c) STM image (a) with atomic structure (b) superimposed. For clarity only one unit cell is shown. (d) Fourth and second shells of the RTH cluster in top view and atoms appearing in the surface layer are marked (top inset). Side view of both shells with both the cluster centre plane (black line) and the surface-terminated plane (red line) indicated.

(710)

As with the (411) facets, the (710) facets do not show atomic resolution in STM. The finest observed features are protrusions of ≈ 1 nm size, which form parallel rows (Fig.4.15(a)). Rows of three different heights bunch together. These are marked with arrows with different colours, the row indicated by the black arrow being measured at the top. Although lack of atomic resolution does not allow assignment of the STM images with specific bulk atomic planes, the symmetry and size of the unit cell identified in STM is similar to that expected from the (710) plane of the bcc lattice, with a lattice constant of 1.557 nm. The (710) plane of the bcc lattice is shown in Fig.4.15(b), which is a vicinal plane consisting of narrow (100) and (301) planes (Fig.4.15(c)). The unit cell is a centred rectangle with dimensions of a and $a\sqrt{50}$, which is in agreement with

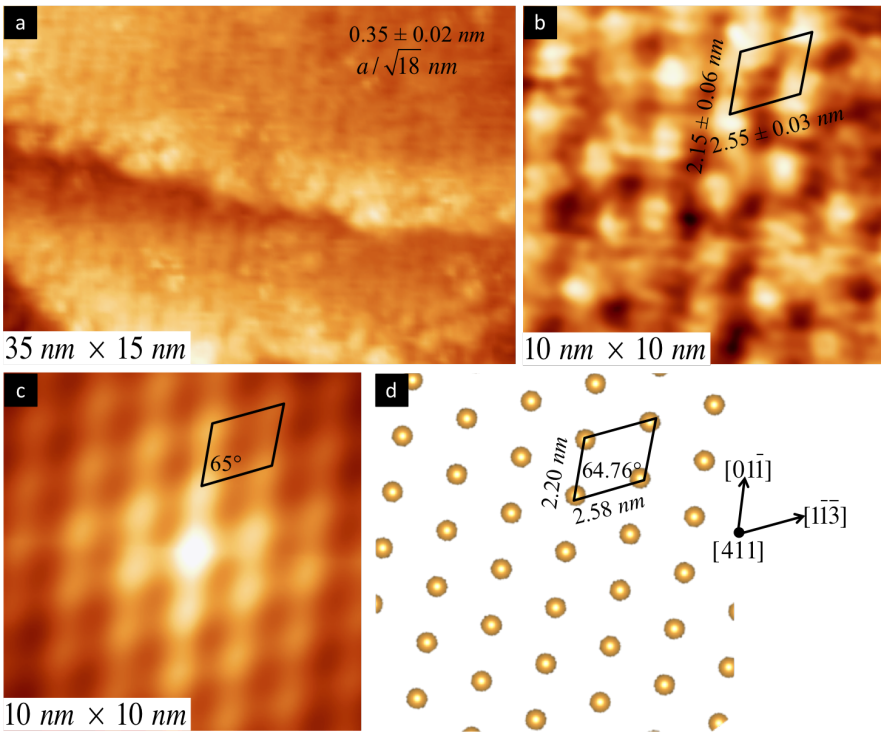

Figure 4.14: (a) 35 nm × 15 nm STM image showing the step/terrace structure of the (411) facet of the Ag-In-Tb system. (b) 10 nm × 10 nm STM image showing protrusions arranged in an oblique lattice. (c) Autocorrelation function of the STM image in (b). (d) The space lattice of the bcc structure in the (411) plane.

the unit cell observed in STM (1.465 ± 0.01 nm × 10.55 ± 0.30 nm). The symmetry of the (100) and (310) planes is also identified in STM.

Low Energy Electron Diffraction (LEED)

Fig.4.16(a) shows the LEED pattern of the (100) surface of the Ag-In-Gd 1/1 approximant which was recorded at 18 eV. The LEED pattern exhibits discrete diffraction spots arranged in a square unit cell. A square pattern is overlaid on the pattern and it is shown in Fig.4.16(b). It is found that most of the spots lie on the vertices of the square pattern consistent with the (100) facet. However, there are some spots displaced from the pattern. These spots are marked with green circles. These spots could come from other facets which are observed in STM. However, the facet giving rise to these spots could not be identified.

The LEED patterns of the (100) surface of the Ag-In-Tb 1/1 approximant are shown in the Fig 4.16(c) and (d) taken at 27 eV and 33 eV respectively. As can be seen some diffraction spots appear and disappear at different energies; for example the spots marked with yellow circles in Fig.4.16(c) which was taken at 27 eV disappeared in Fig.4.16(d) which was recorded at 33 eV and some other spots appeared in Fig.4.16(d)

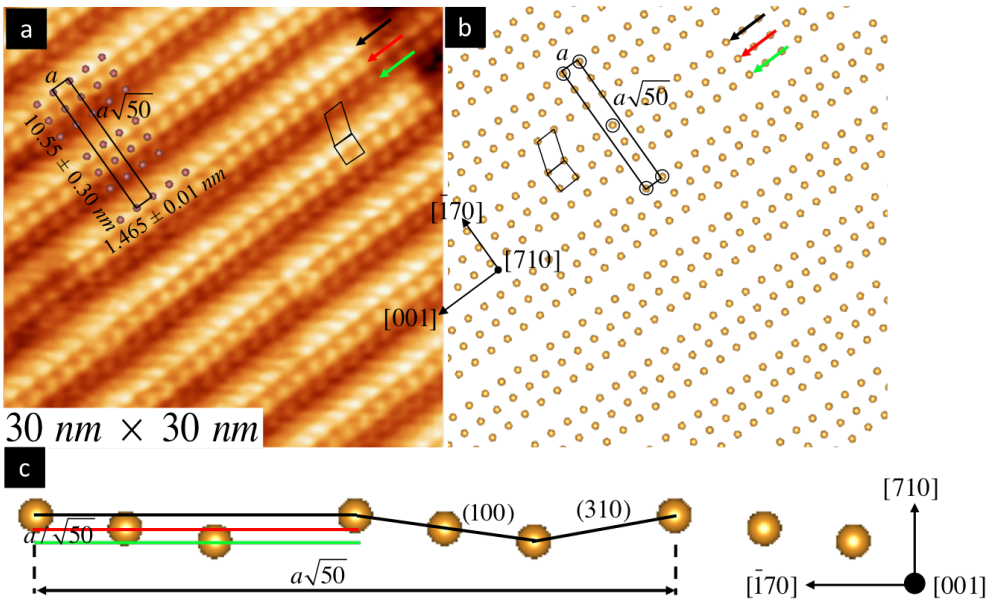

Figure 4.15: (a) 30 nm × 30 nm STM image of the (710) facet of the Ag-In-Tb system. (b) The bcc space lattice cleaved and projected along [710]. (c) A portion of the bcc lattice (side view) (b) projected normal to (710).

(marked with green circles) which do not appear in Fig.4.16(c). Moreover, there appears to be spots moving in different directions with changing energy. The arrows in Fig.4.16(c) indicates the direction of the spots with changing energy. The facets could not be identified at this time but this most likely could be due to the existence of different facets on the surface. Therefore these LEED patterns also reveal the existence of facets which is consistent with STM data discussed before.

4.2.3 The Structure of the (100) Surfaces of Ag-In-Yb 1/1 Approximant

The observation of the facets in both Ag-In-Tb and Ag-In-Gd approximants is in contrast with the result from the (100) surface of the Ag-In-Yb 1/1 approximant. The structure study of the (100) surface of the Ag-In-Yb 1/1 approximant which is isostructural to Ag-In-Tb and Ag-In-Gd 1/1 approximants was reported by Cui *et al.* [29]. The (100) surface of the Ag-In-Yb 1/1 approximant showed a periodic step/terraced structure [29] with no facets. The (100) surface of the Ag-In-Yb 1/1 approximant was prepared with both preparation methods mentioned in the experimental section. Both preparations reproduced the results reported by Cui *et al.* [29], without observation of facets.

Fig.4.17(a) shows the step/terrace structure of the clean Ag-In-Yb 1/1 approximant (100) surface. Unlike the (100) facet of Ag-In-Tb and Ag-In-Gd approximants which showed step heights of about half a lattice constant, the (100) facet of the Ag-In-Yb

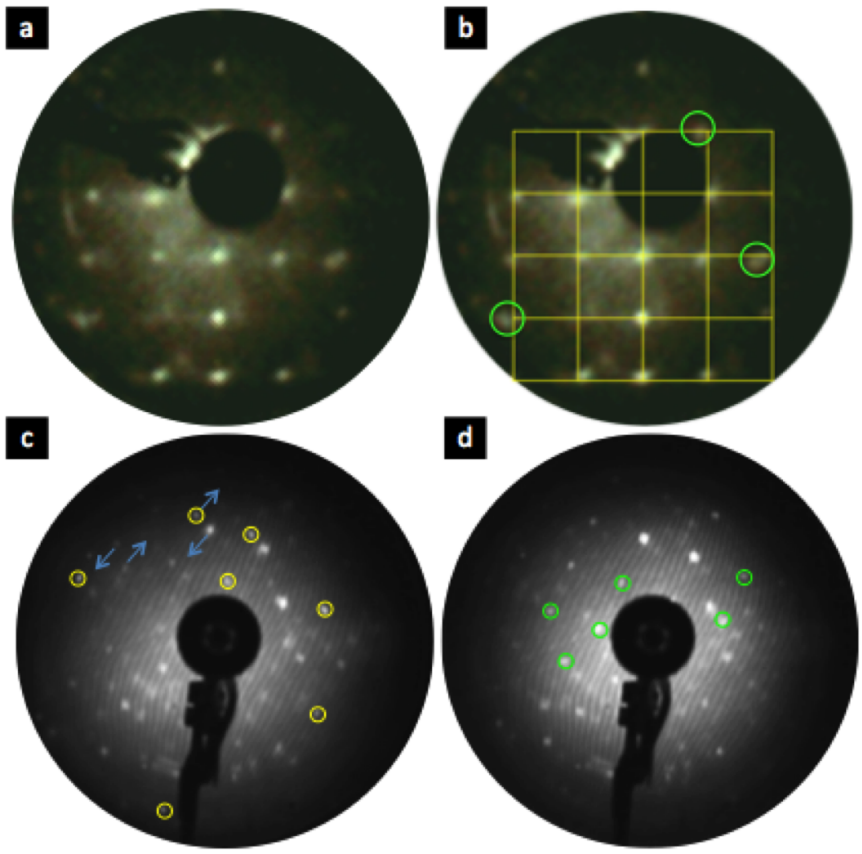

Figure 4.16: (a) LEED patterns of the (100) surface of the Ag-In-Gd 1/1 approximant recorded at 18 eV. (b) the same patterns as (a) with a square pattern overlaid; (c) and (d) LEED patterns of the (100) surface of the Ag-In-Tb 1/1 approximant recorded at 27 eV and 33 eV respectively.

approximant showed additional steps. Different terraces with different structures were observed, which are highlighted with labels A, B and C. The step heights measured using the line profile. The measured step heights are found to be A - B : 0.22 nm, B - C: 0.328 nm, C - A: 0.22 nm. The step heights between terraces of same structure such as A - A or B - B were found to be 0.768 $\pm$ 0.01 nm, which is consistent with half the lattice constant (0.771 nm) of the Ag-In-Yb approximant. These step heights are similar to those previously reported by Cui *et al.* [29].

The observed step heights are consistent with bulk plane separations. Fig.4.17(c) shows the atomic density distribution of bulk planes of the Ag-In-Yb 1/1 approximant along [100]. The figure shows bulk planes of different atomic density. The planes which cut the cluster centre have the highest atomic density. These planes are located at 0, $a/2$ and a, and they named as plane A. There are also other two planes located at 0.246 nm and 0.525 nm, which have the second highest atomic density. These planes can be considered as planes B and C respectively. The separation of these planes (A-B:

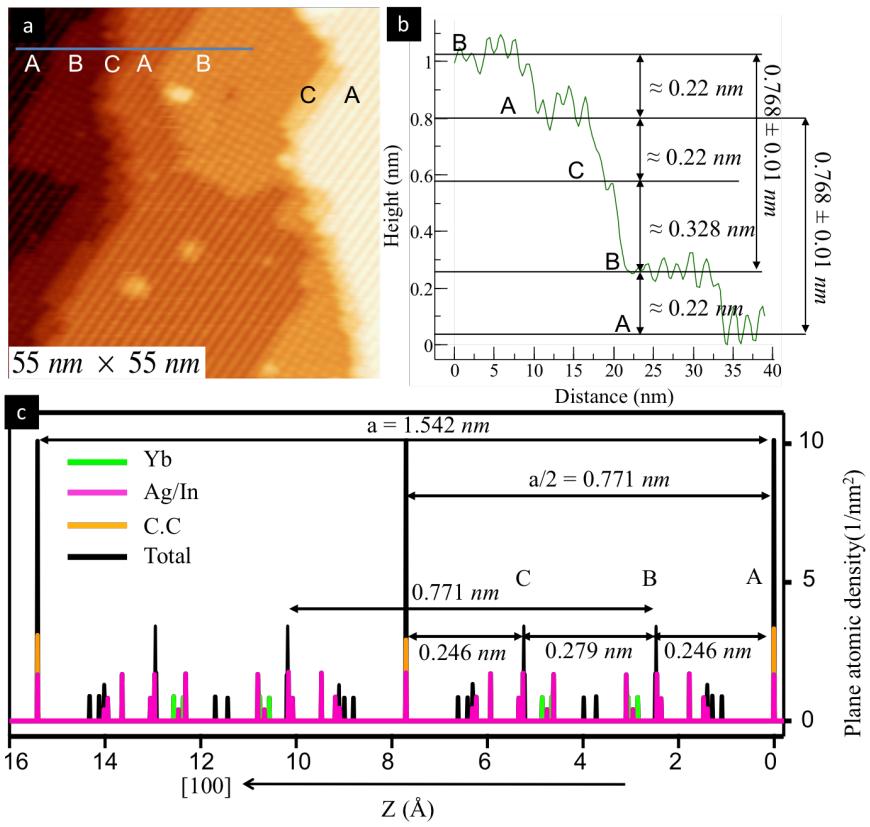

Figure 4.17: (a) 55 nm × 55 nm STM image showing the step/terrace structure of the (100) of the Ag-In-Yb; (b) line profile over STM image (a); (c) The bulk density distribution of the Ag-In-Yb 1/1 approximant. Planes which cut the cluster centre have the highest atomic density.

0.246 nm, B-C: 0.279 nm, C-A: 0.246 nm, A-A or B-B: 0.771 nm) is similar to what was observed in the STM data. However, due to the lack of atomic resolution on the terraces, it is difficult to assign terraces to bulk planes.

As shown in Fig.4.18(a) terraces A and B reveal different structure. Terrace A shows a stripe pattern of protrusions whereas the protrusions of terrace B are arranged in a square unit cell. Terrace C was not large enough to image the fine structure. Fig.4.18(b) and (c) show STM images of terrace A and B respectively. Unlike its parent quasicrystals [16, 119, 120] and like other 1/1 approximants Ag-In-Tb and Ag-In-Gd, atomic resolution could not be achieved on the (100) facet of this system. The distance between protrusions, measured from the FFT of the STM image, is 1.537 ± 0.02 nm. This is consistent with the lattice constant of the Ag-In-Yb 1/1 approximant [29].

Fig.4.18(d) shows the LEED pattern (31 eV) from the surface. The LEED pattern shows discrete diffraction spots arranged with square symmetry and confirms the long range order of the surface. Here additional spots were not observed i.e facets are absent,

which is consistent with STM data described above.

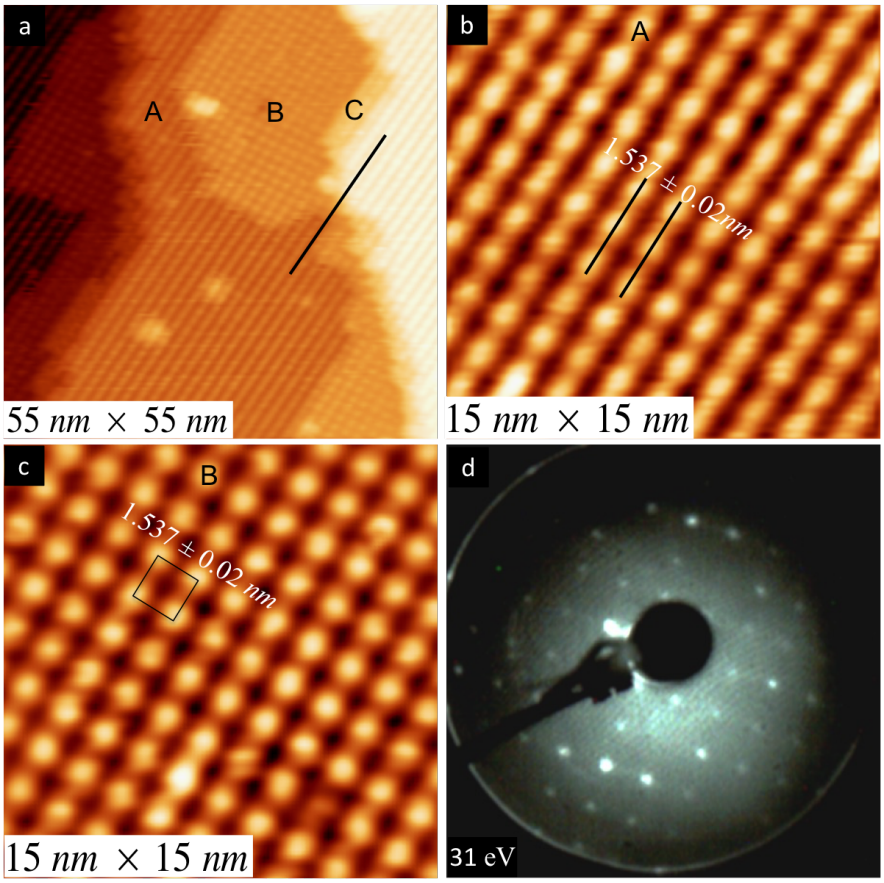

Figure 4.18: (a) 55 nm × 55 nm STM image showing the step/terrace structure of the (100) surface of Ag-In-Yb. (b) 15 nm × 15 nm STM image showing the stripe like structure on the terrace A. (c) 15 nm × 15 nm STM image of terrace B, showing protrusion arranged in a square unit cell. (d) LEED pattern (31 eV) of (100) surface of Ag-In-Yb 1/1 approximant, showing discret spots confirm long range order of square symmetry of the surface.

4.2.4 Discussion

Various factors that may influence the stability of the facets were investigated. These include atomic density, chemistry, and bonding between atoms in the surface and sub-surface regions. First the density of lattice points in a simple bcc lattice, without considering atoms has been calculated. The density is calculated using the fact that the density of lattice points in a plane (hkl) is proportional to the inter-planar spacing (d_{hkl}) [125].

For the analysis, Miller planes with indices up to (999) were considered and then around 20 planes were chosen which make an angle up to 20° with (100). The planes were then sorted based on the density of lattice points (Table 4.2). Equivalent planes

Table 4.2: Density of lattice points in a bcc lattice

Facets	Angle with (100)	d_{hkl}/a
(100)	0°	0.5
(310)	18.43°	0.3162
(301)	18.43°	0.3162
(411)	19.47°	0.2357
(501)	11.31°	0.1961
(611)	13.26°	0.1622
(710)	8.13°	0.1414
(721)	17.71°	0.1360
(811)	10.02°	0.1230
(410)	14.03°	0.1212
(610)	9.46°	0.0821
(612)	20.43°	0.0780
(710)	11.42°	0.0700
(810)	7.12°	0.0620
(830)	20.55°	0.0585
(913)	19.35°	0.0524

in the table were omitted. It was found that the planes with high density lattice points (highlighted with yellow in Table 4.2) correspond to the observed facets, with the exception that the (611) facet is not seen in STM. The sum of the Miller indices of these high density planes is an even number, except for (100). If the sum is odd, the density of lattice points would be much lower. Thus, it is expected that facets would be formed along these planes in a simple bcc lattice crystal. However, the bcc lattice of the current system is associated with an RTH cluster with a complex atomic distribution. Therefore, it is interesting to determine the atomic density of the facet planes and compare with the lattice point density.

However, it is not straightforward to define an atomic plane in a complex crystal, where atoms are continuously distributed in the crystal, unlike in a simple crystal where atomic planes are well separated, (at least the low index planes). Therefore, we hypothesise that atoms within a certain thickness form a plane. We calculated the density of planes with different thickness (0.03 and 0.07 nm). It was found that the calculated atomic density, in all cases, correlates well with the density of lattice points, i.e., the atomic density is proportional to the density of lattice points. However, the atomic density of the plane in these systems is much smaller than in a normal metal. For example, the density of the (111) surface of elemental fcc Tb is 0.178 atoms/Å^2. The density of the (100) plane in the Ag-In-Tb approximant is only half of this value. The (100) plane has the highest atomic density among the observed atomic planes (Table 4.3). The density of the other observed facet planes is lower than (100) by a

factor of four or more. As we will see below, atoms in the top surface layer are so far apart that they are less likely to be bonded together, i.e., they have to bond with sub-surface atoms in order to be stabilised.

Table 4.3: The atomic density and chemistry of the observed facets in the model of the Cd-Tb 1/1 approximant estimated from the top surface. The atomic density is calculated by counting atoms in the unit cell divided by the area of the unit cell. Regarding the chemistry, atoms belong to different RTH cluster shells were first identified then the information about occupancy of Ag, in and Yb in different shells as described in section 4.2.2 is used.

Facets	Atomic density (atom/Å^2)	Chemistry
(100)	0.0824	$Ag_{43}In_{37}RE_{20}$
(310)	0.0208	$Ag_{40}In_{60}RE_{0}$
(501)	0.0122	$Ag_{33}In_{40}RE_{27}$
(301)	0.0078	$Ag_{33}In_{67}RE_{0}$
(710)	no atomic resolution	-
(411)	no atomic resolution	-

Before discussion of the bonding configuration of the surface atoms, the chemical composition of the surface layer is analysed, using information about the occupancy of Ag and In in different shells as outlined in Section 4.2.2. The estimated composition of the top-most layer is shown in Table 4.3. To calculate the density, we consider atoms of only the topmost layer(s) which are used to describe the STM images. The atomic density given in Table 4.3 is also from these layers. As can be seen, the (100) surface has a composition similar to the bulk. The other facets are In-rich in all facets. This is in agreement with observations on the Ag-In-Yb quasicrystal. All three high symmetry surfaces; two-, three- and five-fold; of this system are found to be terminated at a bulk plane containing In as the majority constituent [120].

Finally, the likelihood of bonding between surface atoms is discussed. The nearest neighbour species and their separation in the top surface layer was determined (Table 4.4). For instant, the minimum separation of the nearest neighbours (NN) in the (310) facet (Fig.4.10(b)) is 0.298 nm, which is in-between a Ag - Ag bond. Both atoms belong to the mid-edge of the fifth shell. Therefore, these atoms could be identified as Ag, i.e., the occupancy of these sites by Ag is 100 % and represented by Ag(1). The number in parentheses corresponds to occupancy. Similarly, the maximum separation of the nearest neighbours in this facet is 0.624 nm, which will be in-between atoms in fourth shells, i.e., between Ag/In - Ag/In atoms. As the fourth shell contains 20 % Ag and 80 % In, as described in Section 4.2.2, we represent this NN pair by Ag(0.2)In(0.8) - Ag(0.2)In(0.8). As the separation of Ag(0.2)In(0.8) - Ag(0.2)In(0.8) is far larger than the atomic diameter of Ag or In (atomic diameter of In, Ag and Tb are 0.312, 0.330, and 0.450 nm respectively), it is less likely that these atoms will be bonded. These atoms

Table 4.4: Distance between atoms in the topmost and subsurface of 1/1 Ag-In-Tb approximant. The subsurface atoms are marked bold. The number in parentheses correspond to occupancy of atoms. Refer to text for further discussion of occupancy.

Facets	Distance (nm)	Atoms
(100)	0.281	Ag(1)-Ag(0.63)In(0.37)
	0.328	Tb(1)-**Ag(0.20)In(0.80)**
	0.333	Tb(1)-Ag(0.60)In(0.40)
(310)	0.294	Ag(0.20)In(0.80)-**Ag(0.63)In(0.37)**
	0.294	Ag(0.20)In(0.80)-Ag(0.20)In(0.80)
	0.302	Ag(0.20)In(0.80)-Ag(0.63)In(0.37)
	0.298	Ag(1)-Ag(1)
	0.328	Ag(0.20)In(0.80)-**Tb(1)**
	0.338	Ag(0.20)In(0.80)-**Tb(1)**
	0.341	Ag(1)-**Tb(1)**
(501)	0.288	Ag(0.60)In(0.40)-Ag(0.60)In(0.40)
	0.294	Ag(0.60)In(0.40)-**Ag(0.20)In(0.80)**
	0.323	Tb(1)-**Ag(0.20)In(0.80)**
	0.323	Ag(0.20)In(0.80)-**Tb(1)**
(301)	0.368	Ag(0.20)In(0.80)-Ag(0.20)In(0.80)
	0.294	Ag(0.60)In(0.40)-**Ag(0.20)In(0.80)**
	0.297	Ag(0.20)In(0.80)-**Ag(0.20)In(0.80)**
	0.333	Ag(0.60)In(0.40)-**Tb(1)**

must therefore be bonded with subsurface atoms. Therefore, the nearest neighbour of each surface atom in the subsurface is determined as well, which is shown in the same table. The Ag(0.2)In(0.8) species in the topmost layer has nearest neighbour atoms in the subsurface with a separation of 0.328 nm. The subsurface atoms are Tb. Therefore, a bond is likely to be occurred between Ag(0.2)In(0.8) - Tb(1).

From a similar analysis of bonding in the other facets, we can extract common features. The atoms in the fourth shell, which are mostly In, are likely to be bonded with third shell Tb atoms, in the (100), (301) and (501) facets. In our analysis, we considered the atomic diameter of atoms. For example, in the (310) facet the separation of the Ag(0.2)In(0.8) - Ag(0.63)In(0.37) pair is 0.294 nm and that of Ag(0.2)In(0.8) - Tb(1) is 0.328 nm. Since Tb atom is larger than In by 44 %, the gap between atoms in the Ag(0.2)In(0.8) - Tb(1) pair is less than in Ag(0.2)In(0.8) - Ag(0.63)In(0.37). In the (301) facet, Tb atom is likely to be bonded with atoms in the second shell, which has 40 % of In. Ag/In-Ag/In bonds also occur in all surfaces but these bonds will be a minority. Therefore, we can conclude that the majority constituent of the surface, In, is bonded with Tb and that strong bonding occurs between the atoms in the third and fourth shells.

4.3 Conclusions

The first structural study of Ag-In-RE 1/1 approximant surfaces (RE = Tb, Gd and Yb) is presented. STM and LEED were used to characterise the surface. Preparation conditions which produce a surface with step/terrace morphology were found for all approximants. The Ag-In-Tb and Ag-In-Gd surfaces develop facets along certain crystallographic directions. Periodic steps were observed for facets. The observed step heights in different facets were consistent with the expected periodicity of the facets; for example the observed step (0.50 ± 0.02) nm for (310) facet is consistence with $a/\sqrt{10}$ which is the expected periodicity along [310]. Comparing the step heights and high resolution STM images of facets with the bulk structure model it was found that surfaces are bulk (RTH cluster) terminated similar to their parent quasicrystals. The observed facets were in agreement with calculations of the density of lattice points and the stability of the facets was found to be due to bonding of the surface atoms and atoms of the layer below the surface. It is also found that the strongest bond is often between third shell Tb atoms and fourth shell In atoms (fourth shell is mostly occupied by In). This is in agreement with the results obtained from the calculations for the electronic structure and surface stability of the Ag-In-Ca intermetallic [126]. It is reported that the hybridisation between Ca-3d states and Ag/In-sp states contributes in stabilising the surface. The existence of facets is confirmed by LEED patterns. In contrast to the (100) surface of Ag-In-Tb and Ag-In-Gd approximants, no facets were observed on the (100) surface of the Ag-In-Yb 1/1 approximant.

Chapter 5

The Growth of Bi on the five-fold Surface of the *i*-Ag-In-Yb Quasicrystal

5.1 Introduction

A review of the literature on thin film formation on quasicrystal surfaces will be presented in this chapter, followed by the first study of the formation of a Bi thin film on the five-fold surface of the *i*-Ag-In-Yb quasicrystal surface using scanning tunneling microscopy (STM). The motivation of chosing Bi to deposit is explained in the next page.

5.1.1 Epitaxy on Quasicrystal Surfaces

Quasicrystal surfaces have provided a novel template to grow thin film of materials because of their unique five-fold and ten-fold rotational symmetry and long range aperiodic order [127] as well as the existence of a large range of adsorption sites in comparison with conventional crystals [11, 12, 10]. There seems to be three different possibilities of film structure during growth of epitaxial films on quasicrystal surfaces. The first possibility is the formation of a film which has no structural relationship to the substrate. The second possibility is the formation of a crystalline film which is orientationally aligned to the substrate. Finally, the most interesting possibility is pseudomorphic growth in which the film grows with a structure commensurate with the substrate structure [128, 129, 130].

The main motivation of using quasicrystals as substrates is to produce 'artificial' single element quasicrystals with reduced chemical complexity. The study of single element quasicrystals will potentially play a crucial role in understanding the influence of quasiperiodicity on the physical properties of quasicrystals [11, 61, 131]. Another motivation of using quasicrystals as a template is to explain how the nucleation and growth of adatoms are affected by unusual (forbidden symmetry and pseudogaps) properties

of quasicrystals [9].

For this purpose, various elements have been deposited on different quasicrystal surfaces [9, 127] and different surface techniques have been employed to study thin film formation.

Epitaxy on Al-based quasicrystal Surfaces

Thin film deposition has been carried out on various Al-based quasicrystal surfaces such as the five-fold surface of the *i*-Al-Pd-Mn and *i*-Al-Cu-Fe quasicrystals and the ten-fold surface of the *d*-Al-Ni-Co quasicrystal. Different elements have been deposited on these surfaces. Some of the elements showed no order, some of them showed crystalline structures and some of them showed quasicrystalline structures. Those which formed quasicrystalline structures on these quasicrystal surfaces are listed in the Table 5.1.

Table 5.1: List of elements which form a quasicrystalline film on Al-based quasicrystal surfaces. 5*f*, 10*f*, *i* and *d* stand for five-fold, ten-fold, icosahedral and decagonal respectively. See the glossary for acronyms.

Surfaces	adsorbates	Techniques	Coverage	References
5f-*i*-Al-Pd-Mn	Bi	HAS, LEED, *ab initio*	Monolayer	[132, 133]
	Cu	STM,LEED,MEIS	Multi-layer	[129, 131, 134]
	Co	STM, LEED	Multi-layer	[135]
	Si	STM	Sub-monolyaer	[136]
5f-*i*-Al-Cu-Fe	Sn	STM	Monolayer	[137, 138, 139]
	Al	STM	Sub-monolayer	[140]
10f-*d*-Al-Ni-Co	Bi	HAS, LEED	Monolayer	[132]
	Sb	HAS, LEED	Monolayer	[132]
	Co	STM, LEED	Multi-layer	[135]
	Si	STM	Sub-monolayer	[141]
	Sn	STM, RHEED	Monolayer	[142]

Bismuth deposition on these surfaces will be reviewed as it is one of the elements used in the work of this chapter. Bismuth was one of the elements first found to demonstrate a monolayer of quasicrystalline structure after being deposited on the five-fold surface of *i*-Al-Pd-Mn [132]. Bismuth is a semi-metal of group V which crystallises with rhombohedral symmetry (A7 arsenic structure). This structure can be described as pseudocubic, with one atom per unit cell, or as hexagonal with six atoms per unit cell [143]. Elements of weakly bonded atoms such as group V are more likely to form quasicrystalline overlayers [144]. Bi overlayers have been studied intensively because Bi has different structural forms [127].

The quasicrystals used as substrates to grow Bi thin films have been Al-based. The formation of a quasicrystalline monolayers of Bi on the five-fold surface of *i*-Al-Pd-

Mn and tenfold surface of *d*-Al-Ni-Co was investigated using helium atom scattering (HAS) and low energy electron diffraction (LEED), by Franke *et al.* [132]. Thereafter, STM and reflection high-energy electron diffraction (RHEED) were used to study the growth of Bi on the five-fold surface of *i*-Al-Cu-Fe, and also showed the formation of a quasicrystalline monolayer of Bi and periodic islands with specific heights after the monolayer [145]. Following this, the nucleation and growth of a quasicrystalline Bi monolayer on the five-fold surface of *i*-Al-Pd-Mn was studied using scanning tunneling microscopy (STM) [146]. After completion of a quasicrystalline Bi monolayer, periodic islands with pseudocubic and pseudohexagonal symmetry were observed [144].

Epitaxy on the five-fold surface of the *i*-Ag-In-Yb quasicrystal

The five-fold surface of the *i*-Ag-In-Yb quasicrystal was also used as a first non Al-based substrate for epitaxial film growth. Recently the surface was used as template to grow a Pb film using various experimental techniques and theoretical calculations including STM, LEED, XPS and DFT [147]. Lead was deposited on the surface gradually and STM images were acquired at each coverage. STM images of the Pb film revealed different quasicrystalline Pb layers. Fig.5.1 shows STM images of various quasicrystalline Pb layers on the surface. The first layer is shown in Fig.5.1(a) which formed after 5 minute deposition of Pb. The Pb atoms in the first layer make pentagons of 0.92 $\pm$ 0.05 nm edge length and they are 0.11 $\pm$ 0.01 nm above the substrate. At this coverage the substrate protrusions were also observed and the pentagons formed by Pb atoms were found to be formed atop of the substrate protrusions. One of the pentagonal protrusions of the substrate with Pb pentagons on the vertices is highlighted in Fig.5.1(a). Small white pentagons represent Pb atoms and the grey larger pentagons represent the substrate protrusions.

Upon further deposition of Pb for 90 minutes, the Pb atoms make decagonal rings as shown in Fig.5.1(b). The Pb atoms at this coverage are at height of 0.31 $\pm$ 0.01 nm from the substrate. Therefore they can be considered as a second layer. At this coverage additional features were observed such as pentagons of 1.58 $\pm$ 0.1 nm edge-length which are at 0.28 $\pm$ 0.03 nm above the second layer. Thus this was considered to be the third layer. Pentagons of the third layer are rotated by $\pi/5$ with respect to each other. These are marked with white circles in Fig.5.1(d). Other features were observed in-between the first and the second, and second and third layers which were dubbed the intermediate layer. One of these features which is above the second and below the third layer is shown (circle number 2) in Fig.5.1(c). In summary, a quasicrystalline Pb multilayer was resolved on the surface using STM [147].

The quasicrystalline multilayer of Pb was further confirmed using XPS. In addition to the layers observed in STM, XPS detected another layer between substrate and first layer. This layer was called the underlayer. This layer was not observed in STM being

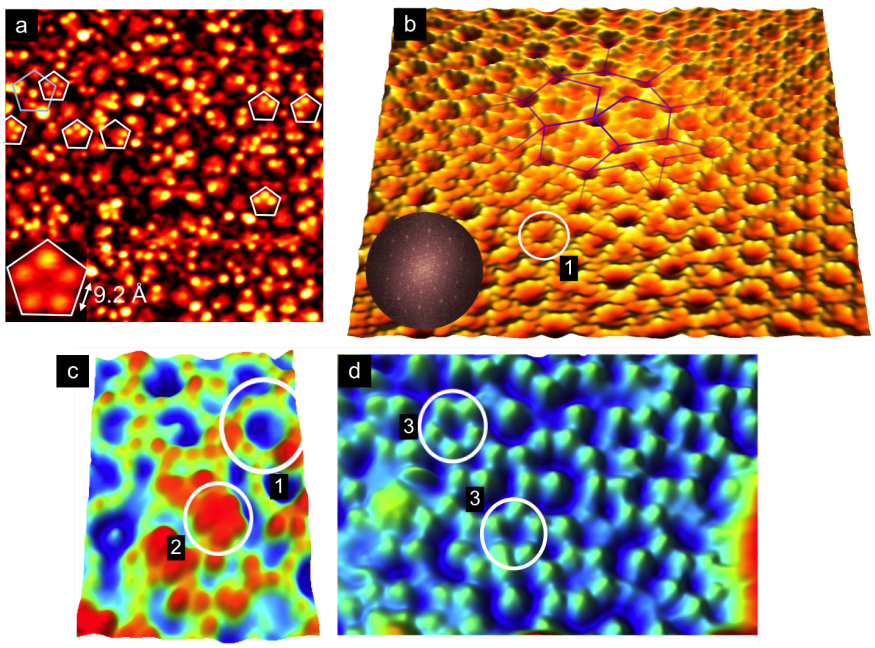

Figure 5.1: Quasicrystalline Pb multilayer on the five-fold surface of *i*-Ag-In-Yb quasicrystal. (a) 30 nm × 30 nm STM image of the first layer; (b) 30 nm × 30 nm STM image of second layer showing decagonal rings formed by Pb atoms. Left inset is the FFT of the image. (c) 30 nm × 30 nm STM image showing both second and intermediate layer. (d) 27 nm × 15 nm STM image showing the third layer. White circles 1, 2 and 3 represent second, intermediate and third layer respectively. Reprinted from [147].

underneath the first layer because STM provides the information on the topmost layer while XPS can probe a few surface layers [147].

The adsorption sites of Pb atoms were identified using STM images and DFT calculations. The adsorption sites for first layer Pb atoms were found to be in-between Ag/In rings and Yb rings of the substrate protrusions. These sites are marked with black dots in Fig.5.3(b). Pb atoms of second layer occupy the centre of Yb pentagons, and these are highlighted with red dots in Fig.5.3(b). These sites were found to be identical to the atomic sites of the RTH cluster above the surface. Pb atoms of different layers occupy atomic sites of specific chemical elements in the RTH cluster. For example, Pb atoms of the first layer occupy the sites of Ag/In atoms of the fifth shell while Pb atoms of the second and third layer occupy the Yb atomic site of the third shell. It was also found that the Pb-Pb atomic distance in the film plays a vital role in stabilising the film [147].

This Pb/5f-*i*-Ag-In-Yb work provided a motivation for further research, to test whether other elements grow a quasicrystalline multilayer on the fivefold surface of the *i*-Ag-In-Yb quasicrystal. For example Bi has been deposited on Al-based quasicrystals but only formed a pseudomorphic quasicrystalline monolayer (see Table 5.1). In the

Pb/5f-*i*-Ag-In-Yb system, it was reported that Pb-Pb atomic distance is important to stabilise the film. Thus In could be a good candidate to be deposited on the same surface as the surface itself is In-rich. Therefore, for the work of this thesis the five-fold surface of the *i*-Ag-In-Yb quasicrystal is used as substrate to grow both Bi and In. The details for both studies are presented in this chapter and the next respectively. Table 5.2 provides a list of thin film growth studies on the five-fold surface of the *i*-Ag-In-Yb quasicrystal.

Table 5.2: List of thin film growth studies on the five-fold surface of the *i*-Ag-In-Yb quasicrystal.

adsorbates	Techniques	Coverage	References
Pb	STM, LEED, XPS, DFT	quasicrystalline multilayers	[147]
Bi	STM	quasicrystalline bilayers	this chapter
In	STM, LEED	quasicrystalline bilayers	next chapter
Sb	STM, LEED	quasicrystalline bilayers	[148]
Pn	STM	quasicrystalline monolayer	[149]

5.2 Bismuth thin film on the five-fold surface of the *i*-Ag-In-Yb quasicrystal

5.2.1 Experimental Details

The Bridgman method was used to grow the single grain *i*-$Ag_{42}In_{42}Yb_{16}$ quasicrystal sample. The sample was then cut perpendicular to the five-fold axis. Prior to insertion into ultra high vacuum (UHV), 6 μm, 1 μm and 0.25 μm grades of diamond paste were used to polish the sample. Following polishing with each paste, the sample was immersed in an ultrasonic bath for 15 minutes to remove residual paste. Once the sample was inserted into the UHV chamber, it underwent repeated cycles of sputtering by Ar^+ ions (2.5 – 3 keV) for 30 minutes and subsequent annealing (at 440 °C for 2 – 4 hours) at a base pressure of 2×10^{-10} mbar. A pyrometer with emissivity of 0.35 was used to measure the temperature. This preparation resulted in a step-terrace structure with quasicrystalline order.

An Omicron EFM-3 electron beam evaporator was used to deposit Bi at room temperature with constant flux and the pressure was kept close to the base pressure during deposition. An Omicron variable temperature scanning tunnelling microscopy (STM) was employed to characterise the surface and the epitaxial films using constant current mode at room temperature.

5.2.2 Results

Substrate (i-$Ag_{42}In_{42}Yb_{16}$) Surface Structure

To understand the formation of Bi quasicrystalline layers, it is necessary to understand the structure of the clean surface first. The structure of the five-fold surface was first reported by Sharma et al. [16] and described in detail in Chapter Four, Section 4.1.1 The same results have been reproduced for the clean surface in this study.

Fig.5.2(a) is a 30 nm × 30 nm STM image showing pentagonal protrusions with a 2.50 nm edge length. The fast Fourier transform (FFT) of the image (not depicted here) showed tenfold symmetry which confirms the quasicrystalline long range order of the surface. The resolved pentagonal sets of protrusions have two different orientations which are rotated by 36° with respect to each other. They will be referred to as 'up' and 'down' pentagons which are marked as black and white pentagons respectively. Fig.5.2(b) is the structure model of a bulk plane which cuts the RTH cluster centre, deduced from the bulk structure model of the binary i-Cd-Yb quasicrystal [150]. Yellow dots represent cluster centre, green and light pink atoms represent Yb and Cd sites respectively. Cd atom locations are occupied by Ag and In atoms for this material. The cluster centres are located at the vertices of a Penrose P1 tiling. The Penrose P1 tiling consists of a pentagon, a thin rhombus (diamond), a star (pentagram), and a boat [57]. A patch of the tiling of 2.53 nm edge length is overlaid in Fig.5.2(b).

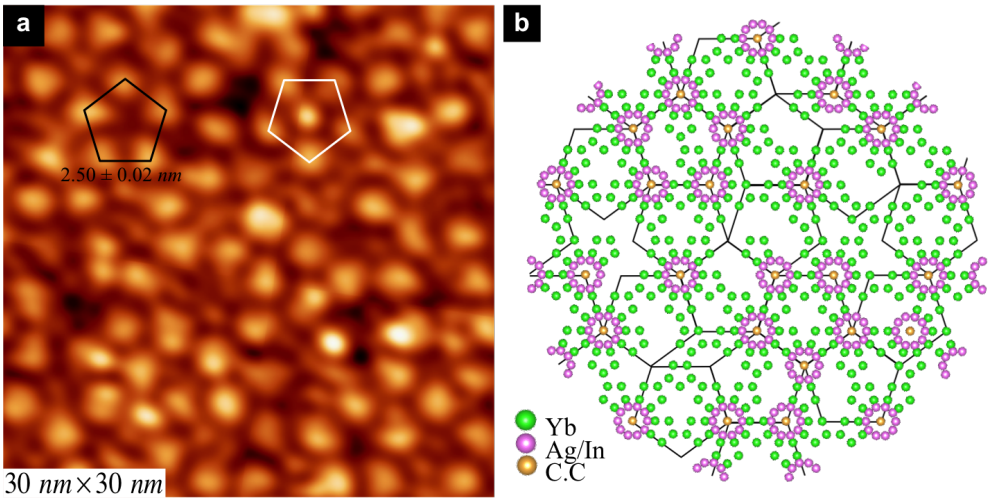

Figure 5.2: (a) 30 nm × 30 nm STM image of the clean surface of i-Ag-In-Yb showing pentagonal protrusions of 2.50 nm edge length. (b) In-plane atomic structure of a bulk plane, which cuts the RTH centre, showing pentagonal motifs with edge length of 2.53 nm. A Penrose P1 tiling of 2.53 nm edge length is superimposed on the model. Almost all cluster centres (yellow dots) are located at the vertices of the tiling. The vertices are decorated with two rings: light pink rings which corresponds to Cd (Ag/In) atoms of the fourth shell of the RTH cluster and a green ring which corresponds to Yb atoms of the third shell.

Room-Temperature Bismuth Deposition

Quasicrystalline Bi Layers

Bismuth was gradually deposited on the surface. Fig.5.3(a) depicts an STM image of 20 nm × 20 nm after depositing Bi for 5 minutes. The surface area covered by Bi atoms at this coverage is about 0.35 ML. Clean surface protrusions and single Bi atoms are resolved at this coverage. This helps to identify the adsorption sites of Bi atoms. Individual Bi atoms are represented by the brighter dot-like motifs in the image. Bi atoms form pentagons of 0.95 ± 0.05 nm edge length. Some of them are highlighted in Fig.5.3(a). Small pentagons represent Bi atoms while the bigger (black and white) ones represent up and down pentagons of the clean surface. Bi pentagons have identical orientations, parallel to the orientation of the 'up' pentagons of the substrate. Most of the observed Bi pentagons at this coverage are incomplete. Fig.5.3(b) shows pentagonal motifs of in-plane structure of the clean surface in additional to two different adsorption sites marked with pink and red spheres. These sites will be explained later on.

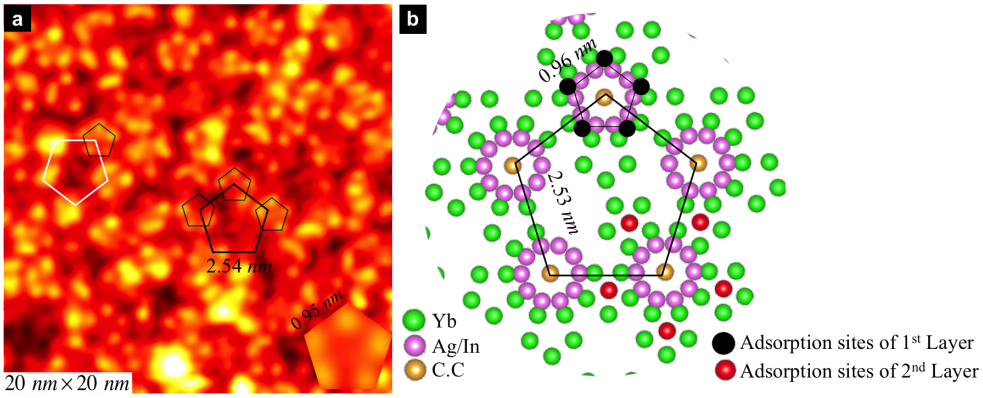

Figure 5.3: (a) 20 nm × 20 nm STM image after deposition of Bi for 5 minutes, showing incomplete Bi pentagons of 0.95 ± 0.05 nm edge length at the vertices of bigger pentagons of 2.50 nm edge length. (b) Pentagonal motif from in-plane structure with 2.53 nm edge length in addition to two different adsorption sites (black and red).

Upon further deposition of Bi, the development of the pentagons was observed. Fig.5.4(a) is an STM image of 20 nm × 20 nm, showing complete pentagons of Bi atoms. The surface area covered by Bi atoms at this dose is about 0.56 ML. The coverage is found by subtracting Bi atoms of first layer from the clean surface structure. In addition to complete Bi pentagons additional features were observed at this coverage including pentagonal stars of 0.60 nm edge length and crescent shape features as a result of additional adsorbed atoms in the pentagon edges. A large scale star and a crescent shape feature are shown in the bottom right inset in the Fig.5.4(a). Observed stars have two different orientations rotated by 36° with respect to each other and they are marked as black and white stars in Fig.5.4(b). The orientations of stars reflects the

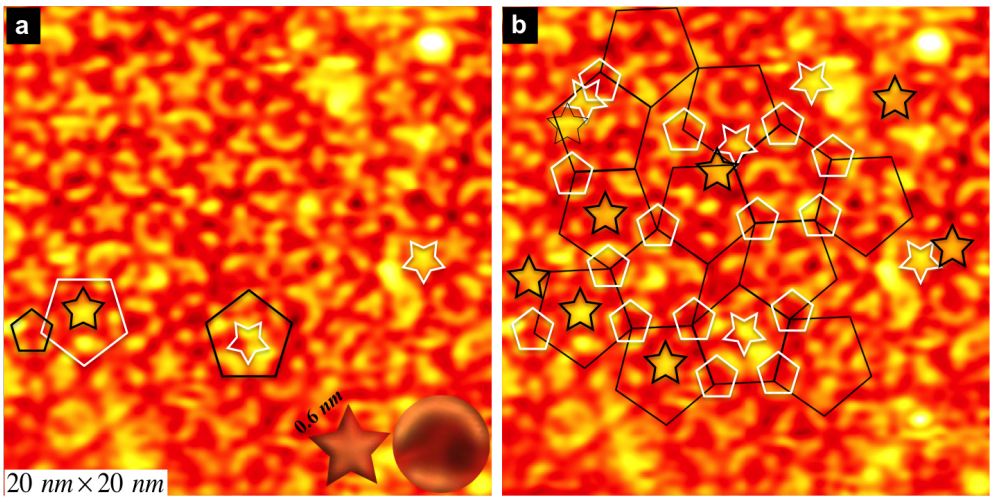

Figure 5.4: (a) 20 nm × 20 nm STM image after deposition of Bi for 12 minutes showing complete Bi pentagons in addition to pentagonal stars of 0.60 nm edge length and crescent shapes which formed by additional atoms at the edges of pentagons. (b) Same STM image as (a) with a patch of Penrose tiling of edge length 2.50 nm overlaid. Most of the pentagons and crescent shapes formed by Bi atoms (highlighted with white pentagons) are located at the vertices of the tiling.

orientations of 'up' and 'down' pentagons of the clean surface. The height of Bi atoms at this coverage is 0.12 ± 0.01 nm from the substrate.

For clarity, the STM image in Fig.5.4(a) is duplicated. The duplicated STM image with a patch of Penrose P1 tiling of 2.50 nm edge length overlaid is shown in Fig.5.4(b). It is obvious that most of the pentagons and crescent shapes formed by Bi atoms highlighted with white pentagons are located at the vertices of the tiling. The vertices of the tiling are where the cluster centres are located (protrusions of the clean surface). The location of Bi pentagons with respect to the tiling together with the location of Bi pentagons observed in the STM image of Fig.5.3(a) suggests that these Bi pentagons form on the top of the protrusions. From the size, orientation and location of the Bi pentagons adsorption sites are suggested to be between the Ag/In ring and the Yb ring. Five black spheres (Fig.5.3(b)) which form a pentagon of 0.96 nm edge length on the top of the protrusions of the clean surface illustrate these adsorption sites.

After depositing Bi for 50 minutes, STM images show Bi pentagons of different height and edge-length compared to pentagons found for previous coverages. Fig.5.5(a) shows an STM image 30 nm × 30 nm showing pentagons of Bi atoms with 1.54 ± 0.05 nm and 2.47 ± 0.04 nm edge-lengths. These pentagons are at a height of 0.25 ± 0.02 nm above the substrate, and therefore they can be considered as a second layer. The pentagons of the second layer are inflated by τ ($\tau = 1.618...$, an irrational number characteristic of quasicrystalline order.) and τ^2 with respect to first layer pentagons. These pentagons have two different orientations which are identical to the orientation of 'up'

and 'down' pentagonal protrusions of the substrate. The autocorrelation together with the FFT of the image, shown in Fig.5.6(a) and (b) respectively, show ten-fold symmetry which confirms the long-range quasicrystalline order of the film. The coverage of second layer Bi atoms is about 0.20 ML.

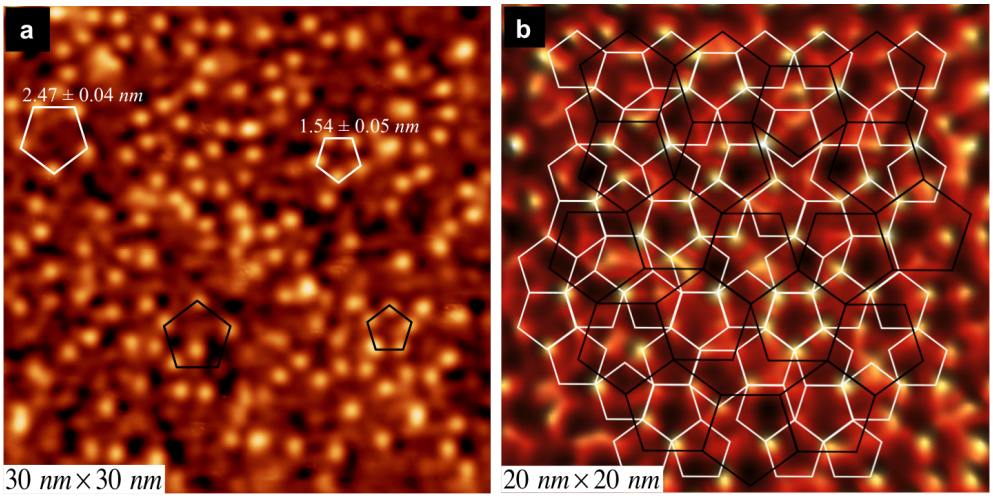

Figure 5.5: (a) 30 nm × 30 nm STM image after deposition of Bi for 50 minutes, showing pentagons inflated by τ and τ^2 compared to previous coverages. $\tau = 1.618...$, an irrational number characteristic of quasicrystalline order. (b) A 20 nm × 20 nm portion of the image (a) enhanced with FFT filtering and viewed in 3D with two Penrose P1 tilings overlaid marked with black and white tiles of 2.50 nm and 1.54 nm edge length respectively.

Fig.5.5(b) shows a portion of STM image of Fig.5.5(a) which is enhanced with FFT filtering. A patch of Penrose P1 tiling of edge-length 1.54 nm (white tiling) is mapped on the STM image Fig.5.5(b). It can be noticed that the Bi atoms are located at the vertices of the tiling. This confirms the long-range quasicrystalline order of the film. Another patch of Penrose P1 tiling of 2.50 nm edge length (black tiling) similar to the tiling superimposed to the surface structure model in Fig.5.2(b) is overlaid. It is obvious that most of the pentagons (white pentagons) of the second layer of Bi are located on the vertices of the black tiling where the substrate cluster centres are located. This indicates that the second layer pentagons are also formed on the top of the protrusions of the clean surface. However, protrusions belonging to the clean surface were not resolved in STM images at this coverage. From the size and orientations of observed second layer Bi pentagons and their location with respect to the tiling, the adsorption sites of the second layer can be identified as the centre of Yb pentagons around the cluster centre. Five red spheres (Fig.5.3(b)) forming a pentagon of 1.56 nm edge length on the top of the protrusions of the clean surface illustrate these adsorption sites.

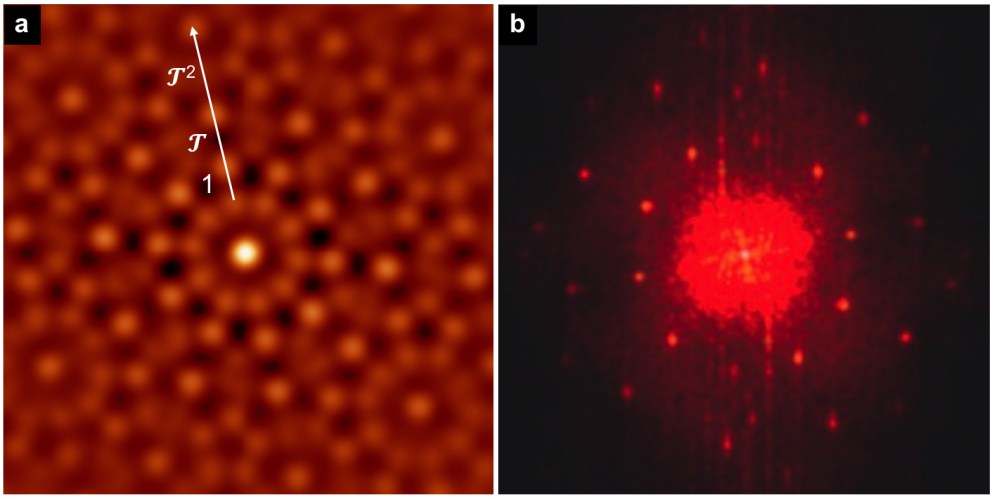

Figure 5.6: (a) The autocorrelation (b) FFT of the STM image in Fig.5.5(a), showing decagonal symmetry which confirms the long-range quasicrystalline order of the film.

Crystalline Bi Islands

Following the formation of the quasicrystalline layers, further deposition of Bi yields three dimensional islands atop the quasicrystalline film. The observed islands have rectangular symmetry. The structure of the islands could not be resolved by STM but the crystalline nature of the islands can be inferred from the rectangular edges of islands. Fig.5.7(a) is a 420 nm $\times$ 420 nm STM image displaying rectangular Bi islands. At these coverages Bi atoms seem to adsorb at the step edges which have higher coordination compared to the centre of the terraces, and thus adsorbed atoms formed islands at these sites. This can be clearly seen in Fig.5.7(a) which shows islands formed at the step edges. The observed rectangular Bi islands have different heights and orientations.

Different orientations of the islands are highlighted with different colours (yellow and white) in Fig.5.7(a). The orientation of islands can be explained by analysing the FFT of the STM images. The angles between the islands were found to be $2\pi/10$ which is consistent with the angle between high symmetry directions of the quasicrystalline Bi film. Fig.5.7(b) is the FFT of the image (a) showing double decagonal rings (tenfold symmetry) which result from the quasiperiodicity of the Bi film. The yellow and white arrows in the FFT image are the direction of Bi islands after rotation by 90°. Thus, the orientation of rectangular Bi islands appear to be parallel to high symmetry axes of the quasicrystalline film. This phenomenon was also observed when Bi deposited on five-fold surface and ten-fold surfaces of *i*-Al-Cu-Fe and *d*-Al-Co-Ni [145, 151] and the orientations of triangular Pb island edges were also found to be parallel to high high symmetry axes of the quasicrystalline film [152].

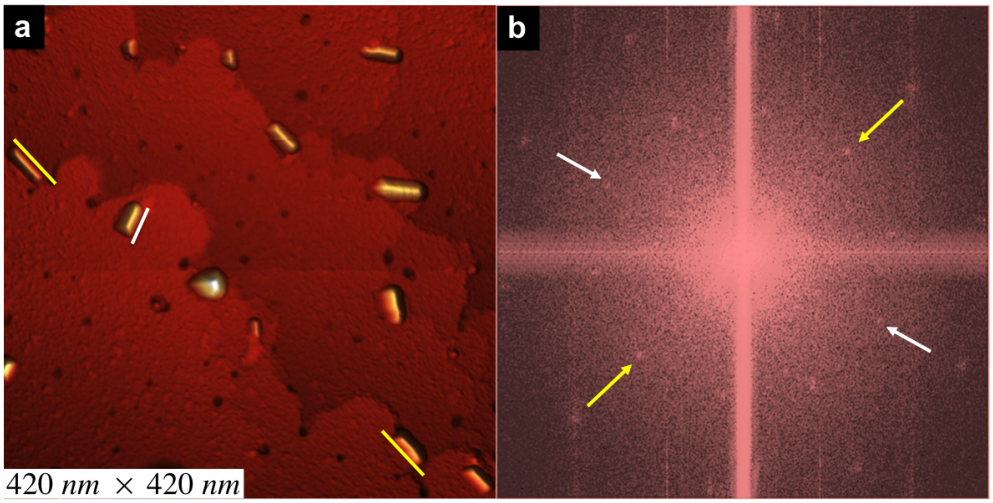

Figure 5.7: (a) 420 nm × 420 nm STM image after depositing Bi for 80 minutes, showing rectangular islands of different heights and orientations. (b) The FFT of image (a) showing decagonal rings which come from quasicrystalline structure underneath.

5.2.3 Discussion

To get further insight into the adsorption sites of Bi atoms, we looked at the structure of all atomic sites of the RTH cluster above the surface plane. For this purpose the structure of all planes (atomic sites) above the surface plane were considered separately. Fig.5.8(a) is the atomic density distribution of the i-Ag-In-Yb quasicrystal along the five-fold direction, showing different atomic planes (layers). Different colours (inset of Fig.5.8(a)) represent different atomic shells of the RTH clusters. Layer 1 represents the structure of the five-fold surface of the i-Ag-In-Yb quasicrystal which cuts the cluster centre of the RTH clusters. This structure is shown in Fig.5.2(b). After the structure of all atomic planes above the surface plane were tested, it was found that the structure of some of these planes correspond to the observed Bi positions in the STM images.

The structure of layer 4 in Fig.5.8(a) which is produced by Ag/In atoms of the fifth shell of the RTH cluster reproduces the structure of the first layer of Bi. To explain stars and crescent shapes observed in the STM image in Fig.5.4(a) an additional layer needs to be included which is the layer 3 just below the layer 4 in Fig.5.8(a). The structure of layer 3 and 4 together produces pentagons and stars (highlighted in Fig.5.8(c)) of 0.96 nm and 0.59 nm edge length respectively which are consistent with pentagons 0.95 ± 0.05 nm and stars 0.60 nm observed in the STM image of the first layer (Fig.5.4(a)). This structure is shown in Fig.5.8(c). The height of the first layer Bi atoms in the STM, 0.12 ± 0.01 nm, is also consistent with the separation between the surface layer 1 and the middle of layer 3 and 4 which is 0.14 nm. When this structure is superimposed to the surface layer it is found that the pentagons of layer 4 lie atop of the protrusions of the surface. This matches with the adsorption sites observed in the STM. Thus, the

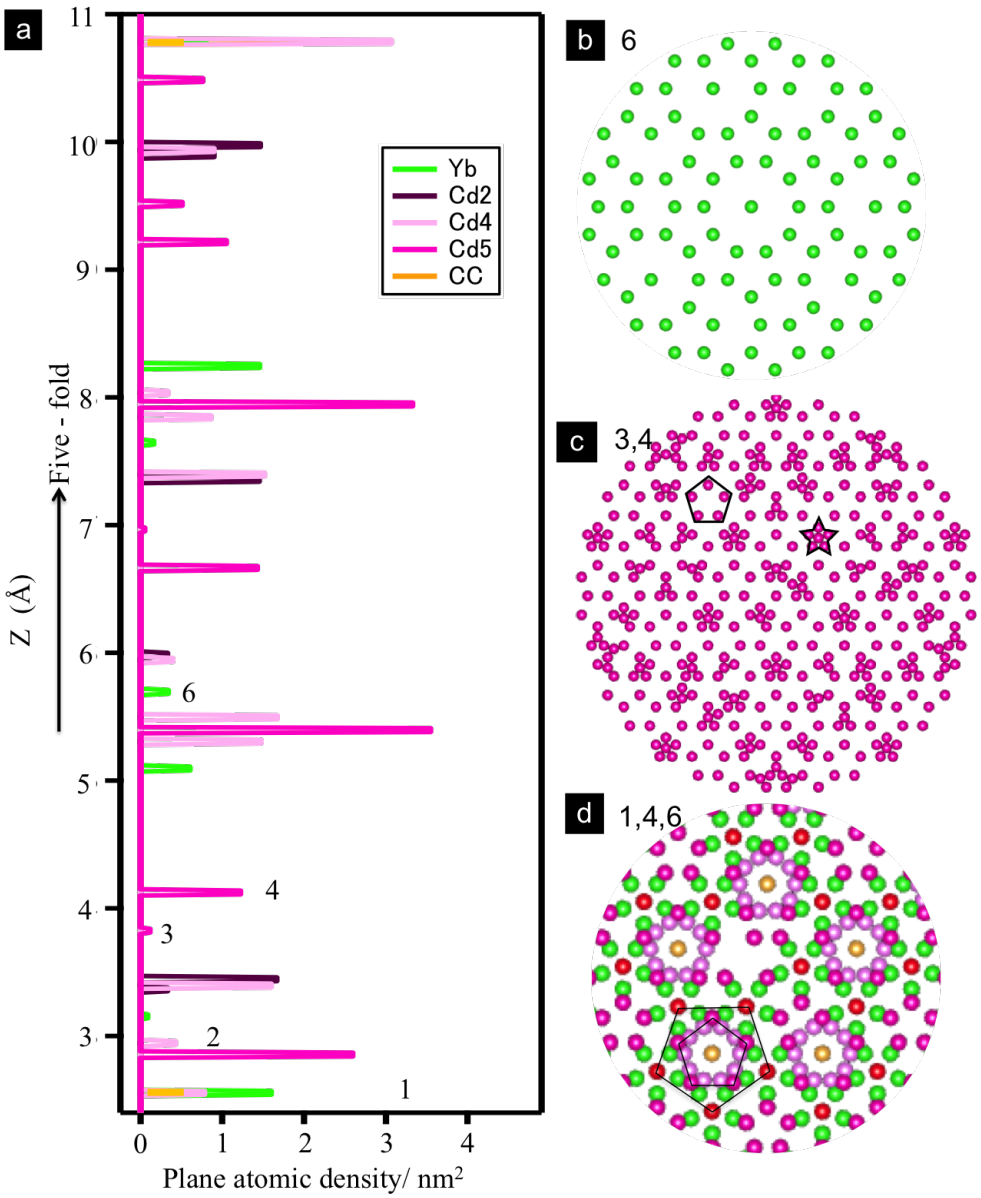

Figure 5.8: (a) Atomic density distribution of *i*-Ag-In-Yb quasicrystal along the five-fold direction. (b) The structure of atomic sites of layer 6 which is formed of Yb atoms (third shell of RTH cluster), which matches the structure of the second layer of Bi; the inset is the STM image of second layer with the structure of layer 6 is overlaid. (c) The structure of atomic layers 3 and 4 together which is made up of Ag/In atoms of the fifth shell of the RTH cluster. This structure corresponds to first layer of Bi. (d) The structure of layer 1, which is the surface, with the structure of layer 4 and 6 (first and second layer) superimposed. Here we have changed the colour of structure layer (6) from green to red so that they can be distinguished from green Yb atoms of the surface plane.

adsorption sites can be identified in-between Yb (green) and In (light pink) rings.

Resolving the second layer of Bi shows that Bi atoms occupy different adsorption

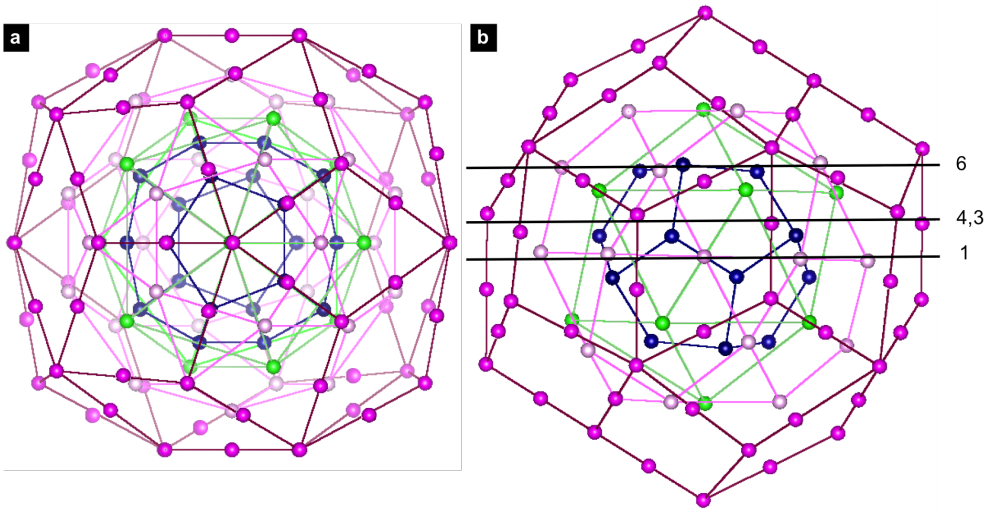

Figure 5.9: (a) RTH cluster shells (innermost (tetrahedron) is not shown) projected along five-fold (b) RTH cluster shells in (a) projected normal to five-fold showing surface plane which cuts the RTH centre (1) and two other planes (4,3) and (6) which represent atomic sites above the cluster centre.

sites once the adsorption sites of the first layer have been saturated. The adsorption sites of the second layer Bi atoms can be explained by layer 6 in Fig.5.8(a). The structure of layer 6, formed by Yb atoms of the third shell of RTH cluster, is shown in Fig.5.8(b). This structure contains pentagons of two different orientations (rotated by 36° with respect to each other) with 1.56 nm edge lengths which is almost the same structure observed for the second layer of Bi in STM. The height of Bi atoms in the STM 0.25 ± 0.02 nm is also in reasonable agreement with the separation of layer 6 from surface layer 1 which is 0.31 nm, although it is slightly lower which could be due to a small relaxation of the Bi atoms. The density of Bi atoms in the second layer in STM, which is calculated by counting the number of atoms in the STM images divided by the area of the images, is in between (0.18 - 0.20) atom/nm^2. This is also consistent with the number of adsorption sites in layer 6 (0.22 site/nm^2). Overlapping the structure of layer 6 with the surface layer 1 structure it was found that atoms of layer 6 occupy the centre of Yb pentagons of the surface surrounding the cluster centre as shown in Fig.5.8(d). Here the colour of atoms of layer 6 have changed from green to red so that they can be distinguished from Yb green atoms of the surface layer 1. Thus, the size and orientations of pentagons of layer 6 and those observed in STM suggest that the adsorption sites for second layer Bi atoms can be identified as the centre of Yb pentagons of the surface. Fig.5.9a and (b) are RTH cluster shells projected along and normal to the five-fold respectively. The surface plane (1) which cuts the RTH cluster at the centre and two other planes (3,4 and 6) which represent atomic sites above the surface for first and second layer Bi films are marked in Fig.5.9b. However, these planes

do not reproduce the same structure as planes in Fig.5.8(a) with a single cluster.

The observation of quasicrystalline Bi layers on the five-fold surface of the *i*-Ag-In-Yb quasicrystal is similar to what was recently observed for Pb on the same surface [147]. The first layer pentagons of Pb have almost the same size and orientation but they occupy different atomic sites of the RTH cluster (the atomic sites of the fourth icosadodecahedral shell, layer 2 in Fig.5.8(a)). In addition to pentagons in the first layer, pentagonal stars were observed in the centre of substrate protrusions for Bi (see Fig.5.4(b)). In contrast these stars were not observed for Pb. The second layer of Pb is also similar to second layer Bi and the atoms occupy similar sites. However, Pb atoms also occupy additional sites of the same shell (layer 5 in Fig.5.8(a)) which make decagonal rings; these rings were not observed for Bi. A third and an intermediate layers were also observed for Pb but not for Bi. The structure of different layers of Pb was shown in Fig.5.1. The difference between the structure of quasicrystalline Bi and Pb films could be due to different bonding of adsorbates with the substrate and interatomic distances of elements in the film.

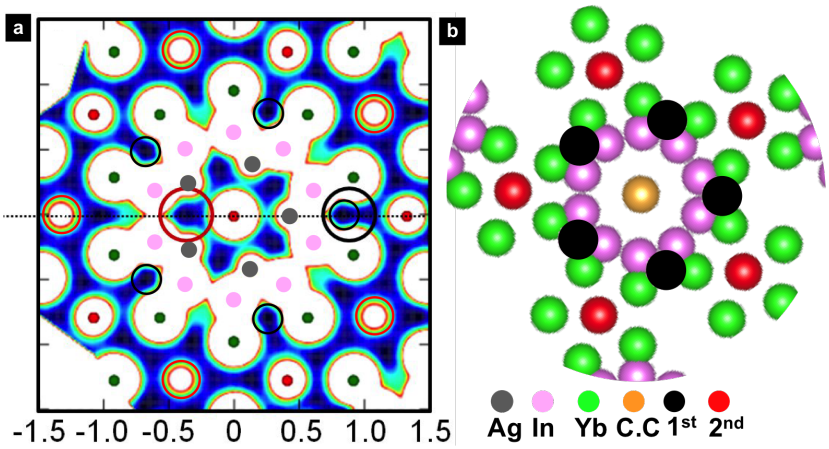

Figure 5.10: (a) Adsorption potential calculations for Bi for the clean five-fold surface of *i*-Ag-In-Yb quasicrystal. Reprinted from [153]. (b) Surface in-plane structure model showing a single cluster formed by Yb rings (green atoms) and In ring (pink atoms) around the cluster centre (yellow atoms) in addition to two different adsorption sites of RTH cluster above the surface (black and red atoms).

Preliminary density functional theory (DFT) calculations performed by our collaborator Nozawa from Graduate School of Materials Science - University of Hyogo - Hyogo - Japan support the formation of stable pseudomorphic Bi layers on the surface. Fig.5.10(a) depicts calculations of the adsorption potential for Bi on the clean five-fold surface of *i*-Ag-In-Yb quasicrystal [153]. Assuming only regions inside the decagonal Yb ring, there are two potential adsorption sites that make pentagons. These sites are marked with black and red circles. Black circles are located between Yb rings (green atoms) and the In ring (light pink atoms), yield a pentagon whose edge-length is con-

sistent with the pentagons of first layer Bi observed in the STM images. Red circles are located in the centre of the Yb pentagons and make a larger pentagon (τ scaled to black circle pentagon) of edge length consistent with second layer Bi pentagons in the STM images.

The DFT calculations support the conclusion that Bi atoms occupy the atomic sites of the RTH cluster above the surface. This can be seen in the comparison image in Fig.5.10. For comparison only a single cluster from Fig.5.8(d) is taken. This cluster is formed by Yb ring (green atoms), and an In ring (light pink atoms) around the cluster centre (yellow atom), is shown in Fig.5.10(b). Two different adsorption sites (marked with black and red) which are formed by atomic sites of the RTH cluster above the surface are also presented in Fig.5.10(b). It can be seen that the adsorption sites identified by DFT calculations are similar to the adsorption sites formed by atomic sites of the RTH cluster above the surface.

Observation of quasicrystalline layers of Bi on the fivefold surface of the i-Ag-In-Yb quasicrystal which is the Yb rich surface [16], is expected from the strong bonding between Bi and Yb as characterised by the high melting temperature of intermetallic compounds of these elements [154]. Achieving more than a single layer of Bi quasicrystalline structure on the surface of the i-Ag-In-Yb quasicrystal (being different structurally and chemically from Al-based quasicrystals), indicates that the chemistry and structure of the substrate also play a role in achieving a quasicrystalline film. As mentioned earlier Bi formed only a pseudomorphic monolayer on Al-based quasicrystals. This explains that the quasiperiodicty of the surface is not the only factor that impacts the structure of the film but chemical composition and structure of the surface are also important in thin film formation.

5.3 Conclusions

The five-fold surface of i-Ag-In-Yb quasicrystal has successfully been used as a substrate to grow a quasicrystalline thin film of a single metallic element (Bi). Scanning tunnelling microscopy (STM) was employed to characterise the surface structure and the thin film formation. In contrast to Al-based quasicrystal surfaces, more than a single layer quasicrystalline of Bi film was successfully grown on the surface. Thus in parallel to the symmetry, the chemistry and structure of the substrate seem to play a role in achieving the quasicrystalline film. The quasiperiodicty of the film is confirmed through the FFT, autocorrelation of the STM images and through the Penrose tiling. The adsorption sites of Bi adsorbate were found to be the atomic sites of the RTH cluster above the surface; thus the film is formed in layers of different heights above the substrate. Following the formation of the quasicrystalline film, crystalline Bi islands were observed which are aligned to the quasicrystalline high symmetry axes of the film underneath. The growth mode of the film formation can be identified as Stranski-Krastanov mode.

Chapter 6

The Growth of In on the five-fold Surface of the *i*-Ag-In-Yb Quasicrystal

6.1 Introduction

Indium growth on Al-based quasicrystal surface has been studied previously [9]. The deposition of In on the five-fold and ten-fold surfaces of the *i*-Al-Pd-Mn and *d*-Al-Ni-Co quasicrystals was studied using X-ray photoelectron spectroscopy (XPS), reflection high energy electron diffraction (RHEED) and scanning tunneling microscopy (STM). Indium did not show any order on these surfaces. However, when used as a surfactant on the *d*-Al-Ni-Co surface and deposition of Au leads to the formation of a crystalline multilayer [155, 156, 157].

This chapter provides the details of a first study of quasicrystalline In growth on the five-fold surface of the *i*-Ag-In-Yb quasicrystal. Scanning tunneling microscopy (STM) and low energy electron diffraction (LEED) have been employed to characterise the surface and In thin film formation.

6.2 Experimental Details

This work is done in a collaboration with the Jean Lamour Institute, Nancy, France. The experiments were conducted in both centres (Surface Science Research Centre, Liverpool, UK and Jean Lamour Institute, Nancy, France). The sample preparation methods were as described in the experimental part of the previous chapter. The STM results obtained were similar. The data presented in this chapter were those collected in Nancy.

6.3 STM and LEED Results

Fig.6.1(a) shows a 250 nm × 250 nm STM image following 30 minutes deposition of In on the five-fold surface of the *i*-Ag-In-Yb quasicrystal. STM images revealed terraces of two different structures as can be seen in Fig.6.1(a).

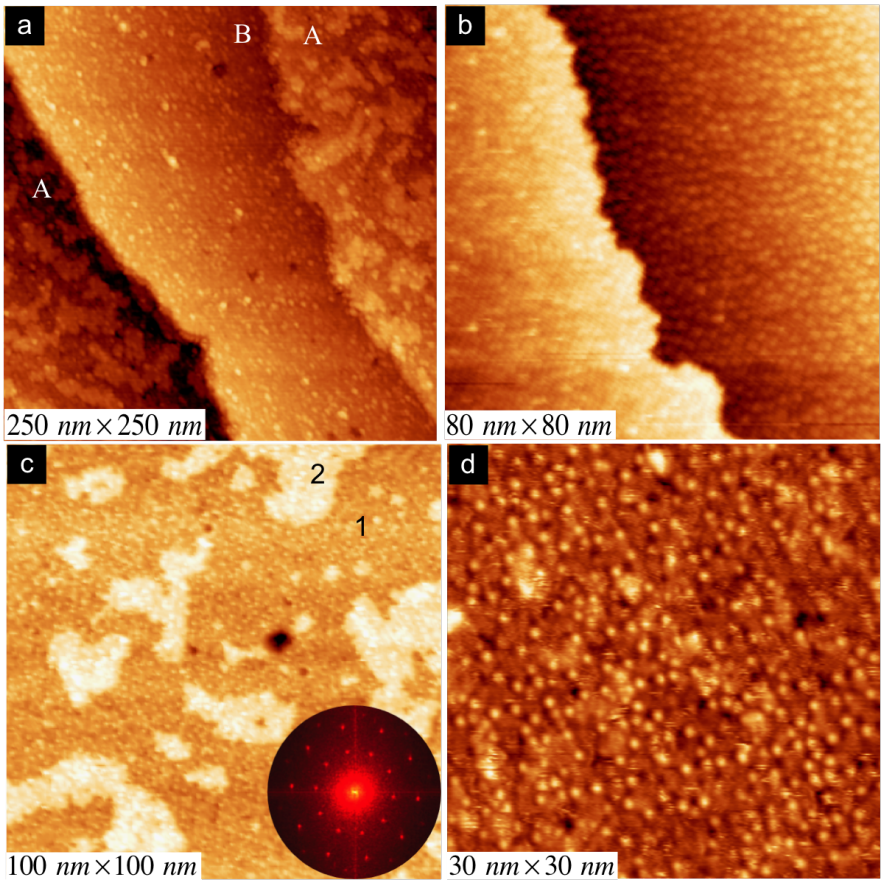

Figure 6.1: (a) 250 nm × 250 nm STM image of 30 minutes In deposition on the five-fold surface of *i*-Ag-In-Yb quasicrystal. The image shows different terraces with different structure. (b) 80 nm × 80 nm STM image of the clean five-fold surface of the *i*-Ag-In-Yb quasicrystal. (c) 100 nm × 100 nm STM image of 30 minutes deposition of In, showing the structure of terrace A. The structure reveals a quasicrystalline structure (1) and islands (2). (d) 30 nm × 30 nm STM image of the quasicrystalline In structure

The terraces of different structure are labelled with A and B. This is most likely to be due to the fact that terraces of the clean surface are not identical in terms of chemistry and atomic density. Fig.6.1(b) shows an example of two different terraces of the clean surface. The FFT of both terraces shows ten-fold symmetry. Pentagonal protrusions were resolved on the right terrace in Fig.6.1(b) whereas the structure of the left terrace Fig.6.1(b) is unresolved. This is could be due to the chemistry and atomic density of the bulk planes which describe the terraces. For example the plane 1 in Fig.6.5(e) is Yb rich ($Ag_8In_{34}Yb_{58}$) and the atomic density is 1.95 atom/nm^2 but the chemistry and

atomic density of plane 2 are $Ag_{16}In_{63}Yb_{21}$ and 3.13 atom/nm^2 respectively. Terrace dependent film morphology was also observed when Sn [139], Al [140] and Bi [158] were deposited on the five-fold surface of the *i*-$Al_{63}Cu_{24}Fe_{13}$ quasicrystal.

The structure of terrace A is shown in Fig.6.1(c). This structure showed a quasicrystalline structure (1) and island-like features (2). These are marked with number 1 and 2 respectively. Terrace B of Fig.6.1(a) shows no features and the FFT does not show any order. To understand the quasicrystalline structure in-between islands in Fig.6.1(c) , STM images of this region were collected. A clear quasicrystalline structure was resolved: Fig.6.1(d) shows a 30 nm $\times$ 30 nm STM image of this quasicrystalline structure.

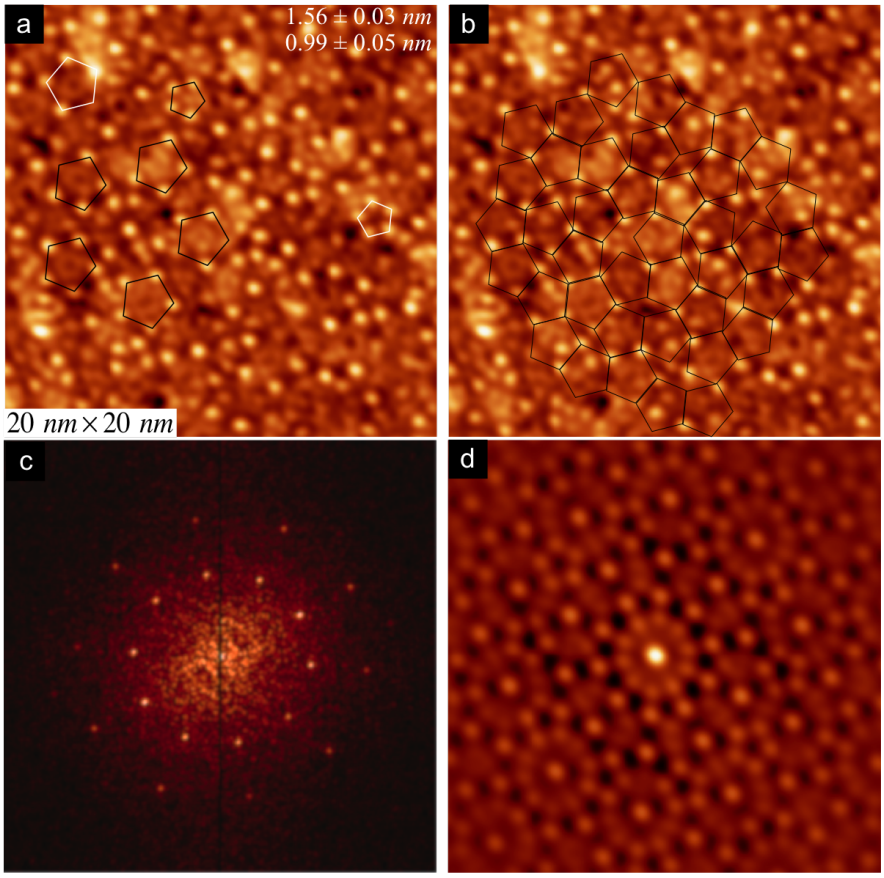

Figure 6.2: (a) 20 nm $\times$ 20 nm STM image of the structure between islands, showing In atoms forming pentagons of two different sizes (0.99 $\pm$ 0.05 nm and 1.56 $\pm$ 0.03 nm) which are related by τ. (b) The same STM image of (a) with a patch of Penrose P1 tiling overlaid. Most of the In atoms located at the vertices of the tiling. (c) The FFT of the STM image. (d) The autocorrelation of the STM image. Both the FFT and the autocorrelation show tenfold symmetry which confirms the quasiperiodicity of the structure.

To analyse the quasicrystalline structure, a portion of STM image of Fig.6.1(d) was chosen as shown in Fig.6.2(a). The bright features correspond to In atoms. Pentagons

of two different sizes and orientations were formed by In atoms. The edge length of small and larger pentagons was found to be 0.99 ± 0.05 nm and 1.56 ± 0.03 nm respectively. The larger pentagons are inflated by τ compared to the smaller ones. The orientations of larger In pentagons are identical to the orientations of substrate protrusions as they are rotated by 36° to each other and dubbed as 'up' and 'down' pentagons. These pentagons are highlighted with black and white in Fig.6.2(a). The height of In atoms from the substrate is 0.10 ± 0.01 nm. This is can be considered as a first In quasicrystalline layer. Protrusions belonging to the substrate were also resolved in this image. These protrusions are located inside the larger (1.56 ± 0.03 nm edge length) In pentagons (see larger pentagons in Fig.6.2(a)). This helps to identify the adsorption sites of In atoms.

A patch of Penrose P1 tiling with 1.56 nm edge length is overlaid on the same STM image as shown in Fig.6.2(b). It is found that most of the In atoms which form the larger pentagons are found at the vertices of the tiling. This confirms the long range quasicrystalline order of the In film. The quasiperiodicity of the structure is also confirmed by the FFT and autocorrelation of the STM image which are shown in Fig.6.2(c) and (d) respectively. The islands in Fig.6.1(c) are at 0.25 ± 0.02 nm from the substrate. Thus they can be considered as a second layer of In. However, no atomic resolution was found on the islands at this coverage.

On further deposition the development of the islands was observed. Islands grew laterally and a quasicrystalline structure was observed on the islands. Fig.6.3(a) shows a 80 nm × 80 nm STM image after In deposition for 36 minutes. A quasicrystalline structure was resolved on the island as shown in Fig.6.3(b). Similar to the first layer, In atoms at this coverage form pentagons of two different sizes and orientations. The sizes of larger and smaller pentagons were almost the same as those of the first layer. Black and red pentagons refer to different orientations. Most of the In pentagons here are incomplete. Although the atomic resolution obtained from the structure of the islands is not very clear, the autocorrelation and the FFT of images of the structure show long range quasicrystalline order. The autocorrelation and the FFT are shown in Fig.6.3(c) and (d) respectively. The FFT is a mathematical tool used for converting a function of time into a function of frequency which is useful to analyse time dependant phenomena and autocorrelation is also a mathematical tool which measures the correlation of a function of time with itself shifted by a time delay. It is used to find the repeating patterns. The In atoms here are at height of 0.31 ± 0.01 nm from the first layer, so this structure can be considered as a third layer of a quasicrystalline In film. At this coverage additional islands (white features in Fig.6.3(b)) were resolved. These islands are at 0.20 ± 0.02 nm from the third layer. These islands are not large enough to understand the structure. However, the surface appears to be flat. This might produce another crystalline or quasicrystalline In layer upon further deposition. However the

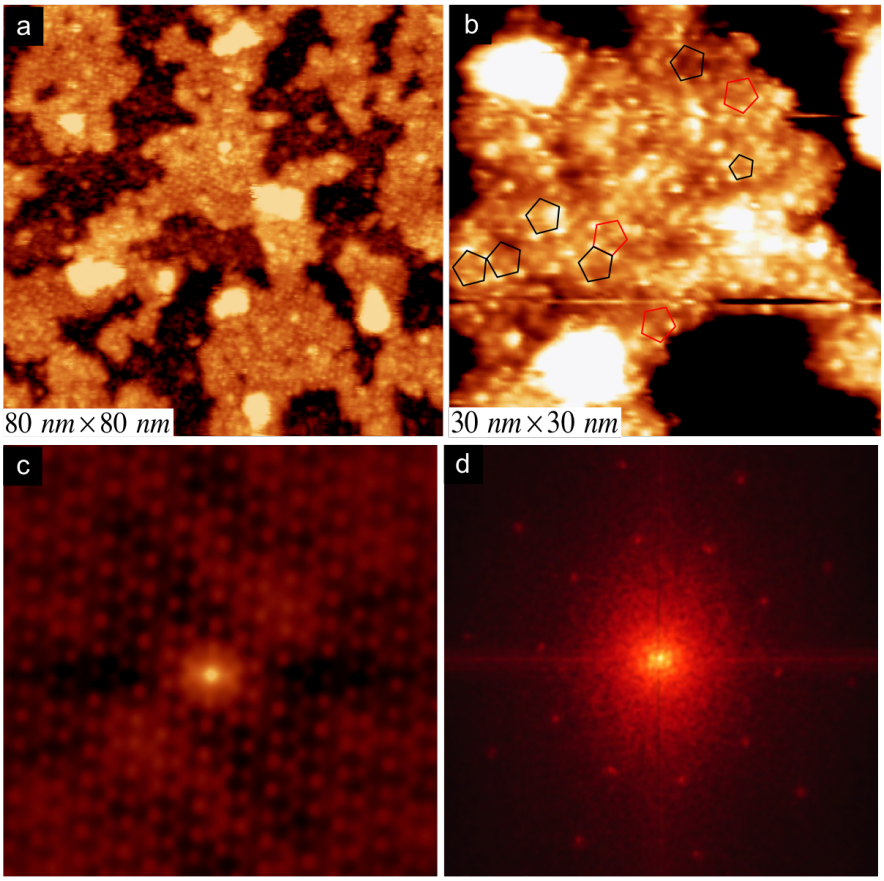

Figure 6.3: (a) 80 nm × 80 nm STM image after 36 minutes deposition of In on the five-fold surface of *i*-Ag-In-Yb quasicrystal. (b) 30 nm × 30 nm STM image at the same coverage, showing the structure on the islands. (c) Autocorrelation of the STM image of (b), showing tenfold symmetry which confirms the quasiperiodicity of the structure. (d) The FFT of the STM image of (b), showing tenfold symmetry.

data for higher coverages are not available at this time.

The LEED pattern was collected after deposition of In for 36 minutes. At this coverage tenfold symmetry was observed as a sign of a quasicrystalline In film. However, the LEED patterns were not sharp, which might be due to the existence of the islands. The LEED pattern (18 eV) is shown in Fig.6.4(a). The film was then briefly annealed for 15 minutes at 290 °C. The annealed film showed a sharp LEED pattern (see Fig.6.4(b)). This could be due to diffusion and coalescence of In islands on the surface.

6.4 Discussion

Similar to the Bi analysis in the previous chapter, the quasicrystalline In film may be understood in terms of adsorption at RTH atomic sites above the surface. The structure of atomic planes (layers) above the surface plane (layer) was considered separately. The atomic density distribution of the *i*-Ag-In-Yb quasicrystal along the five-fold axis

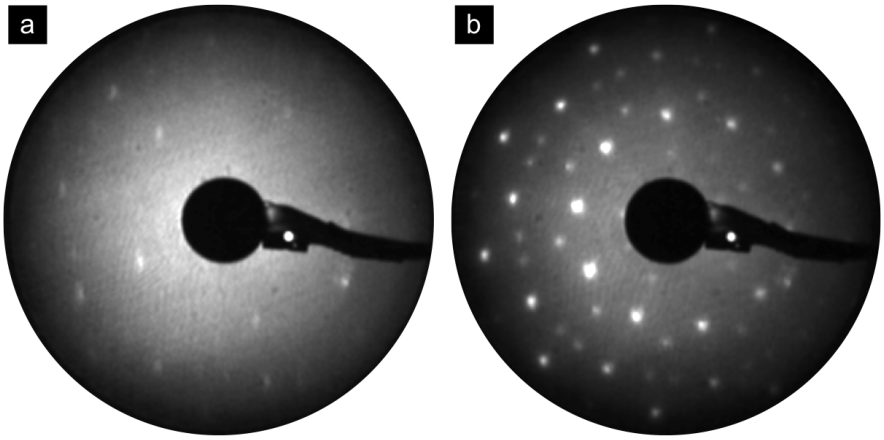

Figure 6.4: (a) LEED pattern (18 eV) of In deposition after 36 minutes on the five-fold surface of *i*-Ag-In-Yb quasicrystal. film (b) LEED pattern (18 eV) after annealing the film for 15 minutes at 290 °C

is shown in Fig.6.5(e). The surface planes which cut the RTH cluster centres are highlighted with 1, 2, 3 and 4 in Fig.6.5(e). To determine the structure of a plane that can explain the quasicrystalline film observed in STM, many planes were tested.

This was done by comparing the STM data with the structure of the atomic sites. The STM image of the quasicrystalline In film shown in Fig.6.5(a) is the same image as Fig.6.2(a). The In atoms make pentagons of 1.56 ± 0.03 nm around protrusions of substrate. The protrusions of the substrate observed in the image make pentagons of 2.48 ± 0.04 nm and 4.10 ± 0.07 nm edge length which are related to each other by the factor τ. These pentagons are highlighted by blue pentagons in the image. This is in good agreement with the structure of the surface plane 1. This structure is shown in Fig.6.5(b) with pentagons of 2.53 nm and 4.10 nm edge length highlighted.

The in-plane structure of layer 1a which is formed by Ag/In atoms of the fifth shell of RTH cluster is shown in Fig6.5(c). The atomic sites of this layer make pentagons of two different sizes and orientations. The small and large pentagon edge-lengths are 0.967 nm and 1.565 nm respectively. This is consistent with the observed pentagons (0.99 ± 0.05 nm and 1.56 ± 0.03 nm) of the first quasicrystalline In layer in STM (Fig6.5(a)). Layer 1a is at 0.096 nm above the surface of plane 1 which is also consistent with the height of In atoms (0.10 ± 0.01 nm) of the first quasicrystalline In layer from the surface. Moreover, the density of In atoms 0.40 ± 0.05 atom/nm^2 of the first layer in STM is comparable to the density of atomic sites 0.56 atom/nm^2 of layer 1a. This structure is overlaid on the surface plane 1 structure and shown in Fig6.5(d). It is found that pentagons of 1.565 nm formed by Ag/In atoms of layer 1a lie around the cluster centres in-between Yb pentagons. Therefore these sites can be identified as the adsorption sites for In atoms in the first layer.

Regarding the second layer, because of lack of atomic resolution, it is difficult to

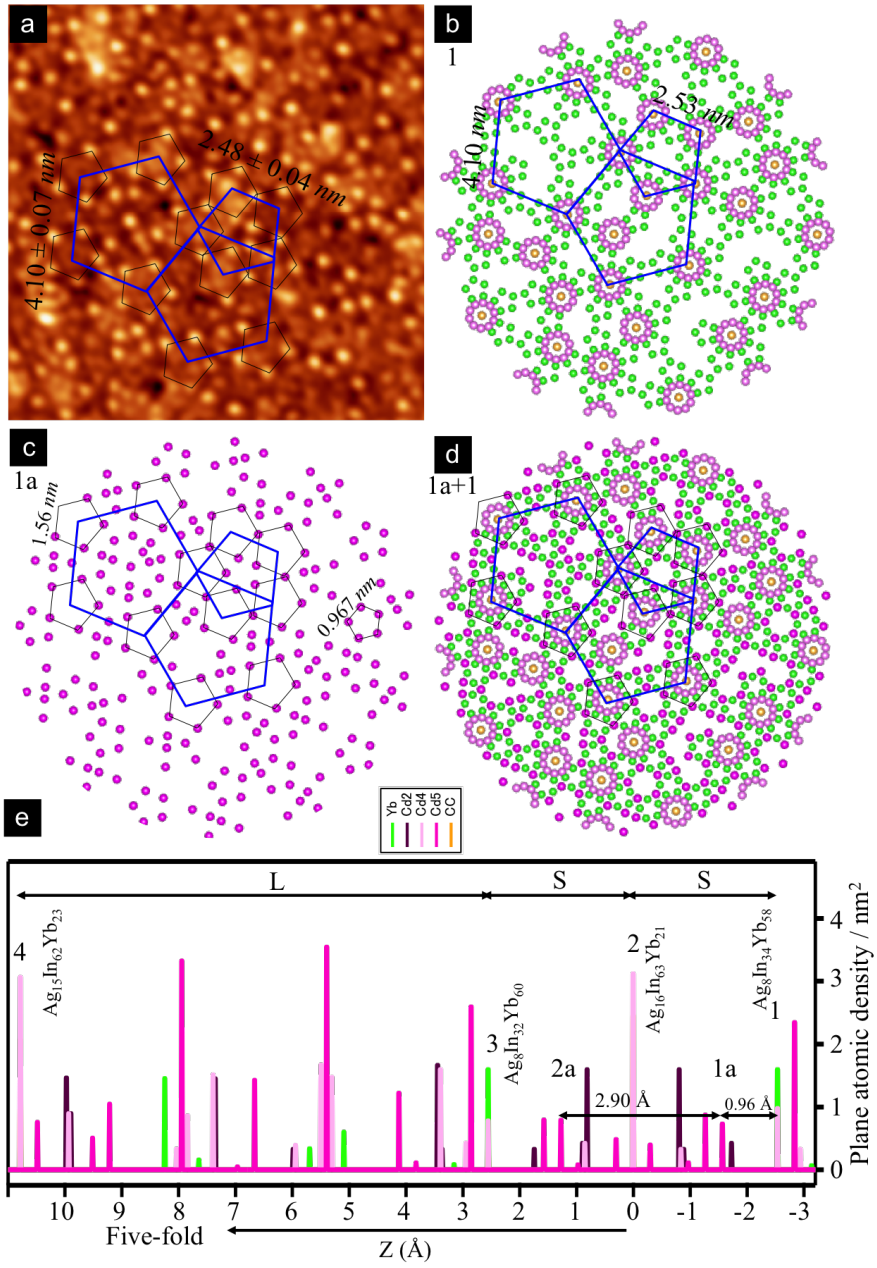

Figure 6.5: (a) 20 nm × 20 nm STM image of quasicrystalline In film. (b) The in-plane structure of layer 1(surface plane). (c) The in-plane structure of layer 1a, which matches the In quasicrystalline film. (d) The structure of layer 1a is superimposed on the structure of layer 1 (surface plane). (e) The atomic density distribution of the *i*-Ag-In-Yb quasicrystal along the five-fold axis.

assign the structure to any layer. However its height of 0.25 ± 0.02 nm from the substrate matches the separation of surface layer 1 and layer 2 which is 0.25 nm. So the second layer could be formed by atoms of layer 2. The lack of atomic resolution in this layer could be due to electronically coupling of In atoms as the density of In is very high compared to other species $Ag_{16}In_{63}Yb_{21}$ in layer 2 and additional In was

deposited.

In the third layer due to low density of In atoms and lack of relation between In atoms and substrate protrusions, the comparison of the structure of the third quasicrystalline In layer with the structure of atomic sites of RTH cluster above the surface is not straight-forward. However, its structure is similar to the structure of the first layer and the structure of layer 2a produces the same structure as layer 1a (which explains the first layer) so it is reasonable to consider that the third layer In atoms occupy the atomic sites of layer 2a. Moreover the height of the third layer from the first layer (0.31 $\pm$ 0.01 nm) in STM also matches the separation between layer 2a and 1a (0.29 nm). The relation between third layer pentagons and first layer pentagons or substrate protrusions was not observed in the STM, so it was not possible to identify the adsorption sites of third layer In atoms in terms of first layer or substrate protrusions. However, as the structure of layer 2a is the same as 1a, and when 2a is superimposed to the surface plane 1, it is found that the atomic sites of layer 2a occupy the same sites in the surface plane as 1a (Fig.6.5(e)). These sites are in-between Yb pentagons of the surface plane. Both first and third quasicrystalline layers are formed on the small (S) terraces in the experiment. This confirms that In atoms occupy atomic sites of layer 1a and 2a as they belong to S planes in the model structure (Fig.6.5(e)).

Table 6.1: Comparison between growth of metallic (Pb, Bi and In) films on the five-fold surface of the *i*-Ag-In-Yb quasicrystal in terms of occupying atomic sites of different shells of the RTH cluster.

Species	1^{st} Layer	2^{nd} Layer	3^{rd} Layer
Pb	fourth shell $Ag_{0.2}In_{0.8}$	third shell Yb	third shell Yb
Bi	fifth shell $Ag_{0.5}In_{0.5}$	third shell Yb	- -
In	fifth shell, $Ag_{0.5}In_{0.5}$	fourth shell $Ag_{0.2}In_{0.8}$	fifth shell $Ag_{0.5}In_{0.5}$

In summary, similar to other metallic elements Pb and Bi, In forms quasicrystalline layers on the five-fold surface of the *i*-Ag-In-Yb quasicrystal. The In atoms similarly occupy the atomic sites of the RTH cluster above the surface. However, the adsorption sites are different. This could be due to the different bonding between substrate and adsorbate or could be due to the different atomic size of these elements. The RTH cluster shells and the chemistry of the planes which describe the quasicrystalline layers of various species are shown in Table 6.1. It can be seen that third shell atomic Yb sites are occupied by Pb and Bi atoms as expected from the strong interaction between Pb and Yb [159] and Bi and Yb [154], whereas In atoms only occupy atomic sites of shells which contains In. To get further insight into adsorption sites density functional

theory (DFT) calculations are required.

The associated growth mode for all quasicrystalline films observed can be identified as the Stranski-Krastanov type. To understand the nature of islands and layer formation, further experiments are required including different techniques such as X-ray photoelectron spectroscopy (XPS) which probes chemical bonding.

The observation of In quasicrystalline structure on this surface is in contrast to Al-based quasicrystals where no order was observed. The chemistry of the five-fold surface of the *i*-Ag-In-Yb quasicrystal seems to play a role in obtaining In quasicrystalline structure as the surface itself is In-rich. This indicates that different structures of films of the same adsorbed element results from the different structure and chemical composition of the substrate.

6.5 Conclusions

The first study of In growth on a non-Al-based quasicrystal surface is presented. The five-fold surface of *i*-Ag-In-Yb quasicrystal was used as a substrate to grow the film. Scanning tunneling microscopy (STM) and low energy electron diffraction (LEED) were used to characterise the film. A quasicrystalline single element film of In was achieved through deposition of In on the surface. The qausiperiodicity of the film was confirmed by the autocorrelation and the FFT of images of the film. Comparing the structure of the film with the structure of atomic sites of the RTH cluster above the surface, it was found that the adsorbate atoms occupy the atomic sites of the RTH cluster above the surface. Thus the film grows in layers. Following the formation of the quasicrystalline In film, In islands atop the quasicrystalline layer were observed. To conclude, unlike Al-based quasicrystal surfaces the five-fold surface of the *i*-Ag-In-Yb quasicrystal could be used as a template for In single element quasicrystal thin film. In parallel to the symmetry of the surface, the chemistry of the surface seems to play a role in this mission.

Chapter 7

Summary and Conclusions

The discovery of the *i*-Cd-Yb quasicrystal provided a new non-Al-based quasicrystal. The *i*-Ag-In-Yb quasicrystal was formed after replacing Cd with equal amounts of Ag and In. This new quasicrystal has been used to understand the surface structure of the binary quasicrystal family as the parent quasicrystal can not be treated under UHV conditions for surface studies due to presence of Cd. In addition to quasicrystalline phase, two crystalline phases were also found in this system, Ag-In-Yb 1/1 and 2/1 approximants. Replacing Yb with other rare earth elements yields other new approximants such as Ag-In-Tb and Ag-In-Gd.

One of the main goals of the work of this thesis was to study the surface structure of Ag-In-RE 1/1 approximants where RE = Tb, Gd and Yb. The bulk structure of these approximants is formed by the same (RTH) clusters as their parent icosahedral Ag-In-Yb quasicrystal. However, in approximants the RTH clusters are packed periodically. The surfaces (two-fold, three-fold and five-fold) of the icosahedral Ag-In-Yb quasicrystal had been studied using STM and LEED. It was found the surfaces are bulk terminated and they form at the bulk planes which intersect the RTH cluster centre. So the surface structural study of approximants will help to find out how these surfaces are related to the surface of the quasicrystals of the same system in terms of bulk termination.

In this thesis the surface of Ag-In-RE 1/1 (RE = Tb, Gd and Yb) approximants were studied. Using normal sputter-annealing cycles, the surfaces revealed the step/terrace morphology. The surface preparation conditions were found to be similar to those used for the *i*-Ag-In-Yb quasicrystal surfaces. STM images of the surface of Ag-In-Tb and Ag-In-Gd approximants showed facets along different crystallographic directions whereas the Ag-In-Yb surface did not show any facets. The observed facets most likely developed during mechanical polishing due to the small size of the samples. After macroscopic orientation of the surface were checked by Laue back scattering, it is found that the surface of the Ag-In-Gd approximant is tilted by 10° from [001] and 4° from [010] and respective angles for the Ag-In-Tb are found to be 11° from [001] and 7° from [010]. STM images of the facets revealed the step/terrace structure. The observed

step heights of facets are in agreement with the expected periodicity of the facets. High resolution STM images of the facets showed protrusions; however the atomic resolutions are rarely resolved in the (310) and (501) facets. Comparing the high resolution STM images and step heights to the bulk structure model, terraces were found to be formed in the bulk planes.

The observation of facets was found to be consistent with the density of lattice points. Atoms of the surface of the facets were found to be bonded with other atoms below the surface. The Tb and In species were often involved in the bonding which stabilises the surfaces. This is consistent with the surface of quasicrystals which they were rich in Yb and In. To summarise this work, the surface of approximants were found to be bulk terminated and form around the bulk plane which cuts the RTH cluster centre. Since the structure of these surfaces are known, they can be used as substrates to grow metallic and molecular films.

The other goal was to achieve artificial single element quasicrystals through deposition on non Al-based quasicrystals. In this thesis, the five-fold i-Ag-In-Yb quasicrystal surface, which is structurally and chemically different from Al-based quasicrystals, was used as a substrate to grow Bi and In thin films. In contrast to the deposition of these elements on Al-based quasicrystal surfaces, layers of quasicrystalline structure of Bi and In were observed on the surface. This shows that the structure and the chemistry of the substrate has an impact on the thin film formation. The quasiperiodicty of the film in both cases was confirmed through the FFT and autocorrelation of images of the film. Comparison of high resolution STM images of the film with the structure of bulk planes above the surface showed that adsorbates occupy specific atomic sites of the RTH cluster above the surface. Further deposition led to three-dimensional crystalline islands of Bi. The islands were not large enough to allow determination of their structure but the crystalline nature of the islands were indicated by rectangular shape of the islands. The analysis of the FFT of the image showed that these islands are orientationally aligned with the quasicrystalline film underneath. The growth mode of both thin films was found to be the Stranski-Krastanov mode as the thin film formation changed from two-dimensional to three-dimensional fashion.

Appendix A

Pumps, Gauges and Mass Spectrometer

A.1 Pumps

A.1.1 Rotary Vane Pump

The rotary vane pump is one of the most widespread pumps in UHV systems as a primary and as roughing pump. It pumps the system from atmospheric pressure to a pressure of about 10^{-3} Torr. A schematic illustration of the cross section of a rotary vane pump is displayed in Fig.A.1. The rotary vane pump is made of a rotor which rotates inside a cylindrical housing called stator. The rotor has vanes which are compressed against the walls of the stator due to a spring attached in the middle of vanes or centrifugal force. As the vanes slides, a chamber will be created in the inlet side and gases enter this chamber. These gases will be compressed upon further rotation of the rotor and finally they will be expelled through the exhaust valve into the atmosphere. Most pumps are provided with a gas ballast valve (gas load valve). A certain amount of air goes through this valve into the compressed gas chamber to prevent the compressed gas from condensing. A seal between the vanes and stator can be maintained using the oil charge of the rotary vane pump which also serves for lubrication and cooling [91, 92, 93, 160].

A.1.2 Turbomolecular Pump

This pump which operates in the molecular flow regime can pump the system from 10^{-3} mbar down to 10^{-10} mbar so must be exhausted to a backing pump (rotary vane pump). A turbomolecular pump consists of a stack of rotors with canted blades which rotate at very high speed (around 90,000 rpm). Gas molecules receive a high velocity in the direction of high pressure exhaust when they hit the canted blades. Stator blades which canted in the opposite direction to the rotor, are interleaved between rotors. Stator blades reduce the gas molecules velocity and compress them. Thus gas molecules will

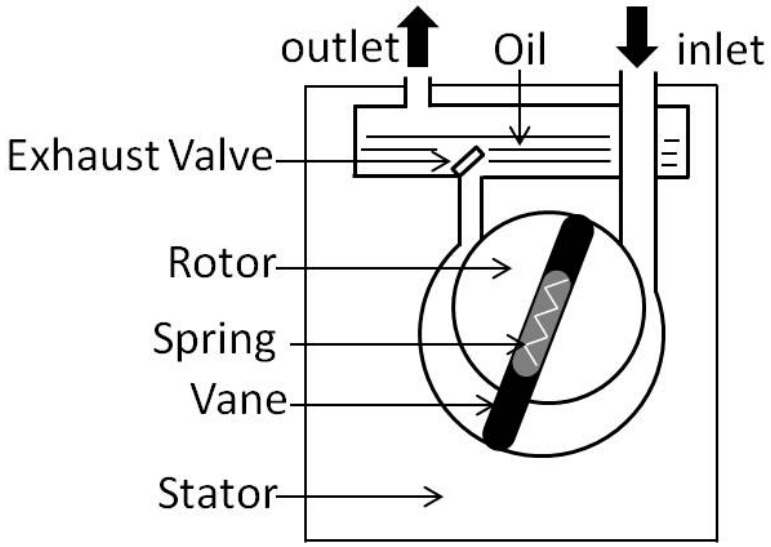

Figure A.1: A schematic illustration of the operation of a rotary vane pump.

be swept away from the UHV into the backing pump and hence into the atmosphere. A schematic diagram of turbomolecular pump is shown in Fig.A.2

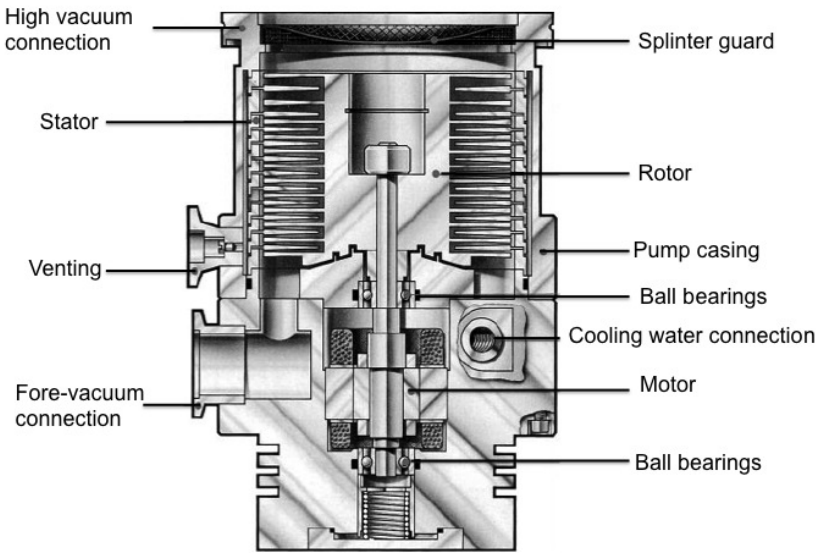

Figure A.2: Schematic diagram of a turbomolecular pump. Reprinted from [87].

The compression ratio between UHV and the backing side depends on the velocity of the rotor and molecular weight of the gas molecules (logarithm of compression ratio is proportional to the square root of molecular weight). So the compression ratio is better for heavier gases, for example about 10^8 for N_2 and only about 10^2 for H_2 see Fig.A.3. The main advantage of turbomolecular pump is the production of a very clean vacuum (oil free). However, it is very slow for pumping light gases and it is vibrationally noisy

for performing a surface analysis experiment such as STM [86, 92, 93, 160].

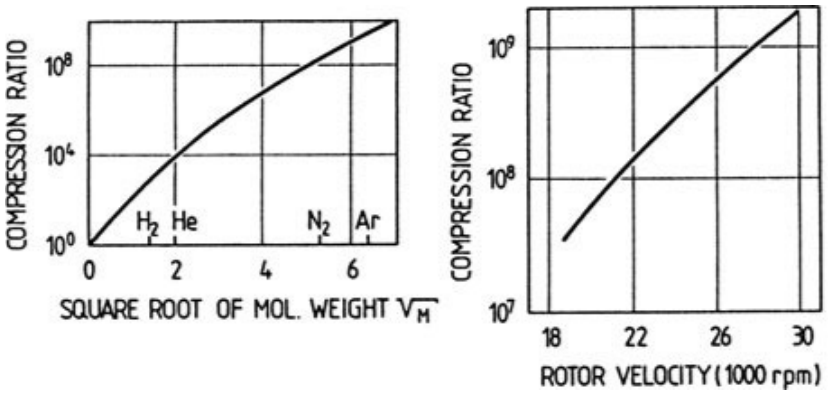

Figure A.3: Compression ratio of turbo molecular pump versus square root of molecular mass (left) and rotor velocity (right). Reprinted from [160].

A.1.3 Ion Pump

The ion pump is one of a family called capture pumps because it traps gases inside the UHV system. It usually operates at the pressure below 10^{-5} Torr and can maintain the pressure around 10^{-11} Torr. The basic components of ion pumps are short cylindrical anodes, which are made out of stainless steel, mounted in between two titanium cathodes. Anodes and cathodes are situated inside a strong magnetic field which is parallel to the cylindrical axes of the anodes. A high voltage around 7 kV is applied across the electrodes (anode and cathode) [92]. Fig.A.4 shows an illustration of ion pump.

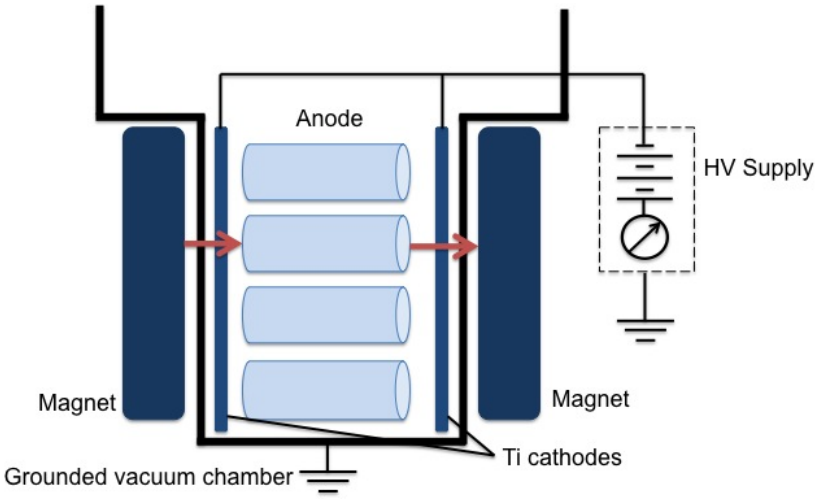

Figure A.4: Schematic illustration of ion pump

The magnetic field moves the emitted electrons from the cathodes in a helical tra-

jectory to the cylindrical anodes. The helical path increases the probability of collision between electrons and gas molecules. When electrons strike the gas molecules, they eject electrons from the gas molecule's valence shell and create a positive ion (ionised gas molecules). The applied electric field accelerates ionised gas molecules toward the cathode plates. Once the ionised gas molecules strike the cathode plates, they can diffuse through the cathode or react with the cathode. Titanium atoms will be ejected towards the anode tubes as a result of striking of ions with the cathode. The sputtered titanium will cover other parts of the pump and react with the residual gasses to increase the pumping effect [1]. The principle mechanism of its operation is shown in the Fig.A.5.

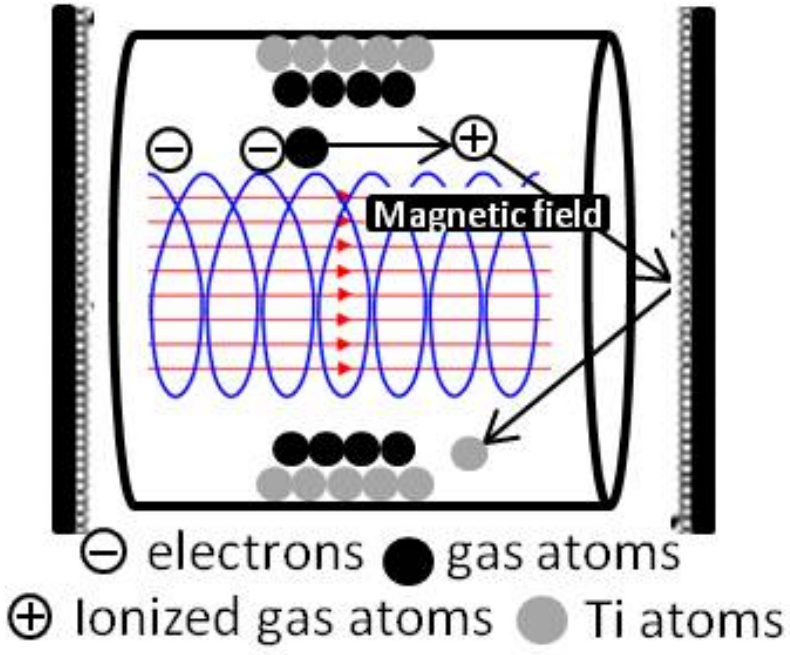

Figure A.5: Schematic illustration of ion pump operation.

The lifetime operation of ion pumps is inversely proportional to pressure. For example, the life time is only between 20 to 50 hours under continuous operation at 10^{-3} Torr while it lasts for about 6 years at 10^{-6} Torr. When operated under UHV the lifetime is almost infinite. Ion pumps are bakeable and vibration-free pumps and they can pump different gases and they do not require water cooling during operation [92, 93].

A.1.4 Titanium Sublimation Pump (TSP)

A TSP is usually used in addition to ion pumps. The operational mechanism of this pump is as follows. An electric current passes through a Ti-covered filament resulting in sublimation of the Ti. A non-volatile compound will be formed on the walls of

the chamber due to the reaction between the sublimated Ti and residual gases in the chamber such as oxygen or hydrogen; thus the gas pressure in the chamber will be reduced for a certain amount of time. Afterwards, the titanium filament can be heated again to regenerate the pumping capacity.

A.2 Gauges

Two main gauges are used in our UHV system which are Pirani and ion gauges;

A.2.1 Pirani Gauge

A Pirani gauge, which works in the pressure ranges between 10^{-3} and 10^{2} Torr (rough vacuum), uses thermal conductivity of gases to measure the pressure. It was invented in 1906 by Marcelo Pirani. It consists of a filament (usually platinum) inside a metal or glass tube connected to the vacuum chamber and the filament is connected with electric circuit (See Fig.A.6 for a schematic diagram). The pressure is measured due to variation of the filament resistance. A Wheatstone bridge is used to measure the resistance [92]. The constant current passes through the filament and the filament gets heated. The heat is transferred to the surrounding gas molecules by conduction. This causes a change in the temperature of the filament which changes the resistance of the filament. This change in resistance is a measure of the pressure and can be measured using the Wheatstone bridge.

A.2.2 Ion Gauge

An Ion gauge works in the molecular flow regime, at pressure ranges between 10^{-3} to 10^{-11} Torr. It works based on ionisation of gas molecules inside the chamber. Since the ion current and ionisation rate are directly proportional to the pressure, the pressure can be measured. It is composed of three electrodes: the filament, grid and collector as shown in the Fig.A.7. Electrons ejected from the filament are attracted towards a positive grid (+200 V) and some of them pass through the grid. These electrons collide with gas molecules to create positive ions. Then positive ions move toward the negative collector (-30 V). The ion current on the collector is directly proportional to the filament current (I_f) and pressure; therefore the pressure can be measured when the total ion current is measured on the collector. The gauge sensitivity is different for different gases [89, 92].

$$I_C = SPI_f \tag{A.1}$$

where: I_C is the collector ion current, S is the gauge sensitivity, P is the pressure and I_f is the filament current.

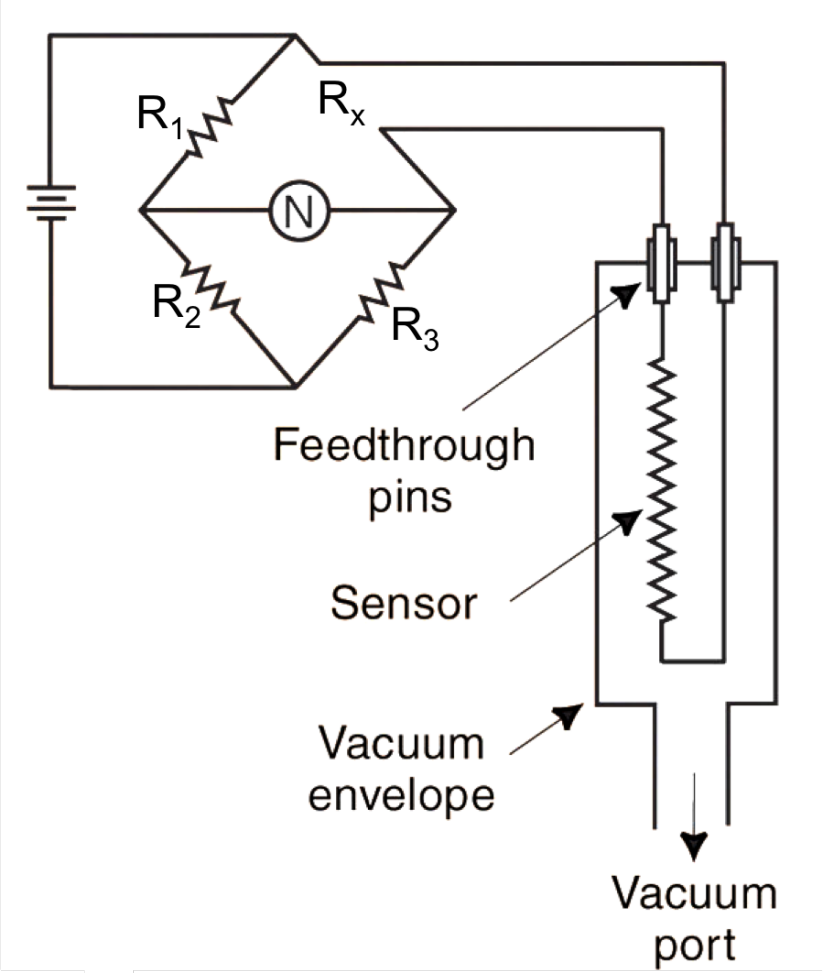

Figure A.6: Schematic illustration of pirani gauge

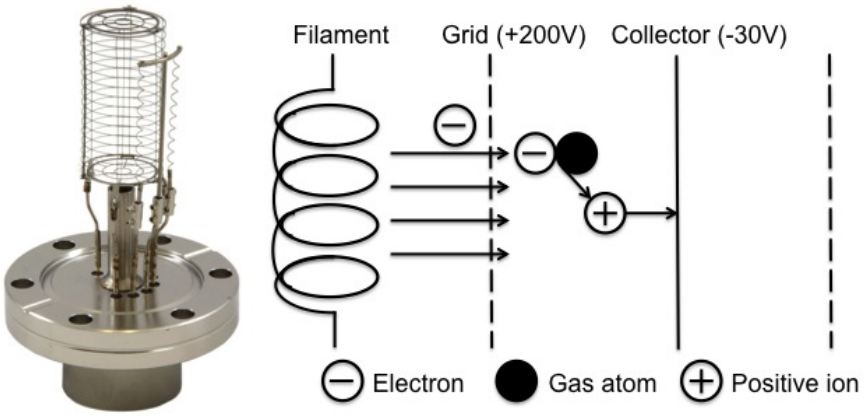

Figure A.7: Left photograph of ion gauge; right schematic diagram of its operation.

A.3 Mass Spectrometer

It is essential to have a mass spectrometer (Residual Gas Analyser (RGA)) attached to the UHV system as it can be used to monitor the partial pressure of the residual gasses

in the chamber as well as for leak detection. A mixture of CO, CO_2, H_2 and a small amount of H_2O are examples of typical residual gases in a properly baked UHV system [92]. A quadrupole mass spectrometer is used in the UHV chamber for the work of this thesis. The major components of the mass spectrometer are the ionisation source to produce ions, a mass analyser (four parallel cylindrical metal rods), the detector and data processing system to produce the mass spectrum [161]. Fig.A.8 displays a schematic illustration of a quadrupole mass spectrometer.

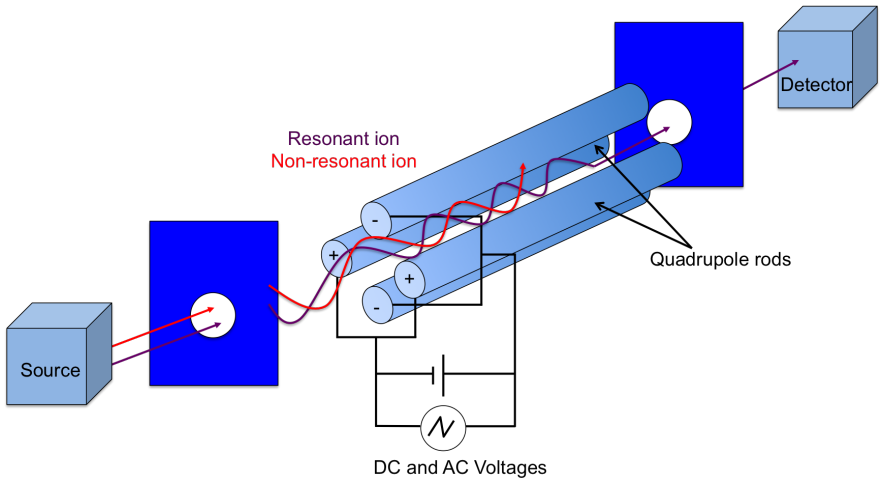

Figure A.8: Schematic illustration of a quadrupole mass spectrometer

A positive potential of (U + Vcos(wt)) is applied to two opposite rods and a negative potential of (- U - Vcos(wt)) is applied to the other two. U, Vcos(wt) represent the DC and AC voltage respectively, where w and t are frequency and time. The trajectory of ions traveling through the rods are influenced by the applied voltage. The ions are filtered based on their mass - to - charge ratio (m/z) during passing through quadrupole rods. Therefore, for a given DC and AC voltage ions of certain (m/z) can reach the detector (purple ions in Fig.A.8) others collide with rods and deflects from their original path (red ions in Fig.A.8). Thus a mass spectrum is produced and detected by the detector.

Appendix B

List of Publications

- **S. S. Hars**, H. R. Sharma, J. A. Smerdon, T. P. Yadav, R. Tamura, M. Shimoda and R. McGrath, **The Structure of the (100) Surface of Ag-In-Gd 1/1 Approximant**, Acta Physica Polonica A, 126, 479, (2014).
- J. A. Smerdon, K. M. Young, M. Lowe, **S. S. Hars**, T. P. Yadav, D. Hesp, V. R. Dhanak, A. P. Tsai, H. R. Sharma, and R. McGrath, **Templated Quasicrystalline Molecular Ordering**, Nano Letters, 14, 1184, (2014).
- **S. S. Hars**, H. R. Sharma, J. A. Smerdon, T. P. Yadav, A. Al-Mahboob, J. Ledieu. V. Fournée, R. Tamura and R. McGrath, **Surface Structure of the Ag-In-RE Complex Intermetallics (RE = Tb and Gd)**, in preparation.
- **S. S. Hars**, J. A. Smerdon, H. R. Sharma, A. P. Tsai and R. McGrath, **The Growth of Bi on the five-fold Surface of *i*-Ag-In-Yb quasicrystal**, in preparation.
- V. Fournée, **S. S. Hars**, H. R. Sharma, J. Ledieu, A. P. Tsai and R. McGrath, **The Growth of In on the five-fold Surface of *i*-Ag-In-Yb quasicrystal**, in preparation.

Appendix C

Presentations

1. Poster Presentations

   - *Surface Structure of Ag-In-RE (Gd, Tb and Yb) 1/1 Approximants*, 29^{th} European Conference on Surface Science (ECOSS-29), 3 -7 September 2012, Edinburgh, Scotland, UK.
   - *Surface study of Ag-In-RE (Gd, Tb and Yb) 1/1 Crystalline Approximants*, C - MAC Days 2012, 10 - 13 December 2012, Kraków, Poland.
   - *Metallic Films on the Five-Fold Surface of i-Ag-In-Yb Quasicrystal*, Interdisciplinary Surface Science Conference (ISSC -19), 25 - 28 March 2013, Nottingham, UK.
   - *Growth of Metallic Films on of i-Ag-In-Yb Quasicrystal and Related Approximants*, C-MAC EuroSchool 2014, 16 - 20 June, 2014, Liverpool, UK.
   - *Surface Structure of Ag-In-RE Approximants and Quasicrystalline Metallic Films on the Surface of i-Ag-In-Yb Quasicrystal*, C - MAC Days 2014, 8 - 11 December 2014, Zagreb, Croatia.

2. Oral Presentations

   - *Ag-In-Based Quasicrystals and Approximants as a Template to Grow Metallic Thin Films*, 12^{th} International Conference on Quasicrystals (ICQ- 12), 1 -6 September 2013, Kraków, Poland.

List of Figures

List of Tables

Bibliography

[1] P. Hofmann, *Surface Physics* (Philip Hofmann, Kindle Edition, 2013).

[2] G. Attard and C. Barnes, *Surfaces*, *59* (Oxford Science Publications, Oxford, 1998).

[3] D. Shechtman, I. Blech, D. Gratias, and J. W. Cahn, Phys. Rev. Lett. **53**, 1951 (1984).

[4] The Noble Prize in Chemistry 2011.

[5] P. A. Thiel, Prog. Surf. Sci. **75**, 69 (2004).

[6] P. A. Thiel, Ann. Rev. Phys. Chem. **59**, 129 (2008).

[7] P. A. Thiel and B. Unal, in *Encyclopedia of Surface and Colloid Science*, 2nd ed., edited by P. Somasundaran (Taylor & Francis, Boca Raton, Florida, 2010), Vol. 2, pp. 1 – 10.

[8] D. V. Louzguine-Luzgin and A. Inoue, Annu. Rev. Mater. Res. **38**, 403 (2008).

[9] H. R. Sharma, M. Shimoda, and A. P. Tsai, Adv. Phys. **56**, 403 (2007).

[10] R. McGrath, J. A. Smerdon, H. R. Sharma, W. Theis, and J. Ledieu, J. Phys.: Condens. Matter **22**, 084022 (2010).

[11] M. Krajčí, J. Hafner, J. Ledieu, V. Fournée, and R. McGrath, Phys. Rev. B **82**, 085417 (2010).

[12] J. Ledieu, M. Krajčí, J. Hafner, L. Leung, L. Wearing, R. McGrath, T. Lograsso, D. Wu, and V. Fournée, Phys. Rev. B **79**, 165430 (2009).

[13] A. P. Tsai, J. Q. Guo, E. Abe, H. Takakura, and T. J. Sato, Nature **408**, 537 (2000).

[14] J. Q. Guo, E. Abe, and A. P. Tsai, Phys. Rev. B **62**, 14605 (2000).

[15] H. Takakura, C. Gómez, A. Yamamoto, M. De Boissieu, and A. Tsai, Nat. Mat. **6**, 58 (2007).

[16] H. R. Sharma, M. Shimoda, K. Sagisaka, H. Takakura, J. A. Smerdon, P. J. Nugent, R. McGrath, D. Fujita, S. Ohhashi, and A. P. Tsai, Phys. Rev. B **80**, 121401 (2009).

[17] D. Gratias, F. Puyraimond, M. Quiquandon, and A. Katz, Phys. Rev. B **63**, 024202 (2000).

[18] R. Tamura, Y. Murao, S. Takeuchi, K. Tokiwa, T. Watanabe, T. J. Sato, and A. P. Tsai, Jpn. J. Appl. Phys. **40**, L912 (2001).

[19] Y. Muro, T. Sasakawa, T. Suemitsu, T. Takabatake, R. Tamura, and S. Takeuchi, Jpn. J. Appl. Phys. **41**, 3787 (2002).

[20] S. Ohhashi, J. Hasegawa, S. Takeuchi, and A. Tsai, Phil. Mag. **87**, 3089 (2007).

[21] J. Q. Guo and A. P. Tsai, Phil. Mag. Lett. **82**, 349 (2002).

[22] R. Tamura, to be published (2015).

[23] C. Cui and A. P. Tsai, Phil. Mag. **91**, 2443 (2011).

[24] A. I. Goldman and R. F. Kelton, Rev. Mod. Phys. **65**, 213 (1993).

[25] A. P. Tsai and C. P. Gomez, *Handbook of Metal Physics* (Elsevier, Amesterdam, 2008), Vol. 3, pp. 75–106.

[26] C. Cui and A. P. Tsai, J. Alloy. Comp. **536**, 91 (2012).

[27] S. S. Hars and et al., In preparation. (2015).

[28] S. S. Hars, H. R. Sharma, J. A. Smerdon, T. P. Yadav, R. Tamura, M. Shimoda, and R. McGrath, Act. Phys. Polon. A **126**, 479 (2014).

[29] C. Cui, H. R. Sharma, P. J. Nugent, M. Shimoda, and A. P. Tsai, Act. Phys. Polon. A **126**, 577 (2014).

[30] L. A. Bendersky and R. J. Schaefer, Physica A: Statistical Mechanics and its Applications **140**, 298 (1986).

[31] A. Kumar, *Introduction to Solid State Physics* (PHI Learning Private Limited, New Delhi, 2010).

[32] D. Levine and P. J. Steinhardt, Phys. Rev. Lett. **53**, 2477 (1984).

[33] R. McGrath, J. Ledieu, E. J. Cox, and R. D. Diehl, J. Phys.: Condensed Matter **14**, R119 (2002).

[34] S. O. Pillai, *Solid State Physics*, 6 ed. (New Age Science, Tunbridge Wells-United Kingdom, 2009).

[35] A. P. Tsai, Acc. Chem. Res. **36**, 31 (2003).

[36] L. Pauling, Nature **317**, 512 (1985).

[37] R. McGrath, U. Grimm, and R. D. Diehl, Physics World 23 (2005).

[38] T. Ishimasa, H.-U. Nissen, and Y. Fukano, Phys. Rev. Lett. **55**, 511 (1985).

[39] N. Wang, H. Chen, and K. H. Kuo, Phys. Rev. Lett. **59**, 1010 (1987).

[40] L. Bendersky, Phys. Rev. Lett. **55**, 1461 (1985).

[41] 1992 International Union of Crystallography Acta Crystallographica A **48**, 922. .

[42] B. Dubost, J. M. Lang, M. Tanaka, P. Sainfort, and M. Audier, Nature **324**, 48 (1986).

[43] A. P. Tsai, A. Inoue, and T. Masumoto, J. Mater. Sci. Lett. **6**, 1403 (1987).

[44] A. P. Tsai, A. Inoue, and T. Masumoto, Jpn. J. Appl. Phys. **26**, L1505 (1987).

[45] X. Zeng, G. Ungar, Y. Liu, V. Percec, A. E. Dulcey, and J. K. Hobbs, Nature **428**, 157 (2004).

[46] A. Takano, W. Kawashima, A. Noro, Y. Isono, N. Tanaka, T. Dotera, and Y. Matsushita, J. Polym. Sci. Polym. Phys. **43**, 2427 (2005).

[47] K. Hayashida, T. Dotera, A. Takano, and Y. Matsushita, Phys. Rev. Lett. **98**, 195502 (2007).

[48] S. Förster, K. Meinel, R. Hammer, M. Trautmann, and W. Widdra, Nature **502**, 215 (2013).

[49] J. Mikhael, J. Roth, L. Helden, and C. Bechinger, Nature **454**, 501 (2008).

[50] S. Fischer, A. Exner, K. Zielske, J. Perlich, S. Deloudi, W. Steurer, P. Lindner, and S. Förster, Proceedings of the National Academy of Sciences **108**, 1810 (2011).

[51] L. Bindi, P. J. J. Steinhardt, N. Yao, and P. J. Lu, Science **324**, 1306 (2009).

[52] L. Bindi, P. J. Steinhardt, N. Yao, and P. J. Lu, American Mineralogist **96**, 928 (2011).

[53] P. J. Steinhardt and L. Bindi, Phil. Mag. **91**, 2421 (2011).

[54] L. Bindi, J. M. Eiler, Y. Guan, L. S. Hollister, G. MacPherson, P. J. Steinhardt, and N. Yao, Proceedings of the National Academy of Sciences **109**, 1396 (2012).

[55] C. Janot, *Quasicrystals*, 2nd ed. (Springer, Grenbole-France, 1994).

[56] B. Grünbaum and G. C. Shephard, *Tilings and patterns* (W. H. Freeman Co Ltd, New York, 1987).

[57] R. Penrose, Bull. Inst. Math. Appl. **10**, 266 (1974).

[58] H. R. Sharma, Ph.D. thesis, Freie Universität, Berlin, 2002.

[59] A. Yamamoto and K. N. Ishihara, Acta Crystallogr. A **44**, 707 (1988).

[60] J. A. Smerdon, Ph.D. thesis, The University of Liverpool, 2008.

[61] V. Fournée and P. A. Thiel, J. Phys. Appl. Phys. **38**, R83 (2005).

[62] M. Duneau and A. Katz, Phys. Rev. Lett. **54**, 2688 (1985).

[63] A. Katz and M. Duneau, J. Physique **47**, 181 (1986).

[64] K. M. Young, Ph.D. thesis, The University of Liverpool, 2012.

[65] P. J. Lu and P. J. Steinhardt, Science. **315**, 1106 (2007).

[66] J. Bohannon, Science **315**, 1066 (2007).

[67] I. Hargittai, *Fivefold symmetry* (World Scientific, Singapore, 1992).

[68] P. A. Thiel, A. I. Goldman, and C. J. Jenks, in *Physical properties of quasicrystals*, edited by Z. M. Stadnik (Springer, Berlin, 1999), Vol. 126.

[69] H. S. Jeevan and S. Ranganathan, J. Non-Crys. Sol. **334**, 184 (2004).

[70] D. A. Shulyatev, Cryst. Rep. **52**, 938 (2007).

[71] T. Ishimasa, Handbook of Metal Physics **3**, 49 (2008).

[72] A. P. Tsai, Sci. Technol. Adv. Mater **9**, 013008 (2008).

[73] M. de Boissieu, H. Takakura, C. P. Gòmez, A. Yamamoto, and A. P. Tsai, Phil. Mag. **87**, 2613 (2007).

[74] W. Hume-Rothery, J. Inst. Met. **35**, 295 (1926).

[75] A. Tsai, J. Non-Crys. Sol. **334**, 317 (2004).

[76] J. Q. Guo, E. Abe, and A. P. Tsai, Phil. Mag. Lett. **82**, 27 (2002).

[77] P. J. Nugent, Ph.D. thesis, The University of Liverpool, 2011.

[78] A. Yamamoto, H. Takakura, and A. P. Tsai, Phys. Rev. B **68**, 094201 (2003).

[79] R. Tamura, Isr. J. Chem. **51**, 1263 (2011).

[80] V. Elser, Phys. Rev. B **32**, 4892 (1985).

[81] C. Cui and A. P. Tsai, J. Cryst. Growth. **312**, 131 (2009).

[82] C. P. Gómez and S. Lidin, Phys. Rev. B **68**, 024203 (2003).

[83] C. P. Gómez and S. Lidin, Angew. Chem. Int. Edn. **40**, 4037 (2001).

[84] C. P. Gómez, *Order and disorder in the RE-Cd and related systems* (Institutionen för fysikalisk, oorganisk och strukturkemi., Stockholms, Sweeden, 2003).

[85] *Surface Analysis-The Principal Techniques*, edited by J. C. Vickerman (John Wiley & Sons, Chichester, West Sussex, England, 1997).

[86] J. F. O'Hanlon, *A User's Guide to Vacuum Technology*, 3rd ed. (John Wiley & Sons, Hoboken, New Jersey, 2003).

[87] W. Umrath, *Fundamentals of Vacuum Technology* (Oerlikon Leybold Vacuum, Cologne, 1998).

[88] C. Harding and C. McKee, in *Physical Chemistry, S342 Block 6*, edited by I. Nuttall and D. Sharp (The Dorset Press, Dorchester, 1996).

[89] Y. W. Chung, *Practical Guide to Surface Science and Spectroscopy* (Academic Press, San Diego, California, 2001).

[90] J. A. Venables, *Introduction to Surface and Thin Film Processes* (Cambridge University Press, Cambridge, 2003).

[91] A. Chamber, R. K. Fitch, and B. S. Halliday, *Basic Vacuum Technology*, 2nd ed. (IOP Publishing, London, 1998).

[92] K. Oura, V. G. Lifshits, A. A. Saranin, A. V. Zotov, and M. Katayama, *Surface Science An Introduction* (Springer-Verlag, Berlin Heidelberg, 2003).

[93] J. H. Moore, C. C. Davis, M. A. Coplan, and S. C. Greer, *Building Scientific Apparatus* (Cambridge University Press, Cambridge, 2009).

[94] M. Prutton, *Introduction to Surface Physics* (Oxford Science Publications, Oxford, 2002).

[95] D. P. Woodruff and T. A. Delchar, *Modern Techniques of Surface Science*, 2nd ed. (Cambridge University Press, Cambridge, 1999).

[96] H. R. Sharma, M. Shimoda, S. Ohhashi, and A. P. Tsai, Phil. Mag. **87**, 2989 (2007).

[97] K. Seshan, *Handbook of Thin-Film Deposition Processes and Techniques*, 2nd ed. (Noyes Publications/William Andrew Publishing, Norwich, New York, 2002).

[98] C. Kittel, *Introduction to Solid State Physics*, eighth ed. (John Wiley & Sons, Inc, New York, 2005).

[99] R. Tilley, *Crystals and Crystal Structure* (John Wiley & Sons, Ltd, Chichester, West Sussex, England, 2006).

[100] P. M. Chaikin and T. C. Lubensky, *Principles of Condensed Matter Physics* (Cambridge University Press, Cambridge, 1995).

[101] J. J. Quinn and K. S. Yi, *Solid State Physics* (Springer-Verlag, Berlin Heidelberg, 2009).

[102] J. P. Srivastava, *Elements of Solid State Physics*, 2nd ed. (PHI Learning Private Limited, New Delhi, 2009).

[103] C. Davisson and L. H. Germer, Phys. Rev. **30**, 705 (1927).

[104] *Scanning Tunneling Microscopy*, edited by J. A. Stroscio and W. J. Kaiser (Academic Press, INC., San Diego, California, 1993), Vol. 27.

[105] H.-J. Güntherodt and R. Wiesendanger, in *Scanning Tunneling Microscopy I*, 2nd ed., edited by R. Gomer (Springer-Verlag, Berlin Heidelberg, 1994).

[106] C. J. Chen, *Introduction to Scanning Tunneling Microscopy* (Oxford University Press, 200 Madison Avenue, New York, 1993).

[107] C. Bai, *Scanning Tunneling Microscopy and It's Applications*, 2nd ed. (Shangahai Scientific & Technical Publishers and Springer-Verlag, Berlin Heidelberg, 1992).

[108] R. Wiesendanger, *Scanning Probe Microscopy and Spectroscopy* (Cambridge University Press, Cambridge, 1994).

[109] G. H. Haertling, J. Am. Ceram. Soc. **82**, 797 (1999).

[110] L. B. Kong, T. Li, H. H. Hng, F. Boey, T. Zhang, and S. Li, *Waste Energy Harvesting* (Springer-Verlag, Berlin Heidelberg, 2014).

[111] A. I. Oliva, A. Romero, J. L. Peña, E. Anguiano, and M. Aguilar, Revi. Sci. Instrum. **67**, 1917 (1996).

[112] T. Hagedorn, M. El Ouali, W. Paul, D. Oliver, Y. Miyahara, and P. Grütter, Revi. Sci. Instrum. **82**, 113903 (2011).

[113] I. Ekvall, E. Wahlström, D. Claesson, H. Olin, and E. Olsson, Measurement Science and Technology **10**, 11 (1999).

[114] A. H. Sorensen, U. Hvid, M. W. Mortensen, and K. A. Morch, Revi. Sci. Instrum. **70**, 3059 (1999).

[115] J. P. Ibe, P. P. Bey Jr, S. L. Brandow, R. A. Brizzolara, N. A. Burnham, D. P. DiLella, K. P. Lee, C. R. K. Marrian, and R. J. Colton, J. Vac. Sci. Technol. A **8**, 3570 (1990).

[116] J. Méndez, M. Luna, and A. M. Baro, Surf. Sci. **266**, 294 (1992).

[117] E. Bauer, Z. Kristallogr. **110**, 395 (1958).

[118] M. Ohring, *Materials Science of Thin Films* (Academic press, San Diego, California, 2001).

[119] C. Cui, P. J. Nugent, M. Shimoda, J. Ledieu, V. Fournée, A. P. Tsai, R. McGrath, and H. R. Sharma, J. Phys.: Condensed Matter **24**, 445011 (2012).

[120] C. Cui, P. J. Nugent, M. Shimoda, J. Ledieu, V. Fournée, A. P. Tsai, R. McGrath, and H. R. Sharma, J. of Phys.: Condensed Matter **26**, 015001 (2014).

[121] C. Cui, M. Shimoda, and A. P. Tsai, RSC Adv. **4**, 46907 (2014).

[122] Y. Ishii and T. Fujiwara, Phys. Rev. Lett. **87**, 206408 (2001).

[123] I. Horcas, R. Fernández, J. M. Gomez-Rodriguez, J. Colchero, J. Gómez-Herrero, and A. M. Baro, Rev. Sci. Instrum. **78**, 013705 (2007).

[124] K. Momma and F. Izumi, J. Appl. Crystallogr. **44**, 1272 (2011).

[125] R. Tamura, Private Discussion .

[126] K. Nozawa and Y. Ishii, in *J. Phys.: Conf. Ser.* (IOP Publishing, London, 2010), No. 1, p. 012030.

[127] H. R. Sharma, J. A. Smerdon, K. M. Young, and R. McGrath, J. of Phys.: Condensed Matter **24**, 354012 (2012).

[128] J. A. Smerdon, H. R. Sharma, J. Ledieu, and R. McGrath, J. of Phys.: Cond. Matter **20**, 314005 (2008).

[129] J. Ledieu, J. T. Hoeft, D. E. Reid, J. A. Smerdon, R. D. Diehl, T. A. Lograsso, A. R. Ross, and R. McGrath, Phys. Rev. Lett. **92**, 135507 (2004).

[130] L. Wearing, Ph.D. thesis, The University of Liverpool, 2008.

[131] J. Ledieu, J. T. Hoeft, D. E. Reid, J. A. Smerdon, R. D. Diehl, N. Ferralis, T. A. Lograsso, A. R. Ross, and R. McGrath, Phys. Rev. B **72**, 035420 (2005).

[132] K. J. Franke, H. R. Sharma, W. Theis, P. Gille, P. Ebert, and K. H. Rieder, Phys. Rev. Lett. **89**, 156104 (2002).

[133] M. Krajčí and J. Hafner, Phys. Rev. B **71**, 184207 (2005).

[134] J. A. Smerdon, J. Ledieu, R. McGrath, T. C. Q. Noakes, P. Bailey, M. Draxler, C. F. McConville, T. A. Lograsso, and A. R. Ross, Phys. Rev. B **74**, 035429 (2006).

[135] J. A. Smerdon, J. Ledieu, J. T. Hoeft, D. E. Reid, L. H. Wearing, R. D. Diehl, T. A. Lograsso, A. R. Ross, and R. McGrath, Phil. Mag. **86**, 841 (2006).

[136] J. Ledieu, P. Unsworth, T. A. Lograsso, A. R. Ross, and R. McGrath, Physical Review B **73**, 012204 (2006).

[137] H. R. Sharma, M. Shimoda, J. A. Barrow, A. R. Ross, T. A. Lograsso, and A. P. Tsai, Mat. Res. Soc. Symp. Proc. **805**, LL7.10 (2004).

[138] H. R. Sharma, M. Shimoda, A. R. Ross, T. A. Lograsso, and A. P. Tsai, Phys. Rev. B **72**, 045428 (2005).

[139] H. R. Sharma, M. Shimoda, A. R. Ross, T. A. Lograsso, and A. P. Tsai, Phil. Mag. **86**, 807 (2006).

[140] T. Cai, J. Ledieu, R. McGrath, V. Fournée, T. Lograsso, A. Ross, and P. Thiel, Surf. Sci. **526**, 115 (2003).

[141] L. Leung, J. Ledieu, P. Unsworth, T. A. Lograsso, A. R. Ross, and R. McGrath, Surf. Sci. **600**, 4752 (2006).

[142] M. Shimoda, J. Q. Guo, T. J. Sato, and A. P. Tsai, J. Non-Cryst. Solids **334**, 505 (2004).

[143] P. Hofmann, Prog. Surf. Sci. **81**, 191 (2006).

[144] J. A. Smerdon, N. Cross, V. R. Dhanak, H. R. Sharma, K. M. Young, T. A. Lograsso, A. R. Ross, and R. McGrath, J. of Phys.: Condensed Matter **22**, 345002 (2010).

[145] V. Fournée, H. R. Sharma, M. Shimoda, A. P. Tsai, B. Unal, A. R. Ross, T. A. Lograsso, and P. A. Thiel, Phys. Rev. Lett. **95**, 155504 (2005).

[146] J. A. Smerdon, J. K. Parle, L. H. Wearing, T. Lograsso, A. R. Ross, and R. McGrath, Phys. Rev. B **78**, 075407 (2008).

[147] H. R. Sharma, K. Nozawa, J. A. Smerdon, P. J. Nugent, I. McLeod, V. R. Dhanak, M. Shimoda, Y. Ishii, A. P. Tsai, and R. McGrath, Nat. Comm. **4**, (2013).

[148] P. J. Nugent and et al., In preparation. (2015).

[149] J. A. Smerdon, K. M. Young, M. Lowe, S. S. Hars, T. P. Yadav, D. Hesp, V. R. Dhanak, A. P. Tsai, H. R. Sharma, and R. McGrath, Nano Lett. **14**, 1184 (2014).

[150] H. Takakura, C. P. Gómez, A. Yamamoto, M. de Boissieu, and A. P. Tsai, Nat. Mat. **6**, 58 (2007).

[151] H. R. Sharma, J. Ledieu, V. Fournée, and P. Gille, Phil. Mag. **91**, 2870 (2011).

[152] H. R. Sharma, J. A. Smerdon, P. J. Nugent, A. Ribeiro, I. McLeod, V. R. Dhanak, M. Shimoda, A. P. Tsai, and R. McGrath, J. Chem. Phys. **140**, 174710 (2014).

[153] K. Nozawa, In preparation .

[154] H. Okamoto, J. Phas. Equil. **20**, 453 (1999).

[155] M. Shimoda, Prog. Surf. Sci. **75**, 87 (2004).

[156] M. Shimoda, J. Q. Guo, T. J. Sato, and A. P. Tsai, Surf. Sci. **482**, 784 (2001).

[157] M. Shimoda, T. J. Sato, A. P. Tsai, and J. Q. Guo, Phys. Rev. B **62**, 11288 (2000).

[158] H. R. Sharma, V. Fournée, M. Shimoda, A. R. Ross, T. A. Lograsso, P. Gille, and A. P. Tsai, Phy. Rev. B **78**, 155416 (2008).

[159] F. Sommer, B. Predel, G. Borzone, N. Parodi, and R. Ferro, Intermetallics **3**, 15 (1995).

[160] H. Lüth, *Solid Surfaces, Interfaces and Thin Films*, fifth ed. (Springer-Verlag, Berlin Heidelberg, 2010).

[161] E. d. Hoffmann and V. Stroobant, *Mass spectrometry: principles and applications*, 3rd ed. (John Wiley & Sons, Ltd, Chichester, West Sussex, England, 2007).